博士論文

Bouncing behavior of a water droplet on a super-hydrophobic surface near freezing temperatures

(氷点付近における超撥水面上の水滴の動的挙動に関する研究)

王 恒

Contents

Acknowledgements

First of all, I would like to take this opportunity to thank my Ph.D. supervisor Professor Hirofumi Daiguji for his support and guidance during the past three years. Thanks for providing me with the opportunity to study and pursue the Ph.D. degree in our lab. I also want to thank Lecturer Wei-Lun Hsu because he gives me many helpful suggestions on doing good research.

Besides, I also want to thank the rest of my thesis committee: Professor Shigeo Maruyama, Professor Junichiro Shiomi, Professor Jean-Jacques Delaunay, and Professor Takaaki Inada for their valuable questions and inspiring advices on my research. During the past 3 years in Daiguji & Hsu lab, I have received a lot of help and fruitful discussions from my lab-mates including Dr. Jubair A. Shamim, Ms. Qian Wu, Ms. Lili Yu, Mr. Soumyadeep Paul, Mr. Shubo Fei, Mr. Zhixuan Wang, and Ms. Zixuan Qin. I also want to thank Ms. Shoko Shidara for the help about administration.

Finally, I would like to thank my parents. They support me and love me without any conditions. It is my honor and pleasure to be your son and to grow up in such a great family. Ph.D. is a tough journey and COVID 19 makes it more challenging. But I believe that we human beings will defeat the virus and the world will return to normal in the very near future. The world will be filled with peace and love!

Abstract

In recent years, super-hydrophobic surfaces (SHSs) fabricated through mimicking surface structures of plants and animals in nature have fascinated a lot of interests among researchers and engineers. Due to low surface energy of SHSs, they have demonstrated outstanding potentials to mitigate ice accumulation and exceptional capabilities to repel water droplets for anti-icing applications. However, the underlying physics dominating the rebounding behavior of an impact water droplet on an SHS near the freezing temperatures is still poorly understood. Hence, to understand the ice-phobic nature of SHS, this research focuses on conducting experiments to explore the bouncing mechanism of a water droplet on a cold SHS. The SHS is controlled under the condition of large temperature difference between the SHS and the impinging water droplet. The influence of surface temperature of SHS, initial temperature of a water droplet, which is the same as the ambient temperature, and droplet size on the bouncing behaviors is investigated.

The SHS utilized in this study is fabricated by spray-coating of a suspension of acetylene black and trimethylsiloxysilicate on a copper substrate. To evaluate the dynamics of water droplet during impact, the contact time and rebounding height are measured and employed as performance parameters. The ice-phobic nature of SHS is evaluated for a wide range of SHS temperature maintained around the freezing point of water (283 K–248 K). In addition, the effects of increasing the droplet temperature (278 K–293 K) and droplet size (2.07 mm–2.99 mm) on the droplet rebounding behavior are also analyzed.

Experimental results show that when the droplet initial temperature is at 278 K, the contact time increases, and the rebounding height decreases or even to zero (adhesion to SHS) as the surface temperature of SHS is reduced from 283 K to 248 K. Besides, as the initial temperature of the droplet is increased from 278 K to 293 K, the impinging droplet presents the tendency to adhere to cold SHS. With an increase in droplet size from 2.07 mm to 2.99 mm, these trends become more prominent.

The experimental results are elucidated by the fact that when an impinging water droplet of relatively higher temperature comes into contact with an SHS maintained at

much lower temperature, the rapid evaporation from the droplet could take place during the droplet impact process. As a result, the space between the droplet and micro/nano surface textures of SHS might become supersaturated. At low temperature of SHS, the empty space inside the hierarchical micro/nano surface textures of SHS could be instantly filled with water owing to the local condensation of evaporated water vapor.

Consequently, as the condensed water accumulates inside micro/nano textures of SHS water bridges linking the droplet and SHS could occur, the wetting transition from the Cassie-Baxter state to the Wenzel state takes place, and the super-hydrophobicity of the surface could no longer be preserved. The formed water bridges also yield the increase of droplet-SHS adhesion. Due to the increment in adhesion between the impinging droplet and water bridges within micro/nano surface cavities, a larger amount of kinetic energy was spent during the droplet rebound. Therefore, for the impinging droplet, a noticeable decrease in the residual energy occurs, resulting in an extended contact time and a reduction in rebounding height.

At a lower SHS temperature or a higher water droplet temperature, an increment of the rate of water condensation on SHS could happen. In addition, with an increase in droplet size there is an extended droplet-SHS contact time as well as an increase of the amount of condensed water. Under different experimental conditions, the amount of condensed water is evaluated via liquid-vapor phase transport model and a detailed energy analysis is elucidated during droplet rebounding process, which verify the proposed mechanism.

In addition, this study investigates the wetting transition of a sessile water droplet on a cold SHS from the Cassie-Baxter state to Wenzel state induced by the condensation of evaporated water vapor inside SHS hierarchical micro/nano textures. The receding contact angle of a sessile water droplet with the initial temperature of 278 K on an SHS with different temperatures (283 K–258 K) is measured and selected as the performance parameter. Compared with SHS at 283 K and 278 K, there is a significant decrease in receding contact angle when SHS temperature is reduced to 268 K, which could be caused by the existence of condensed water inside SHS micro/nano structures. When SHS is changed from 268 K to 258 K, the receding contact angle demonstrates a weak

dependency on surface temperature owing to the sufficient time for vapor condensation to completely fill SHS micro/nano structures with condensed water.

To further interpret the dynamics of an impinging droplet on SHS near freezing temperatures, computational fluid dynamics (CFD) simulations through the volume of fluid (VOF) method are applied. A body force based on the continuum surface force model is adopted in the momentum equation to account for the effect of surface tension. The wetting transition observed in experiments is added as a boundary condition via the wall adhesion model and quasi-dynamic contact angle model. The numerical modeling is validated through comparing the side-view profiles of impact droplet, time-course contact length, contact time, and rebounding height between experiments and simulations. Viscous loss calculated via simulation is compared with energy loss analysis carried out in experiments to validate the energy analysis model. A detailed viscous loss analysis is executed during the droplet spreading, recoiling, and rebounding processes on an SHS to interpret the droplet impacting dynamics in consideration of velocity distribution within droplet and surface energy variation.

To analyze the dominant factor determining the rebounding or sticking physics of an impact water droplet on SHS near freezing temperatures, parametric study is carried out in consideration of surface characteristics (i.e., droplet-surface adhesion in terms of contact angle) and water droplet properties (i.e., viscosity and surface tension coefficient). As the droplet-surface adhesion increases (i.e., receding contact angle decreases), the droplet recoiling decelerates, and the rebounding height becomes lower or even 0. When the droplet-surface adhesion increases, there is a reduction in the surface tension force near the surface, particularly in vertical direction. Besides, non-wetting condition is considered to evaluate the maximum energy loss due to viscosity for an impact water droplet. When the initial potential energy is insufficient for the summation of maximum energy loss due to viscosity and maximum energy loss due to adhesion, the droplet forfeits rebounding capability on SHS. Within capillary-inertial regime, contact time shows an irrelevant relationship with water viscosity. But with the increase of water viscosity, the impact droplet bounces to a lower height because of the increment of viscous loss. As the increase of surface tension coefficient, there is a decrease in contact time because the capillarity is equilibrated with the inertia. Meanwhile, there is an

increase in rebounding height owing to reduction in in viscous loss as the larger surface tension restricts droplet spread on surface. The parametric study demonstrates that under the experimental conditions of this work, the dominant mechanism affecting the impact behaviors of a water droplet on an SHS near freezing temperatures is the wetting transition induced by the water condensation inside SHS micro/nano textures.

In summary, the experimental findings indicate that the wetting transition caused by the accumulation of condensed water within micro/nano textures of an SHS near freezing temperatures may significantly alter the droplet rebounding behaviors. The numerical simulations reproduce droplet impacting performance observed from experiments, demonstrate the significance of wetting transition, and validate the energy loss analysis during droplet impact process. For fully droplet rebounding, it is necessary for the impact water droplet to process sufficiently high kinetic energy for energy loss due to adhesion and viscosity. Besides, the surface force near the SHS needs to be large enough to drag the droplet away from the SHS.

When considered in anti-icing applications, SHSs are expected to repel impinging water droplets under various conditions. The present research explores the significance of condensed water from the impact water droplet within micro/nano surface textures to the rebounding capability of droplet on an SHS near freezing temperatures. The substantial understanding of this droplet rebound mechanism will provide valuable insights on the rational design of SHSs for anti-icing or de-icing purposes.

List of Figures

List of Tables

Nomenclature

Roman symbols

A	area [m^2]
A_c	contact area [m^2]
C_p	specific heat [kJ kg^{-1} K^{-1}]
$C_{p\mathrm{a}}$	air specific heat [kJ kg^{-1} K^{-1}]
$C_{p\mathrm{w}}$	water specific heat [kJ kg^{-1} K^{-1}]
D	droplet diameter [m]
$\mathcal{D}$	diffusion coefficient [m^2 s^{-1}]
d_max	maximum droplet-SHS contact length [m]
dr/dt	condensation growth rate [m s^{-1}]
E_0	total energy of impinging droplet [J]
E_a	energy loss due to adhesion [J]
$E_{\mathrm{a-max}}$	maximum energy loss due to adhesion [J]
E_loss	total energy loss [J]
E_p	potential energy [J]
E_{p0}	initial potential energy [J]
E_pr	residual potential energy [J]
E_r	total energy of rebounding droplet [J]
E_μ	energy loss due to viscosity [J]
$E_{\mu-\mathrm{max}}$	maximum energy loss due to viscosity [J]
$E_{\mu-\Delta\mathrm{t}}$	viscous loss in every millisecond [J]
F_drag	drag force [N]
$\boldsymbol{F_\gamma}$	volumetric surface force [N m^{-3}]
$\boldsymbol{F_{\gamma\mathrm{h}}}$	horizontal volumetric surface force [N m^{-3}]
$\boldsymbol{F_{\gamma\mathrm{v}}}$	vertical volumetric surface force [N m^{-3}]
g	acceleration of gravity [m s^{-2}]
H_0	initial height [m]

H_{r}	rebounding height [m]
h	height of SHS microstructure [m]
h_{i}	interfacial heat transfer coefficient [J m^{-2} s^{-1} K^{-1}]
L	latent heat of condensation of water [J kg^{-1}]
$\bar{M}$	molecular weight [kg mol^{-1}]
m	mass of droplet [kg]
$\boldsymbol{n}$	interface normal [m^{-1}]
$\widehat{\boldsymbol{n}}$	interface unit normal [m^{-1}]
$\widehat{\boldsymbol{n}_{\mathbf{t}}}$	unit vector tangential to boundary [m^{-1}]
Oh	Ohnesorge number
p	pressure [Pa]
q	heat flux [J m^{-2} s^{-1}]
R	droplet radius [m]
$\bar{R}$	gas constant [J K^{-1} mol^{-1}]
T	temperature [K]
T_{a}	air temperature [K]
T_{cell}	temperature of the computational cell [K]
T_{s}	SHS temperature [K]
T_{wd}	water droplet temperature [K]
$\widehat{\boldsymbol{t}_{\mathbf{w}}}$	unit vector normal to boundary [m^{-1}]
t_{c}	contact time [s]
t_{e}	characteristic evaporation time [s]
t_{maxr}	droplet maximum rebounding time [s]
t_{recoil}	droplet recoil time [s]
V	droplet volume [m^3]
V_{cell}	computational cell volume [m^3]
V_{ld}	liquid domain volume [m^3]
$\boldsymbol{V}$	velocity [m s^{-1}]
v	velocity [m s^{-1}]
v_{CL}	contact line velocity [m s^{-1}]

v_r	radial velocity [m s^{-1}]
v_z	axial velocity [m s^{-1}]
W_a	work of adhesion [J m^{-2}]
We	Weber number

Greek symbols

α	sliding angle [°]
α_g	gas volume fraction
α_l	liquid volume fraction
γ	surface tension [N m^{-1}]
δ	thickness of condensed water [m]
ρ	density [kg m^{-3}]
ρ_a	air density [kg m^{-3}]
ρ_g	gas density [kg m^{-3}]
ρ_l	liquid density [kg m^{-3}]
ρ_w	water density [kg m^{-3}]
ρ_{wv}	water vapor density [kg m^{-3}]
$\hat{\sigma}$	condensation accommodation coefficient
θ	contact angle [°]
θ_a	advancing contact angle [°]
$\overline{\theta_c}$	average contact angle during receding [°]
θ_r	receding contact angle [°]
θ_s	static contact angle [°]
κ	curvature of liquid-gas interface [m^{-1}]
λ	thermal conductivity [W m^{-1} K^{-1}]
λ_a	air thermal conductivity [W m^{-1} K^{-1}]
λ_w	water thermal conductivity [W m^{-1} K^{-1}]
μ	viscosity [N s m^{-2}]
μ_a	gas viscosity [N s m^{-2}]

μ_{cell}	viscosity in computational cell [N s m^{-2}]
μ_{g}	gas viscosity [N s m^{-2}]
μ_{l}	liquid viscosity [N s m^{-2}]
μ_{w}	water viscosity [N s m^{-2}]
τ	characteristic contact time [s]
ϕ	viscous dissipation function [J $\text{m}^{-3}\text{s}^{-1}$]

Abbreviations

AB	Acetylene Black
AFM	Atomic Force Microscopy
CA	Contact Angle
CAH	Contact Angle Hysteresis
CFD	Computational Fluid Dynamics
CPD	Cell Per Diameter
CSF	Continuum Surface Force
HVAC	Heating, Ventilation, and Air-Conditioning
LBM	Lattice Boltzmann Method
MD	Molecular Dynamics
RH	Relative Humidity
SHS	Super-Hydrophobic Surface
TMSS	Trimethylsiloxysilicate
VOF	Volume Of Fluid

Chapter 1 Introduction

1.1. Thesis introduction

In this thesis, the research includes four major sections:

Firstly, literatures are reviewed including the origins of SHS, fabrication methods, and related applications. Specially, the passively anti-icing capabilities of SHS are summarized. For a sessile water droplet, it is observed that ice nucleation delay and adhesion strength reduction on a cold SHS take place. For an impact water droplet, it reviews the mechanisms affecting droplet impinging behaviors. Wetting transition of an SHS under various scenarios are reviewed as well. It also reviews the numerical modellings exploring the droplet impacting performance under different circumstances.

Secondly, this research experimentally focuses on the bouncing behaviors of an impact water droplet on an SHS near freezing temperatures and the effects of SHS temperature, water droplet temperature, and droplet size. To elucidate the experimental findings, this research proposes the mechanism that condensed water within SHS micro/nano textures builds droplet-SHS water bridges and affects droplet rebounding performance. The amount of condensed water is estimated via the vapor-liquid phase transport model to validate the proposed mechanism.

Thirdly, when the condensed water accumulates inside SHS micro/nano cavities, wetting transition from the Cassie-Baxter state to the Wenzel state takes places. This research compares the wetting transition of a cold SHS induced by an impact water droplet under different experimental conditions. The water condensation also leads to the increase of adhesion between impact water droplet and SHS. Energy loss due to droplet-SHS adhesion and energy loss due to water viscosity are analyzed during droplet impact. To further validate the occurrence of wetting transition owing to condensed water, wetting transition of a sessile water droplet on an SHS near freezing temperatures is investigated and compared with the wetting transition induced by an impact water droplet.

Fourthly, CFD simulation based on VOF method is utilized to reproduce the experimental droplet impacting behaviors on an SHS near the freezing temperatures. The contact angle measured from experiments is added as a wall boundary condition to represent the degree of adhesion between droplet and SHS under different experimental conditions. Viscous loss is calculated to compare with experimental results and to validate the energy loss analysis. During the droplet spread, recoil, and rebound process, time-course viscous loss is analyzed. Besides, parametric study in consideration of the contact angle, water viscosity, surface tension coefficient is adopted to explore the dominant factor for droplet rebounding behaviors in this work. Under the experimental conditions of this research, wetting transition is found to be the dominant factor determining the bouncing or sticking performance on an SHS near freezing temperatures. When wetting transition happens, the physics influencing droplet rebounding dynamics is analyzed as well.

1.2. Research objectives and approaches

The objective of this research is to investigate the droplet impact behaviors experimentally and numerically on an SHS controlled near freezing temperatures for the sake of optimizing the SHS design in anti-icing applications.

This research proposes a previously ignored regime affecting the droplet rebound performance on an SHS near freezing temperatures. During droplet impact, water vapors evaporate from the droplet and vapors condense inside micro/nano cavities of the cold SHS. The condensed water builds droplet-SHS water bridges and increases the adhesion between impact droplet and SHS. The mathematical vapor-liquid phase transport model is employed to evaluate the amount of condensed water under different experimental conditions and validate the proposed hypothesis.

This research also aims to analyze the occurrence of wetting transition as the condensed water accumulates within SHS micro/nano cavities. Owing to the wetting transition, the impact droplet forfeits more kinetic energy during the impact process. Accordingly, there is an increase in contact time and a decrease in droplet rebounding

height. This research evaluates the energy loss due to adhesion and energy loss due to viscosity under different experimental conditions.

Moreover, the present research attempts to utilize CFD simulations to reproduce the droplet rebounding or sticking behaviors observed in experiments through adding the wetting transition as a wall boundary condition. Viscous loss is calculated numerically to analyze the droplet impacting dynamics. After that, this research aims at analyzing the dominant factor and the mechanism determining the droplet rebound via a parametric study.

The approaches employed in this research include SHS fabrication, SHS characterization, experimental measurement, mathematical modelling, and computational fluid dynamics simulation.

1.3. Thesis layout

Contents of this thesis are arranged into the following chapters:

Chapter Two

This chapter presents a review of previous literatures of SHS preparation and applications, droplet impact phenomena, wetting transition, and numerical simulations of droplet impact on an SHS.

Chapter Three

This chapter shows the experimental results of water droplet impact behaviors on an SHS near freezing temperatures. The effects of SHS temperature decrease, water droplet temperature increase, and droplet size change on the rebounding or sticking performance of the impinging water droplet are presented. Besides, the experimental findings are elucidated by the fact that during droplet impact, the condensed water inside hierarchical micro/nano textures might be accumulated and build water bridges between droplet and SHS. These water bridges increase the droplet-SHS adhesion and determine the contact

time and droplet rebounding height. Vapor-liquid phase transport model is adopted to evaluate the accumulation of water condensation under different experimental conditions to validate the proposed mechanism.

Chapter Four

This chapter shows that when condensed water accumulates within SHS micro/nano structures, wetting transition from the Cassie-Baxter state to Wenzel state takes place. This chapter also presents the wetting transition of a sessile water droplet on SHS to further validate the occurrence of wetting transition owing to the existence of condensed water on SHS. When wetting transition happens, the adhesion between droplet and SHS increases. During droplet impact process, energy analysis is carried out in consideration of energy loss due to adhesion and energy loss due to viscosity. Then water droplet impacting behaviors on an SHS near freezing temperatures are summarized, considering the amount of vapor condensation, the occurrence of wetting transitions, and energy losses.

Chapter Five

This chapter executes CFD simulations based on VOF method to reproduce droplet impacting behaviors on SHS near freezing temperatures observed from experiments. The contact angle measured from experiments is added as a wall boundary condition via the continuum surface force model and wall adhesion model. Viscous loss of the impact water droplet is evaluated to validate the energy loss analysis in experiments. Droplet impinging dynamics is analyzed in consideration of the time-course viscous loss during droplet spread, recoil, and rebound processes. Parametric study is carried out to study the influence of contact angle, water viscosity, and surface tension on droplet impact dynamics. The simulation work also shows that wetting transition is the dominant factor determining the droplet rebounding behaviors of an impact water droplet on an SHS near freezing temperatures.

Chapter Six

This chapter presents the conclusions and prospects of this research.

Chapter 2 Literature Review

Chapter 2.1 reviews the SHS originated in creatures, definitions, preparation methods, and multifunctional applications. Chapter 2.2 reviews researches about a sessile water droplet on a cold SHS. Chapter 2.3 reviews the droplet impact behaviors on a surface. Chapter 2.4 reviews the occurrence of wetting transition of an SHS under certain circumstances. Chapter 2.5 reviews the numerical simulations exploring droplet impact behaviors on a surface.

2.1. Super-hydrophobic surface

Inspired by surfaces of plants and animals in nature [1–3] (e.g., lotus leaves as shown in Figure 2.1 [3,4], rose petals [5], water strider legs [6], and butterfly wings [7]), surfaces with special low wettability [3] have attracted tremendous attentions of researchers and engineers. Through interpreting the relationship between surface textures and wettability [8,9], and mimicking the natural surface structures of creatures, artificial SHSs have been fabricated. Correspondingly, plenty of potential applications of these super-hydrophobic surfaces (SHSs) have been considered in mechanical and biological fields [1–3]. This chapter summarizes the definition of SHS, fabrication methods, and potential applications of SHS in practice.

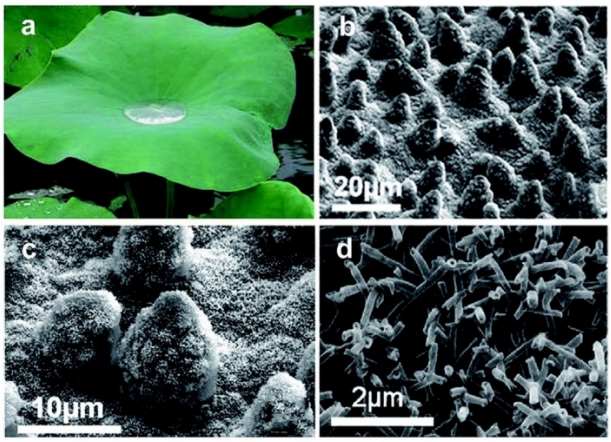

Figure 2.1 (a) Lotus leaves in nature, (b) scanning electron microscopy images of microstructures of lotus leaves, (c) scanning electron microscopy images of protrusions of lotus leaves, and (d) scanning electron microscopy images of wax tubules on lotus leaves [3].

2.1.1. Definition

An SHS is normally quantified with the static contact angle θ_S larger than 150° [1–3] based on Young's equation. For static contact angle between 90° and 150° [1–3], the surface is named as hydrophobic surface. The surface is called hydrophilic when the static contact angle is less than 90° [1–3]. The Young's equation [10] is expressed as follows showing the surface energy balance near the triple-phase contact area of a sessile water droplet on a surface as displayed in Figure 2.2,

$$\cos\theta_S = \frac{\gamma_{SA} - \gamma_{SL}}{\gamma_{LA}} \tag{2.1}$$

where γ_{SA} refers to surface energy between solid and air phases, γ_{SL} refers to the surface energy between solid and liquid phases, and γ_{LA} refers to the surface energy between liquid and air phases.

Furthermore, contact angle hysteresis and sliding angle are also adopted to characterize SHS. Contact angle hysteresis (CAH) [1–3] represents the difference between advancing contact angle θ_a and receding contact angle θ_r, which are the threshold values for the triple-phase contact line movement during droplet spreading and recoiling, respectively [1–3]. The sliding contact angle α refers to the surface tilt angle at which the droplet completely rolls off without an external force. An SHS possesses low contact angle hysteresis (< 10°) and low sliding angle (< 10°) [1–3].

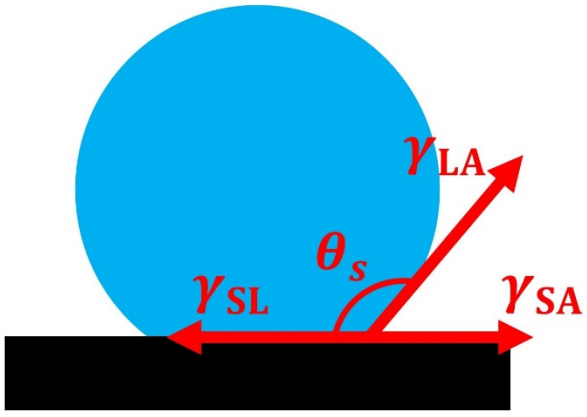

Figure 2.2 Schematic of the surface energy balance near the triple-phase contact line of a sessile water droplet on a surface.

2.1.2. Fabrication methods

The most effective approach to design and prepare superhydrophobic materials is to interpret nature to reveal the physics of super-hydrophobicity of biological organisms [11]. When fabricating artificial SHSs, there are two significant factors: hierarchical surface micro/nano textures and low surface energy [3,12]. During the past years, various methods have been employed to fabricate hierarchical surface textures, including spray coating [13,14], etching [15,16], anodic oxidation [17], crystal growth [18,19], lithography [20,21], electro-spinning [22,23], and galvanic deposition [24,25]. In nature, surfaces with extraordinary super-hydrophobicity are found to be covered with nanoscale layer of wax to decrease the surface energy [26]. In academia and industry, to reduce the surface energy of the fabricated surface, chemicals with low surface energy are adopted such as trimethylsiloxysilicate [13], tetrafluoroethylene [27], and polydimethylsiloxane [28].

2.1.3. Multifunctional applications

Owing to the low surface energy of SHS, great interests and attentions have triggered researchers and engineers to focus on harnessing SHS in a great many functional applications. The bio-adhesion between SHS and cells is weak, and thus SHS can be adopted in combination with super-hydrophilic surface to selectively separate tumor cells from normal blood cells [29,30]. Due to the decrease of bio-adhesion of surface with superb wettability, the SHS inspired by Nepenthes plants has been regarded as an ideal design of anti-biofouling or anti-bacterial surfaces [31,32]. For porous textures combining super-hydrophobicity with super-oleophobicity, they are suitable for the efficient separation of industrial water and oil [33,34]. Low-adhesion structures of SHS can also be in combination with nano-plasmonic textures or gold nanoparticles to design sensors for the sake of detecting target analytes in the fields of biomedicine and environmental monitoring [35,36]. Surfaces with great wettability have also been employed as offset printing plates where the hydrophobic graphic areas and hydrophilic non-graphic areas are occupied with oil inks and aqueous solutions, respectively [37]. Furthermore, for energy conversion devices such as nanogenerators and solar cells

[38,39], the self-cleaning SHS is proven to be a cost-effective approach to prevent the accumulation and deposition of dust particles which block the sunlight. In a nutshell, SHS is a low cost and environmentally friendly technology in many practical applications. Besides, SHSs have been widely considered in the fields of passively ant-icing [12,40]. Chapter 2.1.4 analyzes the advantages and potentials of employing SHS in anti-icing fields.

2.1.4. Anti-icing potentials of super-hydrophobic surfaces

Traditionally, several approaches [12] have been employed to prevent or remove ice formation on surfaces. For example, joule heating [41] is reckoned as the most efficient engineering method to melt the ice but the energy consumption is high and there is extra disturbance because of electromagnetic effect. Another effective and commercially available way of anti-icing is to utilize chemicals [42] with low ice nucleation temperatures. However, these chemicals cause many environmental pollutions and the requirement of periodic treatment of surfaces makes this way inefficient. Salts are also used to melt ice on roads owing to its high solubility [43], but this method contaminates the ground water and do harm to roadside vegetations. Furthermore, mechanical de-icing approaches (e.g., breaking the ice accretion directly or utilizing shock waves) are often utilized to remove ice from apparatuses [44]. Nevertheless, the mechanical de-icing sometimes is confined by the accessibility and bothered by extra disturbance. Despite there exists many conventional anti-icing and de-icing strategies, generally speaking, these methods are inefficient, energy-consuming and unfriendly to environment. It is an urgent necessity to develop an economical and environmentally harmless approach to conquer current anti-icing and de-icing problems.

To date, SHS is becoming a promising candidate for passively anti-icing [12,45]. For a sessile water droplet on an SHS in cold environment, Chapter 2.2 shows the occurrence of ice nucleation delay and the decrease of ice adhesion strength between frozen droplet and SHS. For incoming water droplet, Chapter 2.3 shows that SHS has the capability to repel the incoming droplet before the occurrence of ice nucleation. In addition, when water vapor from the ambient condenses on SHS, the self-jumping

phenomenon of condensed water drops is observed [46,47]. Due to the evaporation from water droplet and the volume increase of frozen water droplet, spontaneous droplet trampolining [48] and droplet self-dislodging [49] take place, respectively. The above-mentioned interesting phenomena make SHS full of potentials to be applied to prevent the ice formation.

2.2. A sessile water droplet on a cold super-hydrophobic surface

For a sessile water droplet on an SHS, owing to the existence of hierarchical micro/nano surface textures of SHS, there exists air pockets between droplet and SHS. As the decrease of SHS temperature to below 273 K, the air pocket layers play the role of thermal barriers and reduce the adhesion between droplet and SHS when the droplet is frozen.

2.2.1. Ice nucleation delay of a sessile water droplet on a super-hydrophobic surface

The water droplet freezing delay has been utilized to evaluate ice-phobicity of a surface. Jung et al. [50] reported that compared with untreated smooth wettable surfaces, an unexpectedly longer freezing delay of water droplet and a slower subsequent phase change are observed on non-wettable surfaces with nanometer-scale roughness.

Alizadeh et al. demonstrated that the ice nucleation delay of a supercooled water droplet can be delayed through altering the surface structure and chemistry [51]. Figure 2.3 displays the transient temperatures of a water droplet on a cold surface at -20 ℃ with different wettability from hydrophilic to super-hydrophobic. On hydrophilic surface, the ice nucleation of a sessile water droplet initiates at around 2 s. But for the droplet on hydrophobic surface, the beginning of ice nucleation takes places at around 6 s. On super-hydrophobic surface, it takes the droplet more than 80 s to start freezing. Alizadeh et al. also [51] analyzed that the obvious ice nucleation delay of a sessile water droplet on SHS is due to the limiting of heat transfer between droplet and SHS. On the super-

hydrophobic silicon substrate with nanoscale structures, the droplet requires a prolonged time period (around 20 s) to reach the substrate temperature [51].

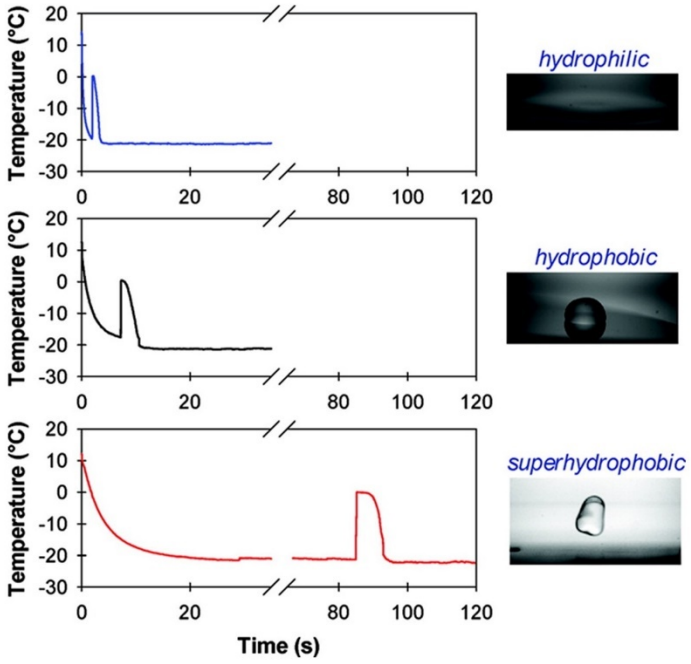

Figure 2.3 Transient temperatures of a water droplet with the volume of 4 μL freezing on hydrophilic, hydrophobic, and super-hydrophobic substrates [51].

2.2.2. Adhesion reduction between a frozen droplet and a super-hydrophobic surface

Another significant evaluation of surface ice-phobicity is the ice adhesion on a surface. For instance, Bengaluru et al. [52] experimental demonstrated that due to the formation of frost within the micro/nano textures of SHS and the stabilization of surface pockets, there is a reduction of ice adhesion on nanotextured surfaces. Meuler et al. [53] developed a custom-built laboratory-scale adhesion measurement apparatus and found that the ice adhesion strength is strongly correlated with the practical work of adhesion. As the receding contact angle reduces, the ice adhesion strength between frozen droplet and the surface increases. In addition, to further reduce the ice adhesion strength, Kim et al. [54] reported a radically different type of ice-phobic material called liquid-infused

nanostructured surfaces. Owing to the existence of liquid within nanostructured surface structures, there is a tremendous decrease in ice adhesion.

2.3. An impact water droplet on a super-hydrophobic surface

For an impact water droplet on surface with low wettability, the droplet rebounds from the surface with the energy conversions among potential energy, kinetic energy, and surface energy [55]. Chapter 2.3.1 reviews the research status of an impact water droplet on an SHS under isothermal conditions. Chapter 2.3.1 summarizes the droplet rebounding behaviors on an SHS under freezing conditions.

2.3.1. Impact behavior of a water droplet at room temperature

When a water droplet collides on an SHS, it can be divided into two phases including droplet spreading and droplet recoiling [56]. For the spreading process, the droplet undergoes an effective lateral acceleration [57] as the kinetic energy of droplet transfers into surface energy with minimal resistance [56,58]. After the maximum spreading of droplet on an SHS, the droplet tends to minimize its surface energy thus recedes on the SHS. During droplet impact, part of kinetic energy is lost due to viscosity of water droplet and adhesion between droplet and surface [55]. Depending on the surface characteristics (e.g., surface chemistry and surface roughness) and droplet properties (e.g., impact velocity, viscosity, surface tension, and droplet size), the droplet impact performance has been classified into five possible outcomes [59]: droplet deposition, droplet splashing, break-up of droplet, partial rebound, and fully rebound.

For the spreading process of an impact water droplet, maximum spreading has been intensively investigated due to its significance to many practical applications [56] (e.g., spray cooling and inkjet printing). At the moment of droplet maximum spreading, a flattened pancake shape is assumed with the balance among inertia, capillarity, and viscous dissipation [58,60]. Mathematical models [61–64] can be found in literature to evaluate the maximum spreading of an impinging water droplet on a surface. However, the droplet spreading involves a more complicated process because the droplet is not in a

flattened pancake shape at the moment of maximum spreading [65] and there is still kinetic energy remained inside the water droplet [60].

As a successive process of droplet spreading, droplet retraction starts as the droplet surface energy transfers into kinetic energy. When water droplet becomes completely rebounded from a surface, contact time is an essential parameter to evaluate the droplet rebound performance [66]. Richard et al. [66] experimentally showed that within a wide range of droplet impact velocity, the contact time is merely relevant to droplet diameter owing to the balance between inertia and capillarity. For water droplet with the diameter of millimeters, the contact time is within tens of milliseconds [66]. To reduce the contact time is one of the important goals. For example, Bird et al. [67] came up with the SHS design with both micro/nano scale structures and macroscopic features to promote non-axisymmetric recoil for the sake of shortening the droplet-surface contact time. Liu et al. [68] developed SHS with microscale textures close to capillary length, and pancaking bouncing is observed so that the contact time is reduced tremendously. In addition, to enhance the functionality of SHS in practical applications, the droplet impact behaviors on inclined SHSs [69–71] or cylindrical SHSs [72–73] have been studied broadly. For instance, Ding et al. [69] studied the droplet impacting and freezing behaviors on an SHS at supercooled temperatures. Ding et al. [72] investigated the droplet impact performance and the occurrence of droplet break-up on a cylindrical SHS.

2.3.2. Impact behavior of a water droplet under freezing conditions

The other important aspect of ice-phobicity of SHS is the capability of repelling incoming water droplets under freezing conditions. Because of the ice nucleation delay of a water droplet on a cold SHS and the short contact time of an impact water droplet on an SHS, an impinging water droplet still demonstrates its capability to rebound from cold SHSs [74]. Lv. et al. [12] summarized that if the time of an impact droplet completely recoiling form a cold SHS is shorter than the time required for the ice nucleation of the droplet, the droplet can rebound from a cold SHS. As shown in Figure 2.4, Mishchenko et al. [74] displayed the sticking of a supercooling water droplet on an SHS at -25℃ and explained that the ice nucleation was the dominant factor [75]. Besides, Zhang et al. [76]

investigated the collision of a supercooled water droplet on an SHS at freezing temperature and concluded that droplet ice nucleation causes adhesion to the surface. Ding et al. [77] measured the rebounding height of a supercooled impinging water droplet and observed that the droplet forfeits rebounding capacity because of ice nucleation when residual kinetic energy is less than 35 %. Shen et al. [78] observed that cold SHS hinders triple-phase contact line movement and the contact time increases because of electrostatic interaction caused by ice nucleation.

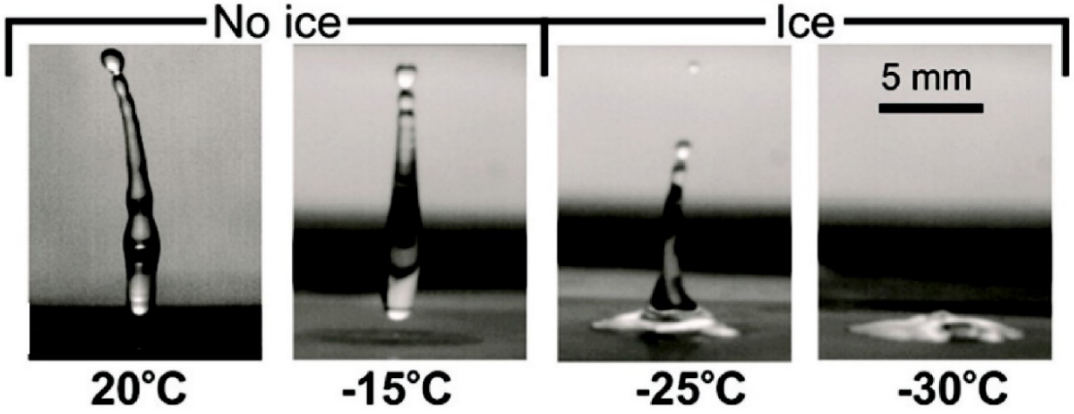

Figure 2.4 Rebounding behaviors of a supercooled water droplet at -5 ℃ on an SHS with different temperatures from 20 ℃ to -30 ℃. Complete droplet rebound on an SHS without ice formation at surface temperature 20 ℃ and -15 ℃. Droplet attachment on an SHS with ice formation at surface temperature -25 ℃ and -30 ℃ [74].

2.4. Wetting transition of a super-hydrophobic surface from the Cassie-Baxter to Wenzel state

For both sessile water droplets and impact water droplets on an SHS, under certain circumstances, wetting transition happens from Cassie-Baxter state to Wenzel state, changing the super-hydrophobicity of the surface. Figure 2.5 shows the schematic diagram of the Cassie-Baxter state and Wenzel state of a sessile water droplet on an SHS. For Cassie-Baxter state [79], air remains trapped inside the surface pockets between droplet and surface. Wenzel state [80] refers to the state when the air pockets of SHS are occupied with water.

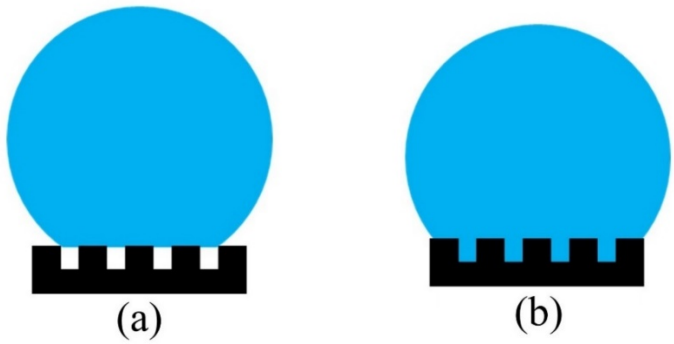

Figure 2.5 Schematic diagram of the Cassie-Baxter state and Wenzel state of a sessile water droplet on an SHS. (a) Cassie-Baxter state, (b) Wenzel state.

2.4.1. Wetting transition induced by a sessile water droplet

For a sessile water droplet, when the SHS temperature is controlled lower than the temperature of water droplet, water condensation within SHS micro/nano structures causes the wetting transition from Cassie-Baxter state to Wenzel state [81–83]. Heydari et al. [81,82] measured the receding contact angle of a sessile water droplet on an SHS at temperature lower than the droplet temperature. As the surface temperature decreases, the receding contact angle of water droplet on SHS decreases tremendously but remains nearly unchanged on hydrophobic surface without micro/nano structures and proposes that this receding contact angle change is due to the wetting transition from Cassie-Baxter state to Wenzel state [81,82]. Bahadur et al. [84] presented an SHS design with some nanoscale roughness to prevent the occurrence of wetting transition. With the help of environmental scanning electron microscopy, Wen et al. [85] showed the condensing condition-induced wetting transition, leading to the loss of surface super-hydrophobicity. Through measuring the sliding angles of a sessile water droplet on a surface, Zhao et al. [86] showed that SHS with densely packed nano-asperities can remain in a stable Cassie-Baxter state but Wenzel state takes places on SHS with coarsely packed nano-asperities. To enhance the droplet drying on SHS, Gerber et al. [87] developed an SHS on which the Cassie-Baxter state can be maintained during the drying process.

2.4.2. Wetting transition induced by an impact water droplet

For an impact water droplet, although the contact time is merely in the time scale of millisecond, wetting transition from Cassie-Baxter to Wenzel state has been observed in literatures. Mouterde et al. [88] investigated the rebound or sticking behaviors of a hot impact water droplet on hydrophobic surfaces with various dimensions of surface textures as shown in Figure 2.6 [88]. Figure 2.7 [88] displayed the regime that during droplet spreading there is a growing condensation nucleus formed inside surface cavities causing the wetting transition from Cassie-Baxter state to Wenzel state. Mouterde et al. [88] explained that for small SHS textures (~100 nm) the formed water bridge is extremely weak so the impact droplet water rebounds, but for large SHS textures (~10 μm) the condensed water is inadequate to build solid water bridges between droplet and surface so the droplet can rebound. Shiri et al. [89] also demonstrated the wetting transition when a hot water droplet impacts on an SHS and explained that the hot water droplet might also melt the surface micro/nano textures.

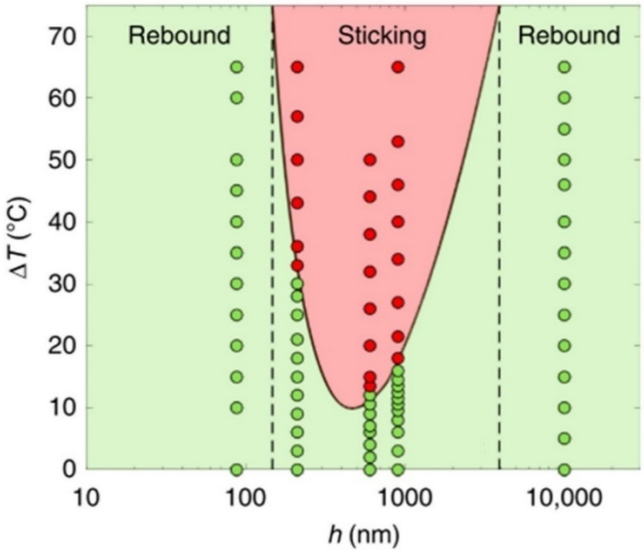

Figure 2.6 Phase diagram of a hot impact water droplet rebound or sticking behaviors on hydrophobic textures as the dimension of substrate textures h and water/substrate temperature difference $\triangle T$ changes [88].

Droplet impalement [90–92] is another scenario causing the wetting transition of an impact water droplet on an SHS. When the impact water droplet impales into SHS

micro/nano textures (e.g., due to high velocity), wetting transition from Cassie-Baxter state to Wenzel state takes place. Bartolo et al. [90] proposed a semi-quantitative model to account for the relationship between surface topography and non-wetting states and presented some guidelines to design robust SHSs. Vasileiou et al. [91] and Maitra et al. [92] studied the impact behaviors of a supercooled water droplet on an SHS with the occurrence of wetting transition due to droplet penetration. Furthermore, the viscosity increment of supercooled water is shown to weaken the influence of droplet penetration. Jung et al. [93] investigated the relationship between SHS parameters and droplet impact velocities and proposed a criterion for wetting transition from Cassie-Baxter regime to Wenzel regime.

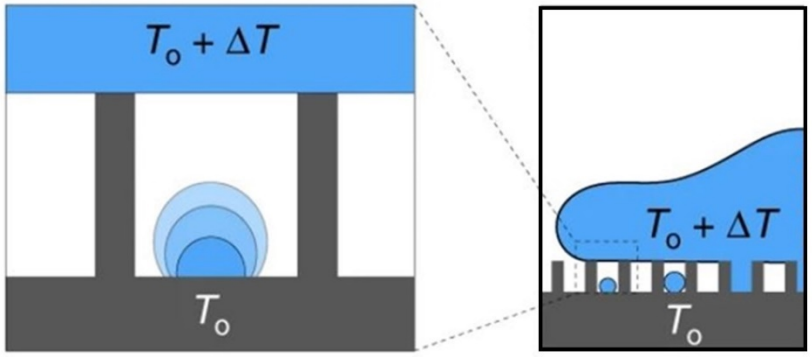

Figure 2.7 Schematic diagram of a spreading water droplet on a hydrophobic surface and an elementary SHS cell including a growing condensation nucleus fed by the hot impact water droplet above [88].

2.5. Numerical investigation of droplet impinging phenomena on surfaces

Theoretically modeling and numerically simulating the droplet impact process on a rigid surface plays a critical role in understanding this phenomenon, where experiments are challenging to be executed [94]. This chapter reviews the numerical methods employed in literatures and current research progresses in investigating droplet impact behaviors on surfaces.

Previously, mainly three simulation methods have been carried out including computational fluid dynamics method, lattice Boltzmann method (LBM), and molecular dynamics (MD) method. In CFD simulations, the volume of fluid (VOF) method [95] and level set method [96] have been widely employed to capture and track the liquid-gas interfaces. CFD simulations [97–100] have been employed to investigate droplet impact behaviors under isothermal conditions. For example, the maximum spreading of an impact droplet on surfaces are investigated numerically [63,73,97], the increment of droplet surface tension [73,97] and viscosity confine droplet maximum spread due to the surface energy increase and viscous loss increase [63], respectively. Qu et al. [98] demonstrated the impacts of Weber number on droplet maximum spreading and the occurrence of droplet splashing as the Weber number increases to 197.5. Farhangi et al. [99] numerically displayed the bouncing of droplets owing to coalescence between an impact water droplet and a sessile water droplet on an SHS. Lunkad et al. [100] and Liu et al. [73] utilized CFD simulations to study the droplet spreading dynamics on inclined surfaces and spherical surfaces, respectively.

For the impingement of a water droplet on a supercooled surface, several numerical works [101–104] takes the droplet freezing into consideration with the assumption that ice nucleation occurs instantly when the droplet contacts the supercooled surfaces. Specifically, Zhang et al. [101] numerically compared the effects of surface temperature and droplet temperature on droplet rebound and adhesion behaviors when ice nucleation takes place. Chang et al. [102] focused on the droplet maximum spreading dynamics affected by the droplet freezing, Yao et al. [103] studied the impact behaviors on an inclined supercooled SHS, and Attarzadeh et al. [104] investigated the ice-phobic performance of an SHS when a micro-meter droplet impinges on it.

When a water droplet collides with hot surfaces, due to droplet evaporation there is an insulating vapor layer between the droplet and surface, and this phenomenon is named as Leidenfrost effect [105]. Some mathematical works [106–110] consider the influence of Leidenfrost effect on droplet impact performance on hot surfaces. Nikolopoulos et al. [106] and Strotos et al. [107,108] explored the cooling effectiveness of a liquid droplet during its collision on a hot substrate as the evaporation takes place, and further

investigated the impacts of surface temperatures and Weber numbers. Harvie et al. [109,110] studied the droplet impact dynamics on a hot surface through applying an additional vapor layer and adding a force to the lower surface of the droplet at the interface region because of droplet evaporation.

In addition, Tanaka et al. [111] used the LBM method to simulate the dynamic behavior of a droplet on a solid surface incorporating the wetting boundary conditions and found the simulation results were in good agreement with experimental outcomes with various Weber numbers. Chen et al. [112] compared droplet vertically separating with laterally sliding on substrate via the LBM method and concluded that vertical adhesion force and lateral adhesion force depend more significantly on the contact area and contact line, respectively. Zhang et al. [113] carried out simulations of a microscopic drop impact on wettable and textured surfaces with the LBM method and MD method, and they observed that at low impact velocities these two methods agree well in terms of droplet impact behaviors.

2.6. Summary

This chapter presents a review of previous literatures about SHS definition, SHS fabrication, practical applications, anti-icing potentials for sessile water droplets, droplet impact behaviors on SHSs, wetting transition of SHS, and numerical works of droplet impact phenomena. Artificial SHSs can be prepared through combining hierarchical surface roughness with chemicals of low surface energy. Also, SHS shows its great potentials to be adopted in anti-icing applications.

However, the literature review reveals that the underlying physics dominating the rebounding behavior of an impact water droplet on an SHS near the freezing temperatures is still poorly understood in the existing studies, particularly when there is a large temperature difference between droplet and SHS. For SHS near freezing temperatures, ice nucleation of the water droplet might not be the only factor determining the droplet rebounding performances. The occurrence of vapor condensation inside SHS

micro/nano textures [88,89] of SHS near freezing temperatures might also affect droplet rebounding and alter the surface super-hydrophobicity.

In addition, the literature review shows that current numerical works mainly seek to reproduce the experimental observations but neglect the analysis of physics determining the droplet impact behaviors. Moreover, the available numerical works focus on non-bouncing impact droplets, there is a lack of analyzing bouncing states in literature [94], which will be beneficial to SHS designs.

Chapter 3 Experimental Study on a Water Droplet Impact on a Cold Super-Hydrophobic Surface

3.1. Introduction

In cold environments, ice accumulation and frost formation on solid surfaces cause inconvenience in our daily life, safety issues, and economic losses [12]. A thin layer of ice could result in traffic accidents due to slippery road [40]. The icing on aircraft wings or railway tracks may cause disastrous crashes [114]. In addition, ice formation in various engineering applications including automobile windshields, satellites, aviation, power transmission lines, refrigeration, and food preservation has severe effects on their operational efficiency and safety [115,116]. Formation of condensates and their subsequent freezing within the duct and on piping of a heating, ventilation and air-conditioning (HVAC) system may lead to substantial reduction of heat transfer efficiency [46,47] as well.

Albeit there exist a great many anti-icing strategies, including joule heating [41], chemical additives [117], and mechanical deicing methods [44], development of new methods capable of demonstrating higher efficiency, inexpensiveness, and better environment benignness is still necessary. A recent promising passive strategy for anti-icing adopts super-hydrophobic surfaces (SHSs) to prevent ice formation with the help of hydrophobic chemicals [118] and micro/nano surface textures [118]. Inspired by super-hydrophobicity of surface structures of plants and animals [35], SHSs have gained great attentions from both academia and industries [3].

In nature, icing originates from condensed or impinging water droplets [12], and thus, the prevention of ice nucleation from these two types of water droplets has been widely studied. For condensed water droplets on an SHS, owing to the existence of air pockets and small contact areas between droplet and SHS, the SHS could effectively prevent sessile water droplets from freezing [50,119,120]. To date, a well-known

phenomenon in this regard is the delaying of ice nucleation on various types of surfaces, such as bi-philic surfaces [119], surface made of water-repellent materials [120] and various coated surfaces [50]. In addition to ice nucleation delay, studies related to adhesion strength decrease between frozen water droplets and an SHS are common in literature [121–123]. Richard et al. [55] showed that an impinging water droplet rebounds on hydrophobic surfaces at room temperature. The contact time, recorded from the beginning of droplet spread to the end of droplet recoil, is a critical parameter in assessing droplet rebound dynamics, which can be evaluated by balancing inertia with capillarity [66]. Since the contact time during the first rebound of a millimeter-sized water droplet impinging on SHS is usually in the order of a few milliseconds [66,67], under freezing conditions such a droplet still has a great potential to rebound from SHS.

In literature, three mechanisms have been studied to comprehend droplet rebounding or sticking dynamics on an SHS under freezing conditions: (1) ice nucleation, (2) viscosity increase of supercooled water, and (3) wetting transition from Cassie-Baxter state to Wenzel state induced by droplet impalement. Regarding the first mechanism, initially, Mishchenko et al. [74] demonstrated that a supercooled impacting water droplet at 268 K bounces off an SHS at 258 K, but adheres to the SHS at 248 K. Using a predictive model considering droplet impact dynamics [55], heat transfer, and heterogeneous nucleation theory [75], it was believed that ice nucleation occurs before a droplet fully bounces off an SHS. The second mechanism hindering the impinging water droplet from rebounding is the viscosity increment of supercooled water [124]. The increase of viscosity consumes considerable kinetic energy during the impacting process [48]. For instance, Maitra et al. [125] showed that compared with a water droplet at 273 K, when a droplet at 256 K collides on SHS, a threefold increment in viscosity was observed, prohibiting the droplet recoiling processes. The third mechanism suppressing droplet bouncing is related to the wetting transition caused by droplet impalement. The complete rebound of an incoming water droplet requires a stable Cassie-Baxter state on an SHS [45]. If a droplet collides with SHS with sufficiently high impact velocity, it can fill the voids between SHS hierarchical textures, resulting in a transition from Cassie–Baxter state to Wenzel state [126], which is known as droplet impalement. There exists a critical Weber number (i.e., the ratio of fluid’s inertia to its surface tension,

mathematically expressed as, $We = \rho v^2 D/\gamma$, e.g., 227 [127]) for droplet impalement, beyond which the droplet wets SHS partially or fully [125]. However, all the above-mentioned studies were conducted under sufficiently low humidity conditions as the voids in frigid cold SHS textures became vulnerabilities under harsh environments. At high humidity, the condensation or frost formation of ambient water vapors inside micro/nano hierarchical structures of SHS at temperatures lower than dew point could prevent droplet from rebounding [52,121,129,130]. In the past decade, many researchers investigated the droplet rebounding or sticking mechanism in cold environments including the ice nucleation, viscosity increment, and droplet impalement. However, the mechanism affecting the bouncing behaviors of an impinging droplet on an SHS near the freezing point remains poorly understood.

Previously, Mouterde et al. [88] and Shiri et al. [89] investigated the rebounding behaviors of a hot impinging water droplet on hydrophobic surfaces influenced by vapor condensation inside surface cavities. Naveen et al. [130] investigated the effect of droplet temperature and surface wettability on impact dynamics of a single drop for a wide range of droplet temperatures and weber numbers spanning from 278 K to 358 K and 14.5 to 160, respectively. Their results showed that with an increase in the droplet temperature, the spreading factor also increases which is resulted in from the combined effects of decrease in the density, the surface tension, the viscosity, and the contact angle of solid surfaces. Alizadeh et al. [131] studied the temperature dependence of impact dynamics of water droplets on both hydrophilic and super-hydrophobic surfaces and for droplet temperature spanning from below freezing point to near boiling point. Their results revealed that for a hydrophilic surface at a lower temperature, retraction become more difficult.

From the survey of literature, it is evident that majority of the above studies were conducted under typical conditions where both the droplet and substrate were maintained at a very low temperature (i.e., ΔT between droplet and substrate was noticeably small). In reality, the initial temperature of a water droplet can be substantially high or even equal to its ambient, while the substrate temperature can be noticeably low in the subzero temperature region. Therefore, the present work focuses on evaluating the bouncing behavior of an impinging water droplet under the scenario of large ΔT between droplet

and substrate, which have not yet been clarified in detail in existing literature. By investigating the effects of decreasing SHS temperature and increasing droplet temperature and droplet diameter on the rebounding behavior of water droplet on an SHS, this study demonstrates that when a water droplet at relatively higher temperature impinges on an SHS maintained at much lower temperature, evaporation takes place from the droplet. Because SHS temperature is less than water droplet temperature, the evaporated water vapors might condense within the micro/nano surface cavities of SHS, and water bridges could be formed. The adhesion between the impinging droplet and the water bridges within micro/nano surface cavities results in the loss of rebounding capability of droplet since more energy is spent due to adhesion increase during the recoil process and less energy is available for rebounding. We anticipate that the outcome of this study will be helpful to provide valuable insights on how to improve performance of SHS to repel incoming water droplet in the field of anti-icing.

3.2. Experimental section

Chapter 3.2.1 introduces the materials utilized to prepare SHSs, Chapter 3.2.2 presents the fabrication methods, and Chapter 3.2.3 characterizes the wettability of prepared SHS. Then the procedures of carrying out droplet impact experiments on an SHS near freezing temperatures are summarized in Chapter 3.2.4.

3.2.1. Materials

To fabricate SHS, this study employed a simple nanoparticle-spraying method developed by Ogihara et al. [13,14]. This fabrication method was selected for the great mechanical properties of fabricated SHS and low fabrication cost [13,14]. The following chemicals were used as super-hydrophobic coatings: acetylene black (AB, Denki Kagaku Kogyo), trimethylsiloxysilicate (TMSS, KF-7312J, Shin-Etsu Chemical), and ethanol (99.5 %, Kanto Kagaku). In addition, copper sheets (Furukawa Electric) were used as the substrate on which chemicals were spray coated. The chemicals utilized in this work are summarized and listed in Table A.1.

3.2.2. Super-hydrophobic surface preparation

AB nanoparticles were utilized to create micro/nano hierarchical surface structures, and TMSS was introduced to achieve low surface energy. Figure 3.1 illustrates the SHS preparation procedures. First, a copper sheet with the dimensions 30 mm × 30 mm × 1 mm was thoroughly cleaned with ethanol, and then a nanoparticle suspension was sprayed on this sheet. The suspension consisted of 0.165 g of AB, 0.5 ml of TMSS, and 4.5 ml of ethanol. After stirring with magnetic stirrer (Remix RSH-4DN, AS ONE) at 200 rpm at 303 K for 10 min and sonicating via ultrasonic disperser (UH-50, SMT Co. Ltd.) at room temperature for 5 min, the suspension was sprayed over the copper substrate from a distance of ~20 cm using a laboratory reagent sprayer (glass with rubber bulb), and then dried at room temperature. The spray-coating process was repeated around 20 times. Eventually, the copper substrate with a super-hydrophobic coating was placed horizontally and dried at room temperature for approximately 48 h.

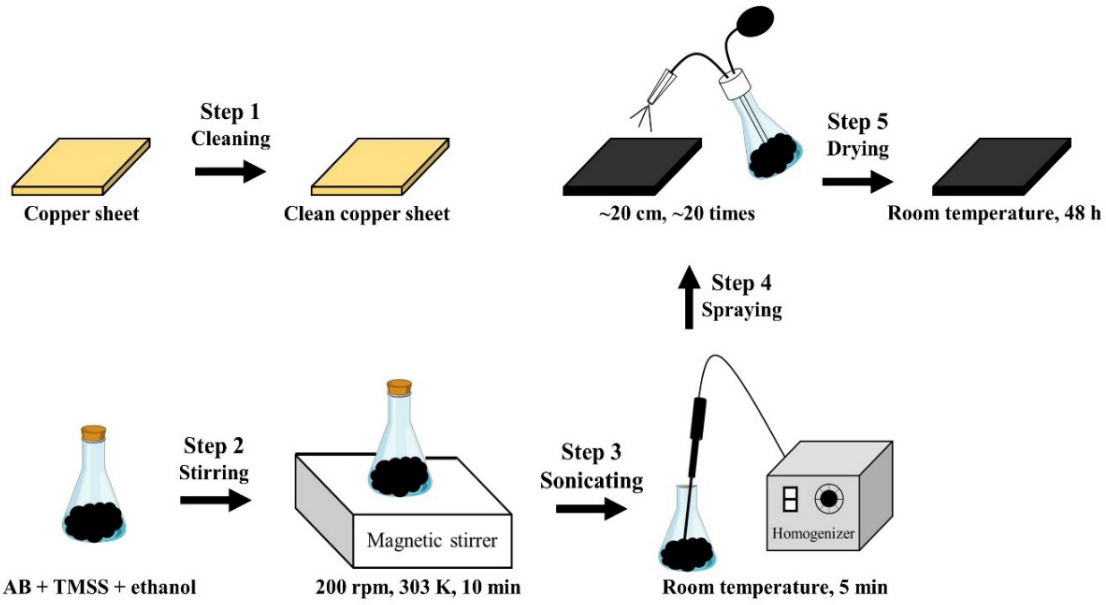

Figure 3.1 Schematic of the fabrication procedures of super-hydrophobic surfaces via spray-coating methods. Step 1: Clean the copper sheet with ethanol. Step 2: Stir the suspension of acetylene black, trimethylsiloxysilicate, and ethanol via magnetic stirrer. Step 3: Sonicate the suspension by homogenizer. Step 4: Spray the suspension over copper substrate with reagent sprayer. Step 5: Dry the substrate coated with the suspension at room temperature.

3.2.3. Super-hydrophobic surface characterization

A thermal field-emission electron microscope (JSM-7100F, JEOL) was used to observe the prepared SHS morphology, as shown in Figure 3.2. The images illustrate that the fabricated SHS was formed by particles with a diameter of approximately 50 nm, constituting micro/nano surface structures with the dimension ranging from 50 nm to 10 μm. In addition, Figure 3.3 displays the SHS topography taken by the atomic force microscopy (AFM, MFP-3D Infinity, Oxford Instruments). The average height of the micro/nano textures of the SHS under this study was 5.92 μm, which was measured by AFM analysis using a software (WSxM 4.0 Beta). Appendix A introduces the prepared SHS topography and parameters of surface structures analyzed via the WSxM 4.0 Beta software. Base on the SEM and AFM images, when a droplet is generated on the SHS, there will be air pockets between droplet and SHS.

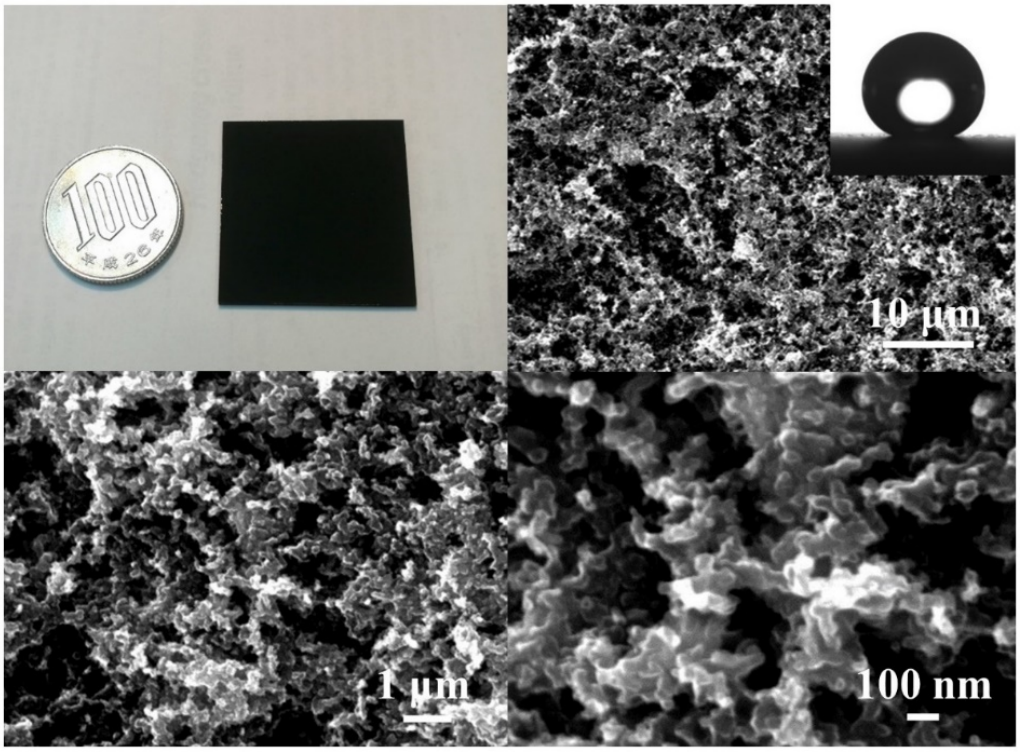

Figure 3.2 Super-hydrophobic surface morphology measured via the thermal field-emission electron microscope.

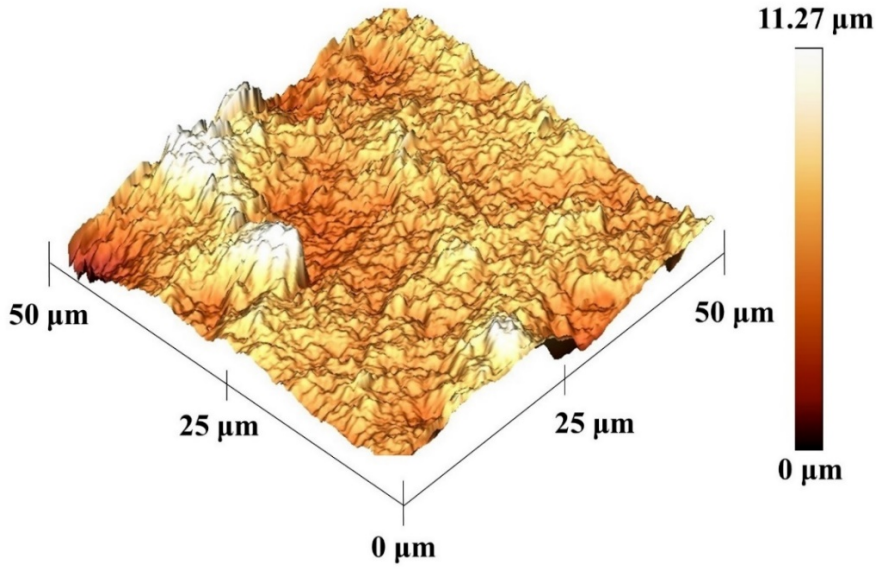

Figure 3.3 Super-hydrophobic surface topography analyzed via the atomic force microscopy.

A contact angle meter (Dmo-501, Kyowa Interface Science) was used to evaluate the surface super-hydrophobicity, including the static contact angle (θ_s), advancing contact angle (θ_a), receding contact angle (θ_r), contact angle hysteresis, and droplet sliding angle (α), using the tilting cradle method. Details of the tilting cradle method is explained in Chapter 4.2.2.

In this work, various contact angles including static, advancing, receding, and tilt angles of water droplets having different diameters D_S, D_M, and D_L were measured and the results are tabulated in Table 3.1. Tilting speed of the cradle is at 0.1 ° s^{-1}. During contact angle measurement, the temperatures of SHS and the ambient environment were controlled at 283 ± 0.2 K and 278 ± 0.2 K, respectively, and the ambient relative humidity was maintained within the range between 2–5 %. Due to the non-uniformity of SHS, contact angles were measured randomly on three different locations of SHS and the represented value is the average of three measurements. From the table, there are slight variations in contact angle hysteresis values for different droplet diameters which may

come from the uncertainties related to random measurement locations on SHS and non-uniformity of the SHS textures. Appendix B shows the measurements of contact angles of sessile water droplets with different diameters on SHS.

Table 3.1 Experimental measurement results of super-hydrophobicity of the prepared super-hydrophobic surface.

Contact Angles	D_S	D_M	D_L
Static contact angle, θ_s	157.1° ± 0.2°	156.9° ± 0.4°	157.2° ± 0.4°
Advancing contact angle, θ_a	160.6° ± 0.7°	161.4° ± 0.7°	161.0° ± 0.5°
Receding contact angle, θ_r	154.9° ± 0.7°	155.2° ± 0.3°	156.2° ± 0.4°
Contact angle hysteresis	5.7° ± 0.5°	6.2° ± 0.4°	4.8° ± 0.1°
Sliding angle, α	5.2° ± 1.1°	5.9° ± 0.6°	2.2° ± 0.6°

In this work, to generate millimeter-sized droplets of various diameters three different needles were used. The corresponding volume and size of droplets produced by each needle is summarized in Table 3.2. Dimensions of the generated droplet in this work were measured in triplicate.

Table 3.2 Needles used in this study and the corresponding volumes and diameters of three different water droplets produced.

Needle Model	Volume (μL)	Diameter (mm)
Stainless needle 32G (Kyowa Interface Science)	V_S = 4.67 ± 0.07	D_S = 2.07 ± 0.01
Injection Needle Subcutaneous 2-5635-01 (Tsubasa Industry Co., Ltd.)	V_M = 7.63 ± 0.07	D_M = 2.44 ± 0.01
Stainless needle 18G (Kyowa Interface Science)	V_L = 14.03 ± 0.17	D_L = 2.99 ± 0.02

3.2.4. Experimental setup for droplet impact experiment

The experimental setup to investigate the dynamic impinging performance of a water droplet on SHS is illustrated in Figure 3.4. Experiments were conducted in a chamber (PL-3J, Espec) with a dry gas supply system, inside which the ambient temperature and relative humidity respectively, were controlled within the range 278–293 K and 2–5 %. A humidity sensor (Hygrolog-HL-NT3, Rotronic Instruments) was employed to simultaneously measure the ambient temperature and relative humidity. A custom-developed droplet generator connected with a syringe pump (PHD Ultra, Harvard Apparatus) was used to dispense water droplets from an adjustable height. Three different needles were used to generate millimeter-sized droplets with various diameters, as listed in Table 3.2. The SHS was placed on a Peltier cooling stage (VTH3500, VICS), which could precisely control the temperature of SHS by means of a microcontroller within the range 248–373 K. The water droplet temperature was in equilibrium with the ambient temperature inside the chamber. Thus, by altering the ambient temperature inside the chamber, droplet temperature could also be altered. Two K-type thermocouples (National Instruments) were employed after calibration, one to SHS and another to droplet generator, to measure T_s and T_{wd}, respectively. The thermocouple on the SHS was attached at a location far enough from the point of droplet impinging. All the experiments were carried out when the temperature of SHS, ambient temperature and relative humidity (RH) inside the chamber reached a steady state. In a steady state, both SHS and ambient temperature varied within ± 0.2 K and ambient RH was maintained within 2–5 %. A high-speed camera (Mini AX200, Photron Fastcam) capable of recording at 4000 fps was used to capture and record the droplet spreading, recoiling, and rebounding behaviors on the SHS. Cold light was employed as the backlight for the impinging water droplet on SHS.

During experiment, SHS temperature T_s was varied from 283 K to 248 K and the droplet temperature T_{wd} was varied from 278 K to 293 K. A constant dispensing height of 16.4 mm was maintained for impinging water droplet throughout the experiments. Thus, the Weber number for the experiment was approximately 10. This small Weber number was chosen to avoid the possible droplet impalement under high impact velocity.

The low ambient relative humidity condition (2–5 %) was chosen to avoid the condensation of water vapor on SHS from the ambient.

During the experiment, T_s was initially set to a value of 10 K higher than the ambient temperature to prevent the deterioration of surface super-hydrophobicity caused by ambient vapor. Once the ambient relative humidity was stabilized within 2–5 %, T_s and T_{wd} were tuned to desired values. Then, experiments were conducted by releasing a deionized water droplet. The high-speed camera captured the dynamics of droplet collision on SHS. The experiment for each condition was repeated three times on random locations of SHS to ensure repeatability of data. In this work, to ensure the mechanical property and wettability of SHS, the SHS is utilized at maximum of 8 sets of experiments, provided that there is no evident damage on the SHS. All the relevant experimental parameters along with their measurement uncertainties are summarized in Table 3.3. All the experimental apparatuses employed in this work are summarized and listed in Table A.2.

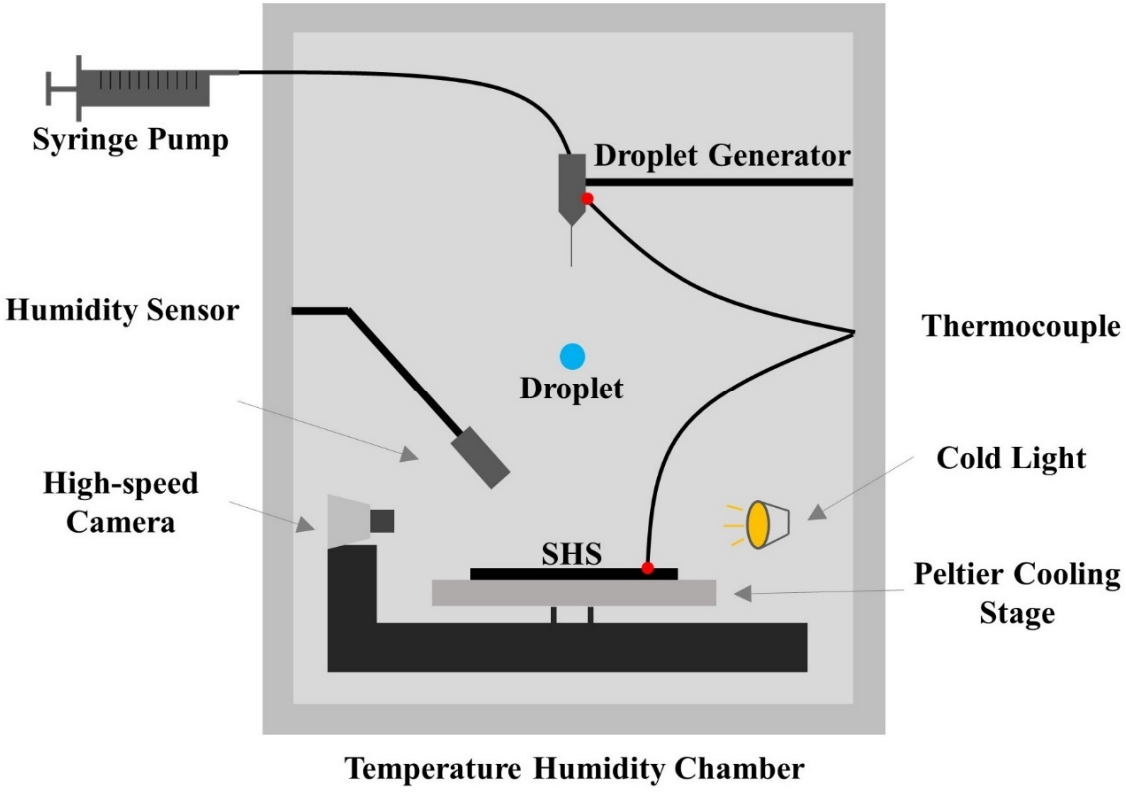

Figure 3.4 Schematic diagram of the experimental setup for a water droplet impinging on a super-hydrophobic surface.

Table 3.3 Summary of the parameters involved in the experiments of a water droplet impinging on a super-hydrophobic surface.

Droplet volume, V	V_S = 4.67 ± 0.07 µL
	V_M = 7.63 ± 0.07 µL
	V_L = 14.03 ± 0.17 µL
Droplet diameter, D	D_S = 2.07 ± 0.01 mm
	D_M = 2.44 ± 0.01 mm
	D_L = 2.99 ± 0.02 mm
Droplet temperature, T_{wd}	278, 283, 293 ± 0.2 K
SHS temperature, T_s	283 to 248 ± 0.2 K
Relative humidity, RH	2–5%
Water density, ρ_w	998 kg m^{-3}
Surface tension [132], γ (at 278 K)	$7.49e^{-2}$N m^{-1}
Surface tension, γ (at 283 K)	$7.42e^{-2}$ N m^{-1}
Surface tension, γ (at 293 K)	$7.28e^{-2}$N m^{-1}
Acceleration of gravity, g	9.8 m s^{-2}
Weber number, We	~10

3.3. Experimental results

To investigate the rebounding or sticking mechanism of an impinging water droplet on SHS near the freezing point, the effects of decreasing SHS temperature T_s (Chapter 3.3.1) and increasing water droplet temperature T_{wd} (Chapter 3.3.2) and droplet size D

(Chapter 3.3.3) on the droplet impact behaviors were investigated. In the present work, only first rebound was considered for analysis. Chapter 3.3 summarizes the key experimental observations. The underlying mechanism is described in Chapter 3.4.

3.3.1. Effect of super-hydrophobic surface temperature on droplet impact behaviors

The influence of decreasing SHS temperature on droplet rebounding behavior was investigated using a water droplet with diameter D_{M} and at a constant droplet temperature 278 K, while the temperature of the SHS was gradually decreased from 283 K to 248 K as shown in Figure 3.5. The moment of initial contact between the impinging water droplet and SHS was defined as 0 ms. Because the spreading of the droplet is mainly governed by inertia [55], the duration for the impacting droplet to reach its maximum spread diameter on SHSs maintained at different temperatures was almost the same (4 ms), followed by droplet recoiling. Figure 3.5 also shows the moments of minimum contact of the droplet with SHS, and further complex rebound, partial rebound with droplet break-up and no rebound at various T_{s}, during the recoiling process. The partial rebound with droplet breakup occurred at T_{s} = 253 K (Figure 3.5g) and at T_{s} = 248 K, the droplet completely attached to SHS without rebounding (Figure 3.5h).

A summary of the droplet-SHS contact time (t_{c}) and rebounding height (H_{r}) for different SHS temperatures are shown in Figure 3.6. Here, t_{c} refers to the duration from the moment droplet first touched the SHS to the moment before it rebounded from the SHS, which is in the order of millisecond in present work. H_{r} refers to the distance between the SHS and the very bottom of droplet when the droplet reached a maximum height after the first rebound on the SHS.

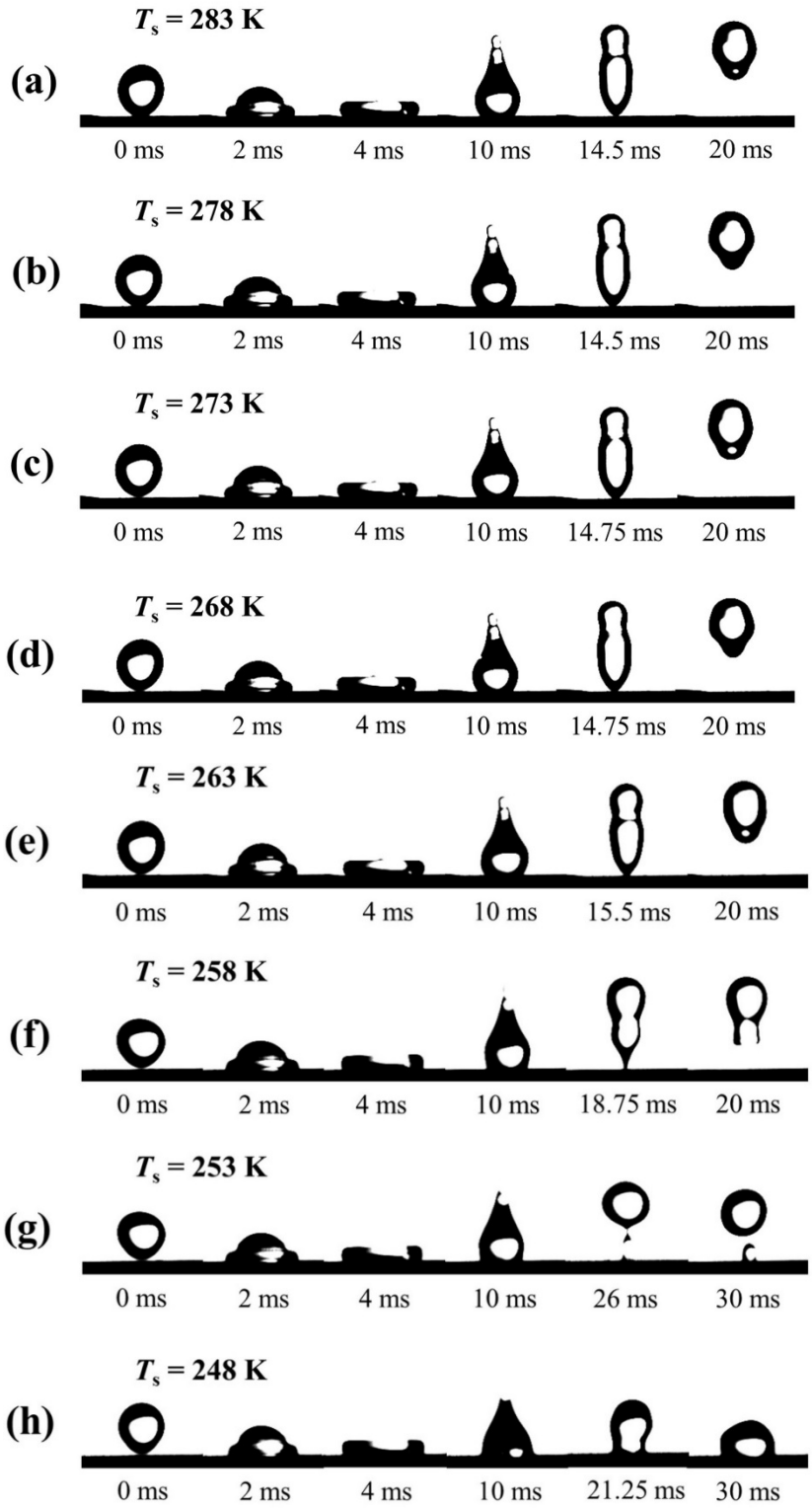

Figure 3.5 Side-view images depicting the impact behaviors of a water droplet with diameter D_M and temperature T_s = 278 K impinging on an SHS at T_s of (a) 283 K, (b) 278 K, (c) 273 K, (d) 268 K, (e) 263 K, (f) 258 K, (g) 253 K, and (h) 248 K.

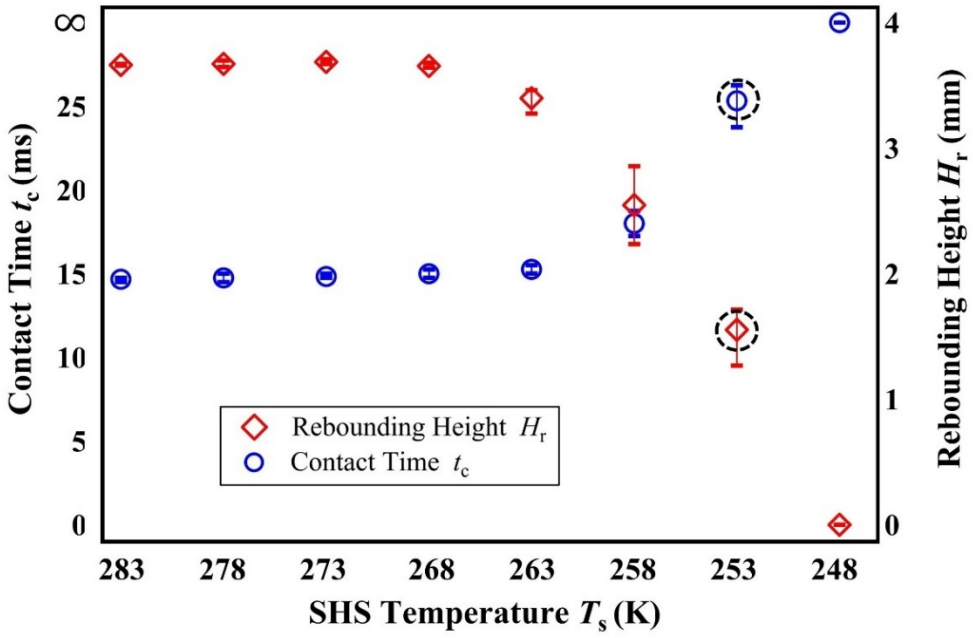

Figure 3.6 Contact time t_c and rebounding height H_r of a water droplet with diameter D_M and temperature T_{wd} = 278 K impinging on an SHS at T_s = 283–248 K. Dashed circles indicate the occurrence of droplet break-up. For each condition, the experiments were conducted three times at different positions on SHS.

The experimental results showed that the water droplet impinging on SHS with various values of T_s exhibits distinct phenomena. For example, when T_s was controlled between 283 K and 268 K, the droplet impinging performance, contact time, and rebounding height were almost identical. As T_s decreased to 263 K, the impinging water droplet displayed a small increase in contact time and a modest decrease in rebounding height. Note that at T_s = 258 K, the impinging water droplet adhered to the SHS for a longer time and a significant reduction in rebounding height was observed in comparison to those at higher surface temperatures. With a further decrease in T_s to 253 K, partial rebound with droplet break-up was observed. Finally, the impinging water droplet adhered to surface and lost its rebounding capability at 248 K. Thus, on a cold SHS, with a decrease in SHS temperature, the impinging water droplet remained adhering on the surface for a longer time and rebound lower height and eventually failed to rebound from the SHS.

3.3.2. Effect of water droplet temperature on droplet impact behaviors

The effect of increasing water droplet temperature on rebounding behavior was investigated by using a water droplet of diameter D_M maintained at three different droplet temperatures (i.e., 278, 283, and 293 K) and impinged on SHSs maintained at four different temperatures (i.e., 283, 268, 263 and 258 K), as shown in Figure 3.7. When T_s was controlled at 283 K, for all values of T_{wd}, the droplets could rebound completely and the time sequences of droplet spreading, recoiling, and rebounding were almost the same. As T_s decreased to 268 K, water droplets with T_{wd} = 278 K and 283 K exhibited complete rebound, whereas the droplet with T_{wd} = 293 K exhibited partial rebound and broke-up into a bigger and a tiny part at 22.5ms (Figure 3.7b). When T_s was further decreased to 263 K (Figure 3.7c), water droplets with T_{wd} = 278 K and 283 K still exhibited complete rebounding from the SHS. However, for water droplet with T_{wd} = 283 K rebounding occurred at 17.75 ms, whereas for droplet with T_{wd} = 278 K rebounding occurred 15.5 ms. Also, the rebounding height of water droplet with T_{wd} = 283 K was much smaller compared to that at 278 K. At this surface temperature, a further increase in droplet temperature up to T_{wd} = 293 K made the droplet completely adhered to the SHS. With a further reduction of surface temperature to 258 K (Figure 3.7d), the droplet rebounding behavior became more pronounced with increasing T_{wd}. At this surface temperature, the droplet with T_{wd} = 278 K could rebound completely at 20 ms, while the droplet with T_{wd} = 283 K partially rebounded and broke-up at 26.25 ms, and the droplet with T_{wd} = 293 K completely adhered to the surface.

The variation in t_c and H_r for droplets with increasing temperature are shown in Figure 3.8 and Figure 3.9, respectively. From the figure it is obvious that at a significantly lower SHS temperatures (< 268 K), an increase in water droplet temperature resulted in prolonged droplet-SHS contact time and reduced rebounding height and eventually led to the loss of rebounding capability of the droplet.

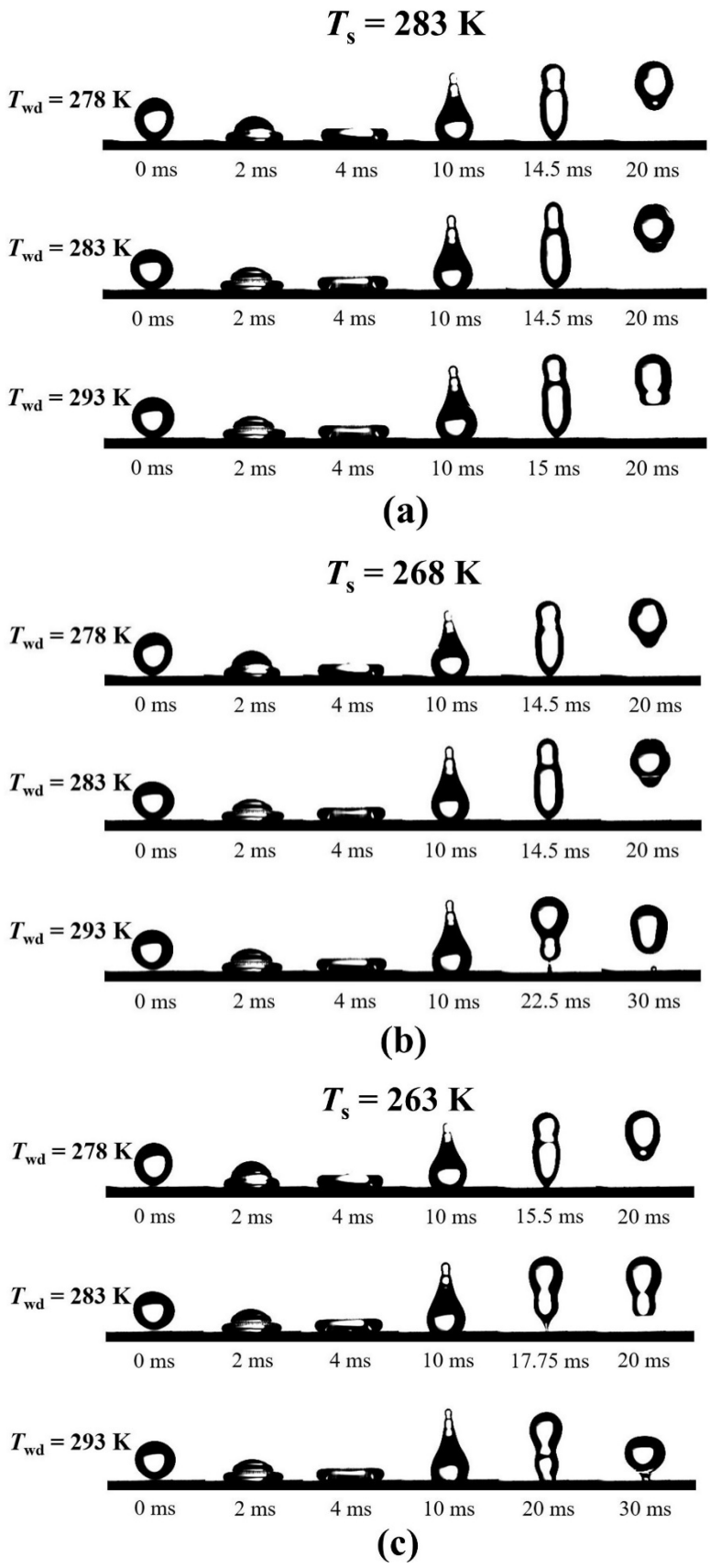
T_s = 283 K
T_{wd} = 278 K
0 ms 2 ms 4 ms 10 ms 14.5 ms 20 ms
T_{wd} = 283 K
0 ms 2 ms 4 ms 10 ms 14.5 ms 20 ms
T_{wd} = 293 K
0 ms 2 ms 4 ms 10 ms 15 ms 20 ms
(a)
T_s = 268 K
T_{wd} = 278 K
0 ms 2 ms 4 ms 10 ms 14.5 ms 20 ms
T_{wd} = 283 K
0 ms 2 ms 4 ms 10 ms 14.5 ms 20 ms
T_{wd} = 293 K
0 ms 2 ms 4 ms 10 ms 22.5 ms 30 ms
(b)
T_s = 263 K
T_{wd} = 278 K
0 ms 2 ms 4 ms 10 ms 15.5 ms 20 ms
T_{wd} = 283 K
0 ms 2 ms 4 ms 10 ms 17.75 ms 20 ms
T_{wd} = 293 K
0 ms 2 ms 4 ms 10 ms 20 ms 30 ms
(c)

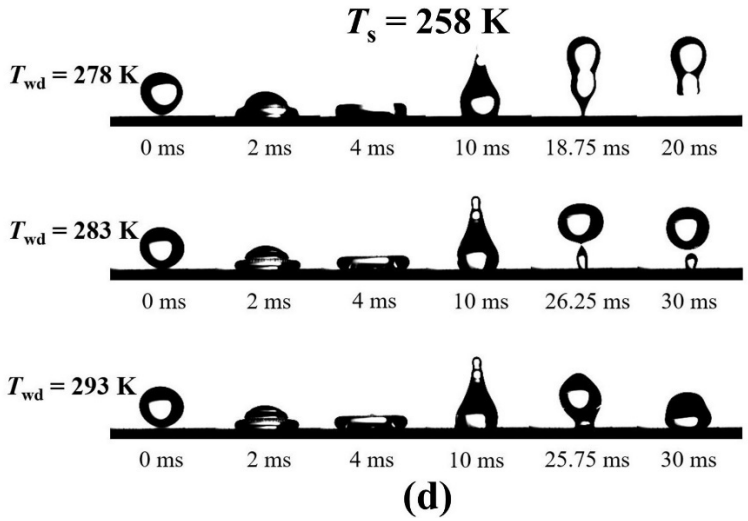

Figure 3.7 Side-view images depicting the impact behaviors of a water droplet with diameter D_M and temperature T_{wd} = 278, 283, and 293 K impinging on an SHS at a T_s of (a) 283 K, (b) 268 K, (c) 263 K, and (d) 258 K.

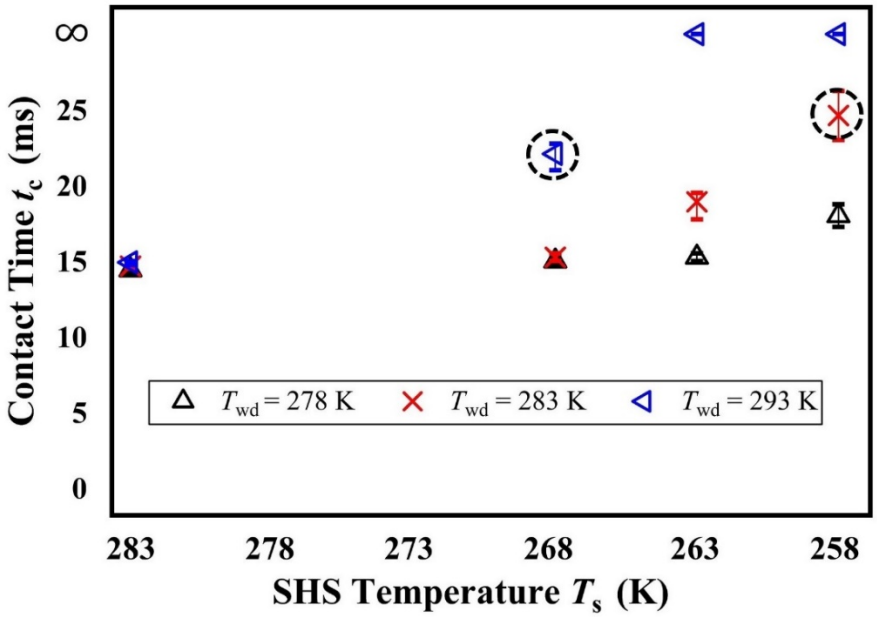

Figure 3.8 Contact time t_c of water droplets with diameter D_M and temperature T_{wd} = 278, 283, and 293 K impinging on an SHS at T_s = 283, 268, 263, and 258 K. Dashed circles represent the occurrence of droplet break-up. For each condition, the experiments were conducted three times at different positions on SHS.

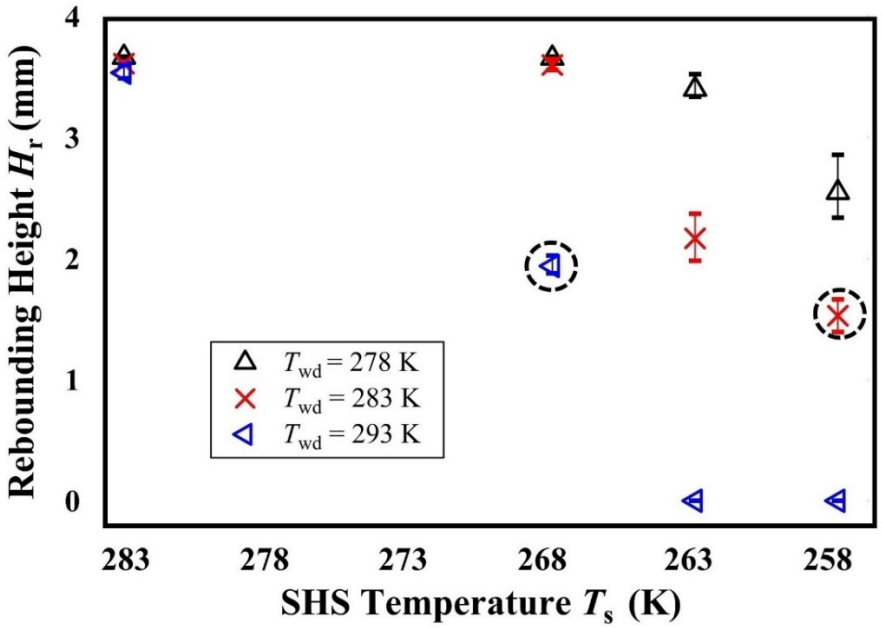

Figure 3.9 Rebounding height H_r of water droplets with diameter D_M and temperature T_{wd} = 278, 283, and 293 K impinging on an SHS at T_s = 283, 268, 263, and 258 K. Dashed circles represent the occurrence of droplet break-up. For each condition, the experiments were conducted three times at different positions on SHS.

3.3.3. Effect of water droplet size on droplet impact behaviors

The effect of increasing droplet size on impact behaviors was investigated by a water droplet with three different diameters D_S, D_M, and D_L under a constant droplet temperature T_{wd} = 283 K, while the temperature of SHS was varied between 283 K to 258 K, as shown in Figure 3.10. When T_s was maintained at 283 K and 268 K, the impinging water droplet exhibited completely rebound from the SHS for all three droplet sizes (Figure 3.10a and 3.10b respectively), although t_c and H_r became slightly longer and smaller respectively, with increasing droplet diameter. However, at T_s = 268 K, the droplet with diameter D_L took more time to lift off from the SHS and bounced lower. With a further decrease of T_s to 263 K and eventually to 258 K, the water droplet with a smaller diameter D_S could still complete rebound with a slight change in contact time and rebounding height (Figure 3.10c and 3.10d). The droplet with diameter D_M exhibited complete rebound with longer droplet-SHS contact time at T_s = 263 K and partial

rebound with break-up at T_s = 258 K. The droplet with diameter D_L exhibited partial rebound with break-up at T_s = 263 K and adhered to SHS at T_s = 258 K.

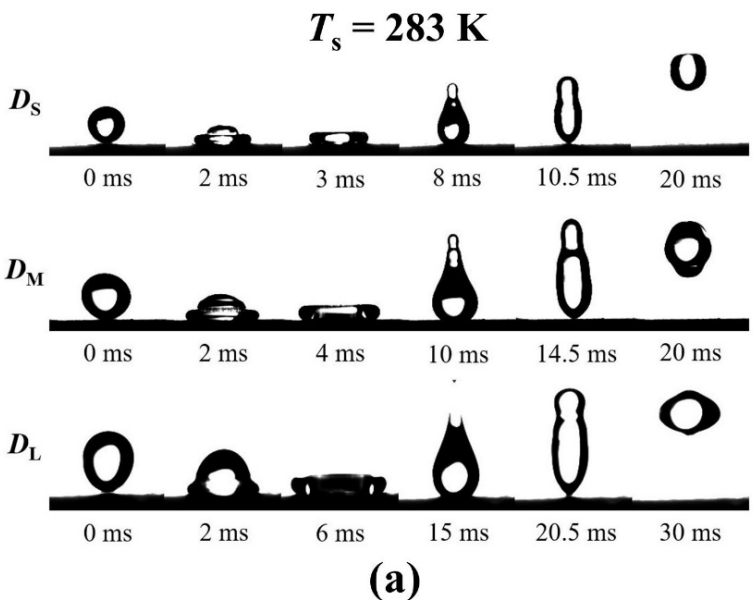

(a)

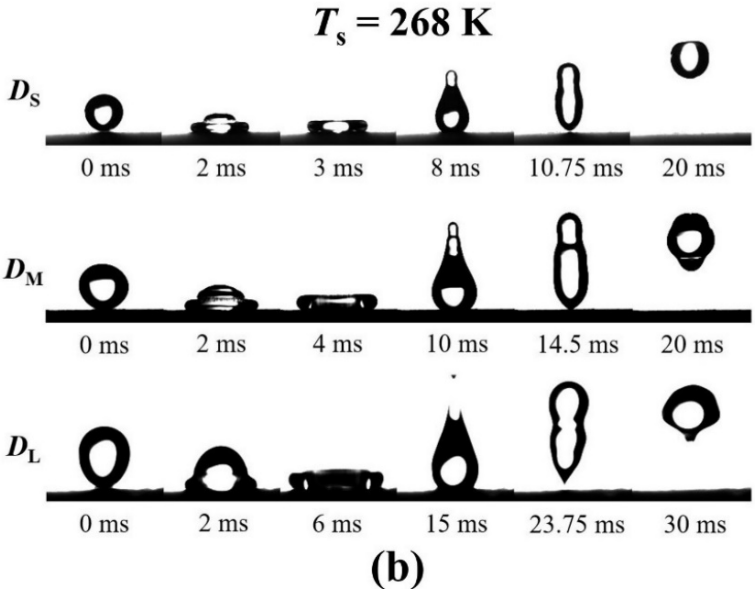

(b)

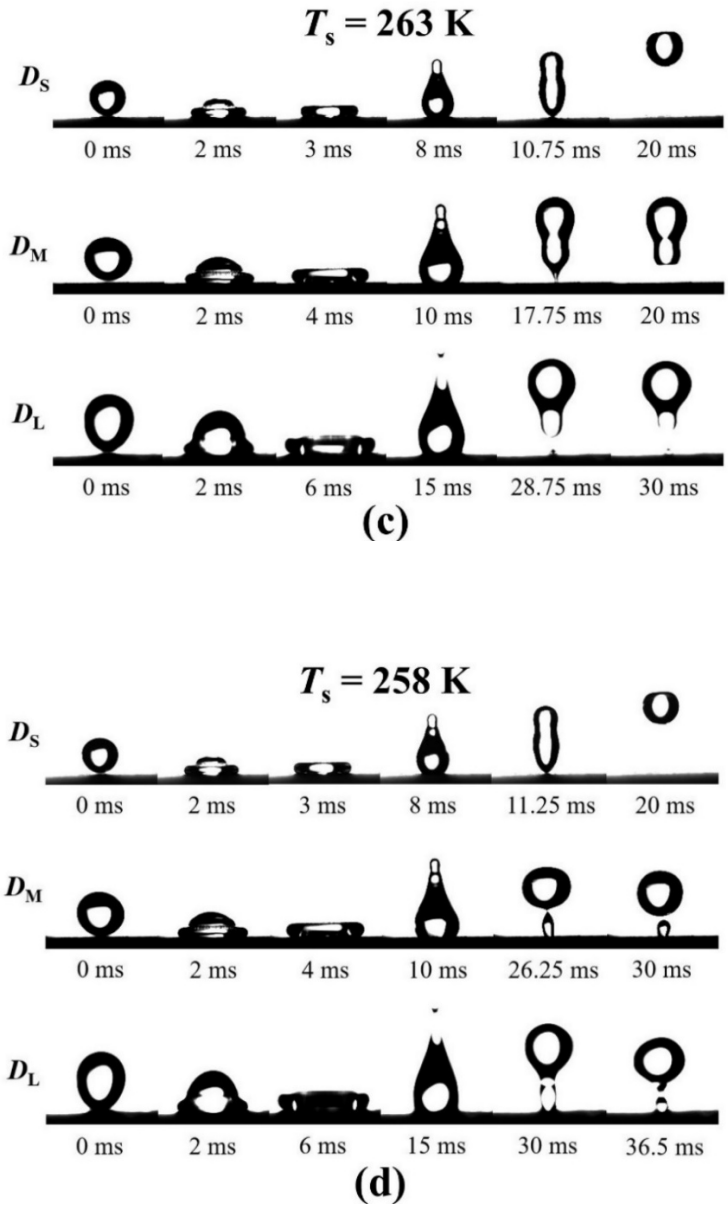

Figure 3.10 Side-view images depicting the impact behaviors of water droplets with diameters D_S, D_M, and D_L and temperature T_{wd} = 283 K impinging on an SHS at T_s of (a) 283 K, (b) 268 K, (c) 263 K, and (d) 258 K.

The variation of droplet-SHS contact time (t_c) and rebounding height (H_r) under above conditions are summarized in Figure 3.11 and Figure 3.12, respectively. From the results, it is evident that decreasing the surface temperature from 283 K to 258 K has little influence on the rebound dynamics of the droplet with diameter D_S, but large influence on the bouncing capacity of larger droplets with diameter D_M or D_L.

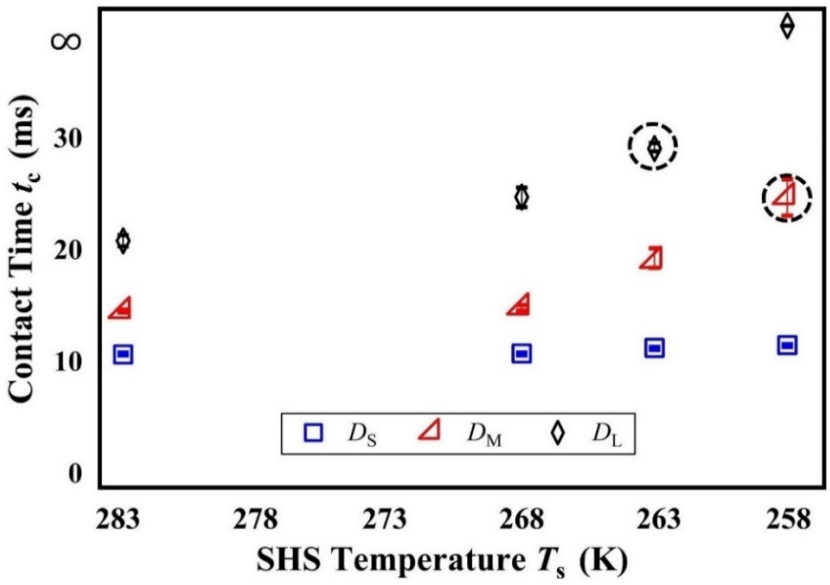

Figure 3.11 Contact time t_c of water droplets with diameters D_S, D_M and D_L and temperature T_{wd} = 283 K impinging on an SHS at T_s = 283, 268, 263, and 258 K. Dashed circles represent the occurrence of droplet break-up. For each condition, the experiments were conducted three times at different positions on SHS.

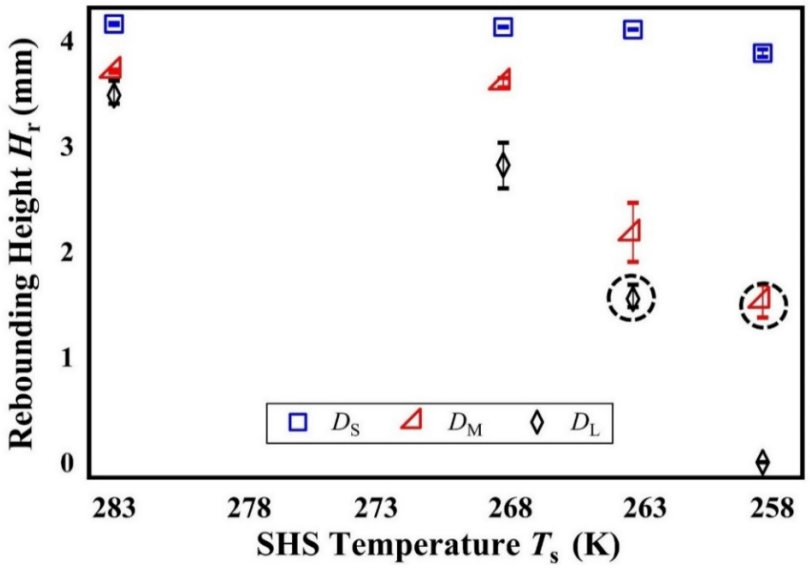

Figure 3.12 Rebounding height H_r of water droplets with diameters D_S, D_M and D_L and temperature T_{wd} = 283 K impinging on an SHS at T_s = 283, 268, 263, and 258 K. Dashed circles represent the occurrence of droplet break-up. For each condition, the experiments were conducted three times at different positions on SHS.

3.3.4. Comparison between contact time and characteristic contact time

This chapter compares the contact time (t_c) and characteristic contact time (τ) [66] of droplets with three different diameters D_S, D_M and D_L on SHS. When droplet size changed under isothermal condition, the ratio of contact time over characteristic contact time should be constant. The characteristic contact time of an impinging water droplet on SHS can be evaluated by balancing inertia with capillarity [66], which yields,

$$\frac{\rho_w R}{\tau^2} = \frac{\gamma}{R^2} \tag{3.1}$$

$$\tau = \sqrt{\frac{\rho_w R^3}{\gamma}} \tag{3.2}$$

where ρ_w denotes the density of water, τ is the characteristic contact time, and γ is the surface tension of water [132].

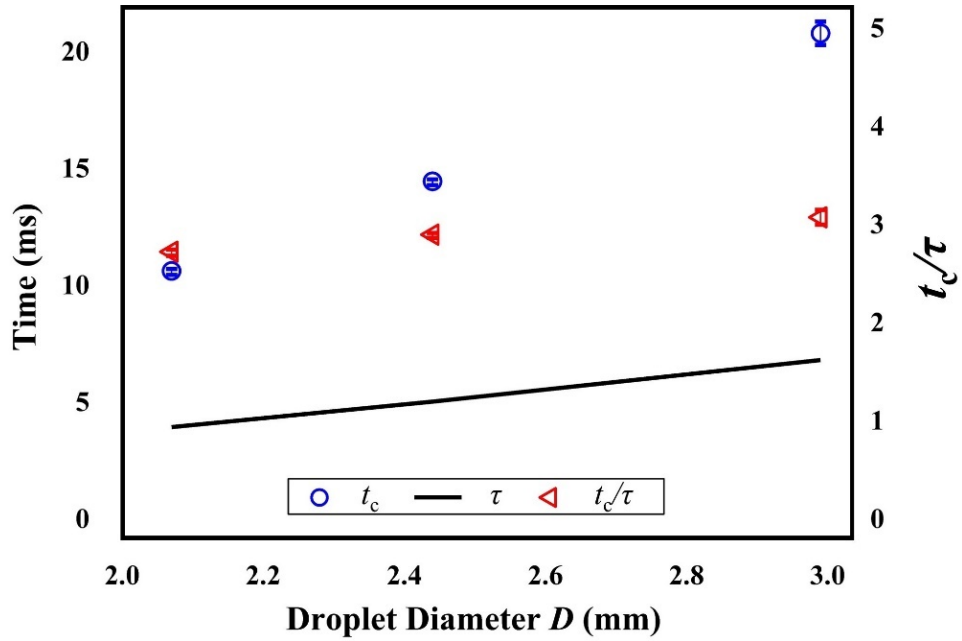

Figure 3.13 Contact time t_c, characteristic contact time τ, and the ratio t_c/τ of a water droplet with different diameter impacting on SHS when T_s and T_{wd} are the same at 283 K.

Figure 3.13 compares the droplet-SHS contact time, characteristic contact time, and the ratio of contact time over characteristic contact time under isothermal conditions (T_s and T_{wd} are the same at 283 K). With the increase in droplet diameter, both contact time and characteristic contact time exhibited a tendency to increase steadily, but t_c/τ showed a negligible relationship with the droplet diameter. The contact time t_c measured in our experiments was in good agreement with the theoretical prediction of droplet-SHS contact time τ. Figure 3.13 validated that our current experimental results were reliable.

3.4. Discussions

This chapter analyzes the dominant mechanism affecting droplet rebounding or sticking mechanism of an impinging water droplet on SHS near freezing temperatures illustrated in Chapter 3.3. Chapter 3.4.1 summarizes the proposed mechanism then theoretical models are employed for verification as shown in Chapter 3.4.2.

3.4.1. Droplet rebounding or sticking mechanism on the cold SHS

To understand the underlying mechanism of experimental observations as described in Chapter 3.3, a comprehensive summary of the effects of SHS temperature T_s and water droplet temperature T_{wd} on rebounding behavior of water droplet with diameter D_M is shown in Figure 3.14. From the figure it is evident that the droplet rebounds to a lower height, partially rebounds with break-up, and eventually becomes adhered to SHS as the temperature of SHS is decreased or temperature of droplet is increased. During experiment, the rebounding capability of the droplet was lost not due to ice nucleation inside the droplet, since the solidification of droplet would result in loss of transparency [50,74–77] and stop the contact line movement [74,78] which was not observed in Figures 3.5, 3.7, and 3.10 (as presented in Chapter 3.3). In addition, as T_{wd} increased, the impinging droplet started to lose its rebounding capability although the viscosity of droplet reduced due to higher droplet temperature. Therefore, it can be inferred that ice nucleation within the droplet was not the appropriate means for the loss of rebounding capability of droplets in this work. Besides, the SHS is made of hierarchical surface

structures, instead of closed structures, therefore, the pressure between droplet and SHS was not considered as a dominant factor.

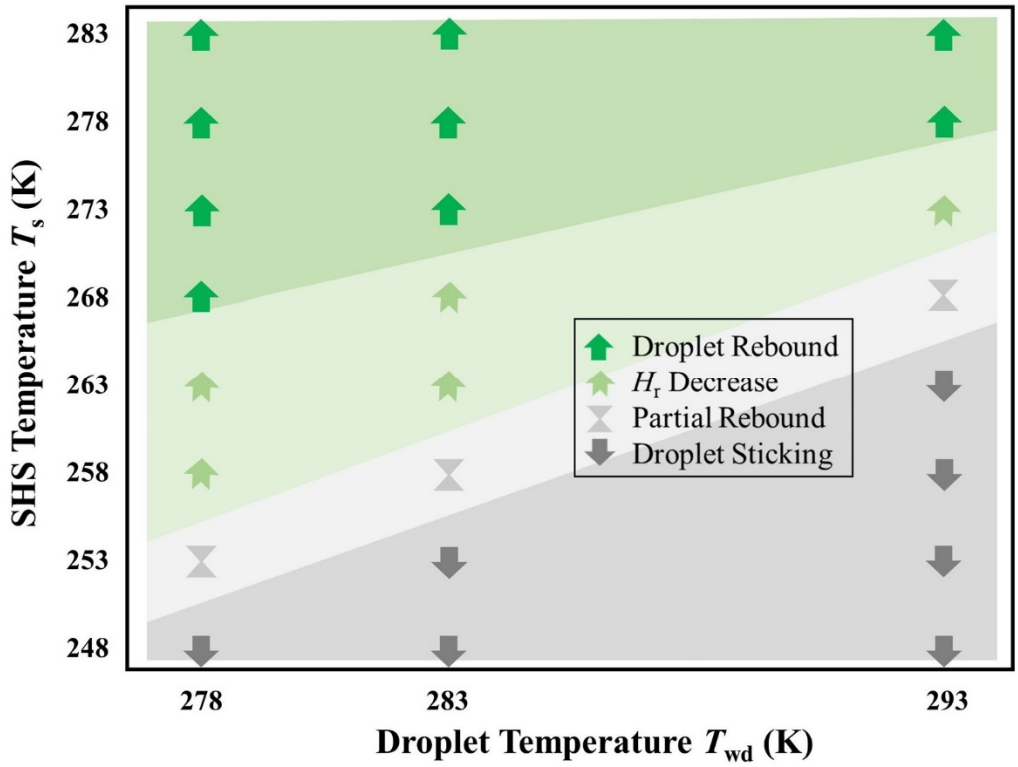

Figure 3.14 Rebound, H_r decrease, break-up, and adherence performance of a water droplet with diameter D_M and temperature T_{wd} impinging on an SHS at temperature T_s.

In the work of Mouterde et al. [88] it was reported that when a hot water droplet came into contact with SHS, condensate from the droplet accumulated within the surface cavities of SHS and led to formation of water bridges. Here, we also elucidate our experimental outcomes by a similar mechanism that when a water droplet impacted on a cold SHS, evaporation took place from the droplet and the evaporated water vapors condensed within the micro/nano surface cavities of SHS and possibly formed bridges of water. This could give rise to the adhesion between the water droplet and small water bridges within micro/nano surface cavities of SHS, and as a result the rebounding capacity of the droplet was affected and phenomena like partial rebound with break-up or even no rebound were observed.

During droplet impact, depending on the dimensions of SHS textures, there could be some distributions of Wenzel and Cassie states on the SHS, which determined its overall hydrophobicity. Taking the SHS structure with an average surface roughness as an example, a schematic illustration of the aforesaid mechanism depicting evaporation and accumulation of water due to condensation inside micro/nano surface cavities is presented in Figure 3.15. However, providing direct evidence by taking real time images of formed water bridges was not feasible in the present work due to the limitation of experimental facility and very tiny surface cavities of fabricated SHS.

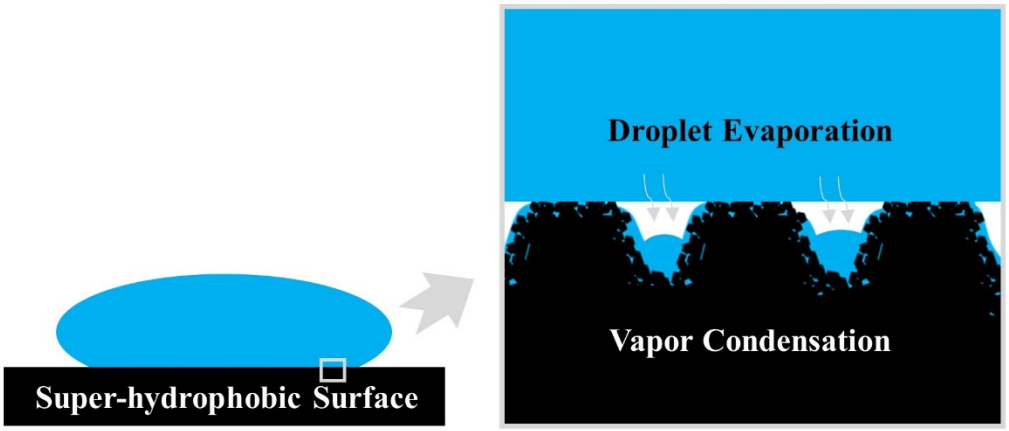

Figure 3.15 Schematic diagram showing the evaporation of an impinging water droplet, and the further condensation of the vapor inside micro/nano hierarchical structures of cold SHS.

3.4.2. Theoretical analysis of evaporation during droplet impact

For the evaporation of impinging droplet, the characteristic evaporation time t_e (i.e., the time required to saturate air within the micro/nano surface cavities of SHS) can be estimated as follows [89],

$$t_e \sim h^2/\mathcal{D} \tag{3.3}$$

where h denotes the height of micro/nano hierarchical surface structures, and $\mathcal{D}$ is the diffusion coefficient of water.

Taking h as 5.92 μm based on AFM analysis and $\mathcal{D}$ as 2×10^{-5} m^2 s^{-1} [89,133], and t_e was obtained as 1.75 μs which is almost three order of magnitude smaller than the droplet-SHS contact time (t_c). Therefore, water vapor from the droplet should have sufficient time to penetrate and fill the micro/nano hierarchical surface structures during the millisecond impact between droplet and SHS. In the work of Shiri et al. [89], the air inside SHS microstructure was considered as saturated during the millisecond (nearly 10 ms) impact between droplet and SHS as well.

To corroborate the proposed mechanism stated in previous section, a 1D analytical model [89] was employed to approximately estimate the thickness of condensed water layer inside micro/nano surface cavities of SHS under different temperature conditions. The influence of SHS temperature, water droplet temperature and droplet size were also assessed on the growth of condensed water layer. However, it is to be noted that experimental validation of the model could not be done here due to the same challenge of imaging and quantifying amount of condensed water inside very tiny surface cavities of SHS. Details of the model are described in Chapter 3.4.3.

3.4.3. Vapor-liquid phase transport model

To estimate the condensation growth rate inside the cavities of cold SHS, a 1D vapor-liquid phase transport model [89,134–136] was employed. Since in the present work time scale of droplet-SHS contact duration was in milliseconds, the following two assumptions could be valid under this short time scale: (i) the temperature of water vapor generated from the droplet was constant with time and in equilibrium to the temperature of the droplet T_{wd} and (ii) the temperature of condensed water was also constant with time and in equilibrium to SHS temperature T_s. The heat flux between vapor and liquid phases was entirely converted into latent heat required for condensation. The latent heat for condensation was estimated by the enthalpy change in condensed water. Therefore, the heat flux q between the vapor and liquid phases [136] can be expressed as,

$$q = h_i \Delta T \approx h_i (T_{wd} - T_s) \tag{3.4}$$

$$q = L\rho_w \frac{dr}{dt} \tag{3.5}$$

where h_{i} is the interfacial heat transfer coefficient, L is the latent heat of condensation, ρ_{w} denotes the density of liquid water, and dr/dt is the condensation rate. The condensed water temperature was assumed to be constant, yielding a constant interfacial heat transfer coefficient h_{i}. The fluxes of vapor and liquid water molecules were assumed to be characterized by the temperature and pressure of these two phases. Based on the Maxwell velocity distribution [56], the interfacial heat transfer coefficient h_{i} can be modeled as [134–136],

$$h_{\mathrm{i}} = \frac{2\hat{\sigma}}{2-\hat{\sigma}}\left(\frac{\rho_{\mathrm{wv}}L^2}{T_{\mathrm{wd}}}\right)\left(\frac{\bar{M}}{2\pi\bar{R}T_{\mathrm{wd}}}\right)^{1/2} \tag{3.6}$$

where $\hat{\sigma}$ is the condensation accommodation coefficient, ρ_{wv} denotes the saturated water vapor density, $\bar{M}$ is the molecular weight, and $\bar{R}$ is the gas constant. Derivation of the interfacial heat transfer coefficient h_{i} can be found in Appendix D.

Then, the condensation rate can be expressed as,

$$\frac{dr}{dt} \approx \frac{h_{\mathrm{i}}(T_{\mathrm{wd}}-T_{\mathrm{s}})}{L\rho_{\mathrm{w}}} = \frac{2\hat{\sigma}}{2-\hat{\sigma}}\frac{\rho_{\mathrm{wv}}}{\rho_{\mathrm{w}}}\frac{T_{\mathrm{wd}}-T_{\mathrm{s}}}{T_{\mathrm{wd}}}\frac{L}{\sqrt{2\pi(\bar{R}/\bar{M})T_{\mathrm{wd}}}} \tag{3.7}$$

Figure 3.16 displays the schematic diagram the simplified 1D condensation model considered in the vapor-liquid phase transport model based on the real experimental system as shown in Figure 3.15.

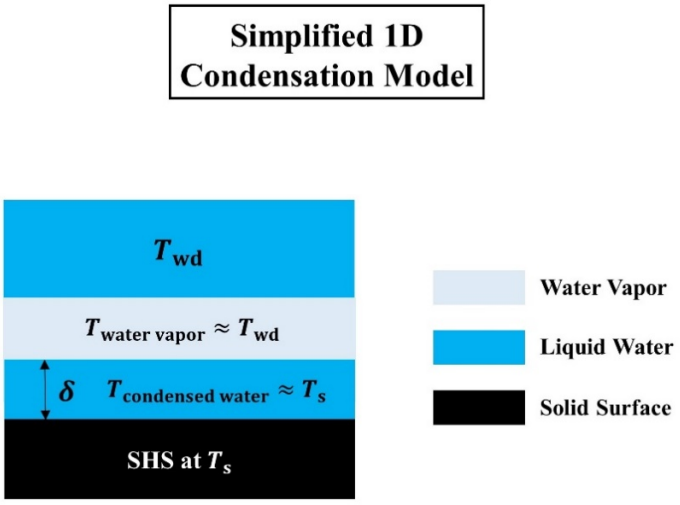

Figure 3.16 Schematic diagram of the real experimental system and the simplified 1D condensation model calculating the thickness of condensed water δ inside cavities of cold SHS.

Based on the condensation rate, the thickness of condensed water δ inside hierarchical textures of SHS during contact time of droplet-SHS can be evaluated as,

$$\delta = \frac{dr}{dt} \cdot t_{\mathrm{c}} \tag{3.8}$$

The condensation accommodation coefficient $\hat{\sigma}$ was obtained by fitting the thickness of condensed water δ with the average height of SHS structure. During experiments, it was observed that under the following two experimental conditions partial rebound with droplet break-up occurred: (i) when T_{s} and T_{wd} were 263 K and 283 K, respectively for droplet with diameter D_{L} (Figure 3.10c) and (ii) when T_{s} and T_{wd} were 258 K and 283 K, respectively for droplet with diameter D_{M} (Figure 3.10d). We assumed that in above two cases, condensed water fully occupied the micro/nano textures of SHS. Then, the fitting condensation accommodation coefficient $\hat{\sigma}$ can be calculated as 0.151 ± 0.004. This value of $\hat{\sigma}$ is consistent with those values (ranging from 0.1 to 1) reported in other studies [137,138]. Table 3.4 presents all the relevant parameters used in this study.

Table 3.4 Parameters used to calculate the condensation rate of an impinging water droplet on super-hydrophobic surface.

Condensation accommodation coefficient, $\hat{\sigma}$	0.151	Density of liquid water, ρ_{w}	998.2 kg m^{-3}
Latent heat of condensation, L	2257 kJ kg^{-1}	Saturated water vapor density [139], ρ_{wv} (at 278 K)	4.91 kg m^{-3}
Molecular weight, $\bar{M}$	18.02 g mol^{-1}	Saturated water vapor density, ρ_{wv} (at 283 K)	6.88 kg m^{-3}
Gas constant, $\bar{R}$	8.3145 J mol^{-1} K^{-1}	Saturated water vapor density, ρ_{wv} (at 293 K)	17.50 kg m^{-3}

3.4.4. Theoretical analysis of the amount of condensed water

Figure 3.17 shows the condensation growth rate of water vapor from the droplet estimated by Equation 3.7 at T_{wd} on SHS at T_s. With a decrease in T_s, vapor condensation rate tended to increase. For instance, when the water droplet temperature was 278 K, condensation initiated as T_s reached less than 278 K. When T_s was reduced from 278 K to 248 K, the condensation rate increased. Moreover, an increase in water droplet temperature also induced water vapor condensation. When droplet temperature was 293 K, the condensation rate increased by approximately five times compared with that at 278 K. With the increasing condensation rate, the amount of condensed water increased correspondingly during droplet-SHS contact.

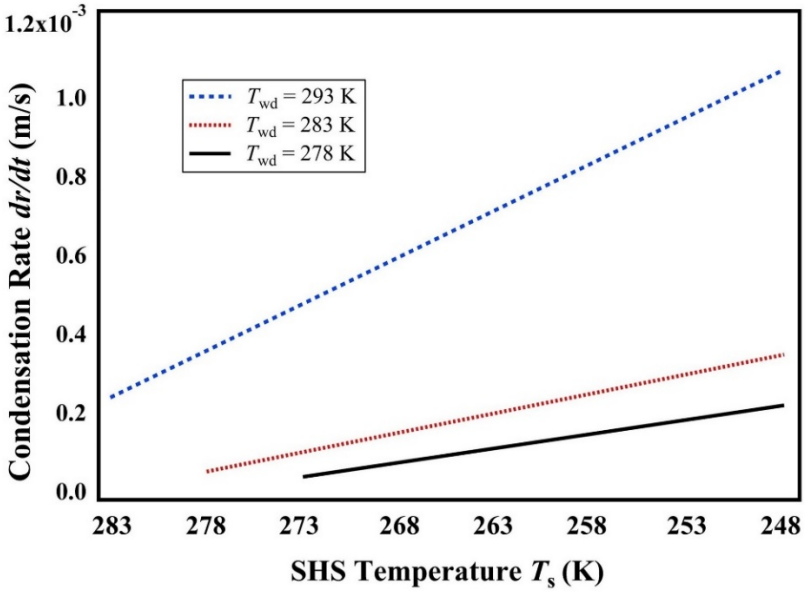

Figure 3.17 Condensation growth rate dr/dt of water vapors emerging from impinging water droplet at temperature T_{wd} on SHS at T_s.

Figure 3.18 shows the thickness of condensed water on SHS derived by Equation 3.8 under different temperature conditions. As T_s decreased or T_{wd} increased, the amount of condensed water inside hierarchical surface textures increased during droplet-SHS contact. At T_{wd} = 293 K, when T_s equaled to 263 K and 258 K, the calculated

condensation water thickness surpassed the average SHS textures (5.92 μm) greatly, indicating that the surface was likely to be entirely filled with water. These results were consistent with droplet rebounding behaviors in Figure 3.9 that at these conditions the water droplet did not rebound. Furthermore, when the temperature was constant, for droplets with larger diameters D_M or D_L, the amount of condensed water increased compared with the case of the droplet with a smaller diameter D_S, owing to the prolongment of droplet-SHS contact time (Figure 3.19). The condensed water bridged the impinging water droplet and SHS. After adequately solid droplet-SHS water bridges were formed, the impinging water droplet exhibited a slow rebound.

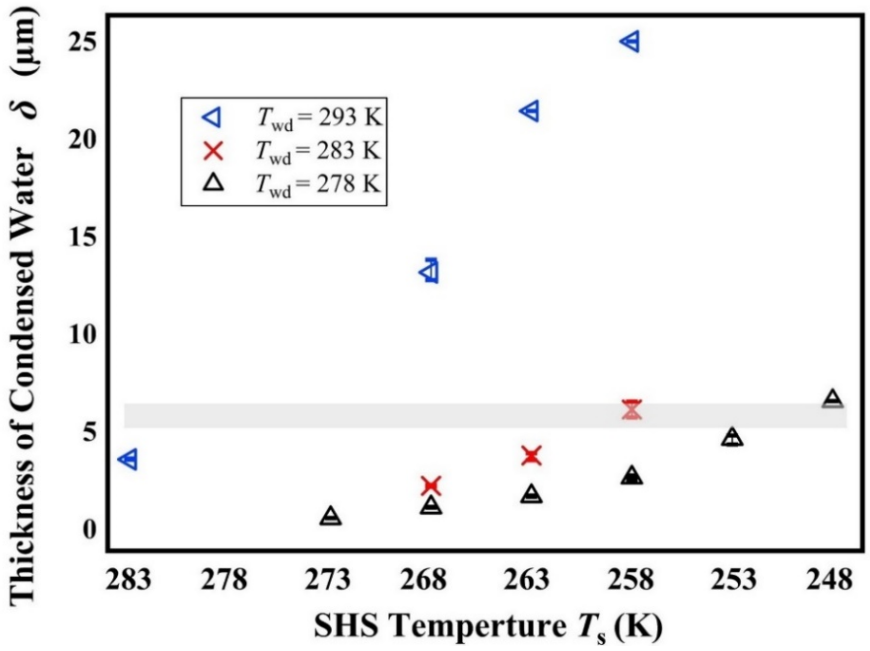

Figure 3.18 Thickness of condensed water δ on SHS during droplet-SHS contact time when droplet with diameter D_M at T_{wd} impinging on SHS at T_s. 30 ms was selected as the contact time when the droplet adhered.

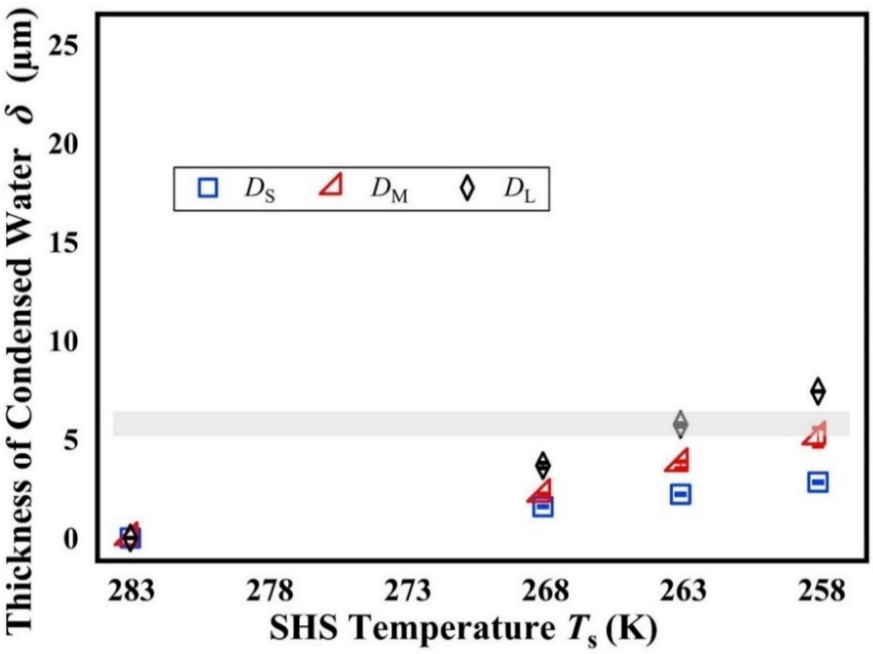

Figure 3.19 Thickness of condensed water δ on SHS during droplet-SHS contact time when droplet with diameter D_S, D_M, and D_L. 30 ms was selected as the contact time when the droplet adhered.

3.5. Summary

This chapter experimentally demonstrated the rebounding behavior of an impinging water droplet on an SHS near the freezing point and evaluated the effects of SHS temperature, water droplet temperature, and droplet size on its impact dynamics. With the decrease of SHS temperature, the impact droplet tended to become adhered to the SHS with an increase in contact time and a decrease in rebounding height. When water droplet temperature increased, the droplet showed the tendency to stick to the cold SHS. For larger impact droplet, the tendency of adhering to cold SHS became more prominent.

Theoretically, water vapor evaporation from an impinging water droplet and the subsequent vapor condensation on cold SHS were evaluated when droplet was in contact with SHS. The impacting process occurred within milliseconds. However, in a low-humidity environment, the vapor emerging from the impinging water droplet saturated the localized air inside micro/nano hierarchical textures of SHS. In addition, water vapor

condensation might occur when in contact with surface at lower temperatures. When condensed water accumulated inside SHS hierarchical micro/nano textures, water bridges between droplet and SHS could be formed. The formed water bridges would increase the droplet-SHS adhesion. As surface temperature decreased from 283 K to 248 K or droplet temperature increased from 278 K to 293 K, the condensation rate of emerging water vapor increased. Over time, the impinging water droplet became incapable of rebounding from SHS. Furthermore, droplet size growth caused the prolongment of contact time and increased the accumulation of condensed water on SHS. Therefore, impinging droplets with larger diameters exhibited a more apparent trend of adhering to cold SHS.

The condensed water would also cause the wetting transition of SHS from the Cassie-Baxter state to Wenzel state. Therefore, Chapter 4 will analyze the wetting transition caused by the water condensation during droplet impact, accordingly the energy loss analysis during droplet impact process is evaluated.

Chapter 4 Experimental Study on Condensation-Initiated Wetting Transition of an Impact Water Droplet on an SHS and the Energy Loss Analysis

4.1. Introduction

For SHS, preservation of surface super-hydrophobicity is crucial to effectively repel incoming water droplets. An impinging water droplet loses rebounding capability if the super-hydrophobicity of surface is destroyed. Antonini et al. [140] experimentally observed that a millimeter-sized water droplet only rebounds from surfaces with a receding contact angle larger than 100° for a wide range of impact velocities. Furthermore, Antonini et al. [141] mathematically found a negative correlation between droplet-surface adhesion force and receding contact angle of SHS. Shen et al. [142] reported that the increase in surface contact angle hysteresis prolongs the contact time of an impinging water droplet with an SHS, because SHS with a higher contact angle hysteresis generates a larger resistance force and requires more kinetic energy owing to droplet-SHS adhesion. Xiu et al. [143] proposed a theoretical positive relationship between the droplet-surface work of adhesion and the difference in advancing contact angle and receding contact angle by employing the Young-Dupré equation.

Wetting transition from the Cassie-Baxter state [79] to Wenzel state [80] has been observed in literatures. For instance, the receding contact angle of a sessile water droplet on an SHS reduces greatly when the surface temperature is decreased to below 273 K [81,82]. Because wetting transition happens when condensed water accumulates within SHS micro/nano structures and the adherence between droplet and cold SHS is enhanced greatly. When a water droplet impacts on an SHS the droplet rebounding behaviors are affected due to the formation of condensation nucleus inside SHS textures [88,89], despite the short contact time period between droplet and SHS. In addition, impact water droplet [90–92] can cause the wetting transition on an SHS if the droplet collides with a

high velocity and penetrates the surface micro/nano textures. However, the influence of an impinging water droplet on the super-hydrophobicity of an SHS near freezing temperatures is yet to be explored in detail.

This research investigates the occurrence of wetting transition of an SHS near freezing temperatures from the Cassie-Baxter state to Wenzel state induced by the condensation of evaporated vapor from incoming water droplet inside surface hierarchical micro/nano textures, although droplet-surface contact merely lasts several milliseconds. Contact angles during the droplet receding process are measured and compared under various experimental conditions. For an impact droplet with the diameter of 2.44 mm and Weber number ~10, in receding process the average contact angle decreases tremendously as the surface temperature reduces from 283 K to 248 K. Nevertheless, the receding contact angle of sessile water droplet on cold SHS demonstrates its weak dependency on surface temperature (from 268 K to 258 K) owing to the sufficient time for vapor condensation. For an impact water droplet on an SHS near freezing temperatures, this wetting transition regime leads to the increase of kinetic energy loss due to droplet-SHS adhesion, correspondingly the droplet rebound dynamics is altered. Hence, a detailed elucidation of the energy analysis during rebounding process is presented in Chapter 4.4. Understanding the wetting transition of superhydrophobic surfaces near freezing temperatures caused by incoming water droplets is of primary significance to the design of superhydrophobic surfaces in the fields of anti-icing.

4.2. Experimental section

This chapter introduces the experiments of wetting transitions of an SHS near freezing temperatures induced by an impact water droplet in Chapter 4.2.1 and a sessile water droplet in Chapter 4.2.2.

4.2.1. Experiments of wetting transition of SHS near freezing temperatures induced by an impact water droplet

The experimental setup utilized to investigate the droplet impact behaviors on SHS near freezing temperatures was displayed in Figure 3.4 and explained in Chapter 3.2.4.

Chapter 3.2.4 introduced the procedures to carry out the experiments as well. Chapter 3.3 showed the experimental results and Chapter 3.4 presented the proposed physics that the condensed water within SHS micro/nano structures might form droplet-SHS water bridges and increase the droplet-SHS adhesion. The condensed water led to the wetting transition from the Cassie-Baxter state to Wenzel state. To illustrate this wetting transition induced by an impact water droplet on an SHS near the freezing temperatures, this study measured the average contact angle of water droplet during its recoiling process $\overline{\theta_c}$ under different experimental conditions.

The average contact angle of a water droplet during receding on an SHS $\overline{\theta_c}$ is measured as follows: the contact angle between a water droplet and an SHS was measured every 1 millisecond from the moment of droplet recoiling (3, 4, and 6 ms for D_S, D_M and D_L, respectively) to the moment of droplet rebound. When a water droplet adhered to an SHS, $\overline{\theta_c}$ was the average value from 4 to 20 ms for droplet with diameter D_M, and from 6 to 30 ms for droplet with diameter D_L. The experiment was performed three times using three different positions of SHS, and the average contact angle in each experiment was calculated. Figure 4.1a shows typical images depicting the impact behaviors of water droplets with D_M and T_{wd} = 278 K impinging on an SHS at T_s = 278 K in three repeated experiments. The blue line represents the manually fitting tangent aligned to the droplet at the triplet-phase contact point [69]. Figure 4.1b shows the mean value of the instantaneous contact angles on both sides of the droplet measured at every 1 millisecond from 4 to 14 ms. The average contact angle $\overline{\theta_c}$ is the mean of time-averaged values for three experiments. In Figure 4.1, the time-averaged values for three experiments are 146.29°, 146.37°, and 146.39°, respectively, and the average contact angle $\overline{\theta_c}$ is 146.35°.

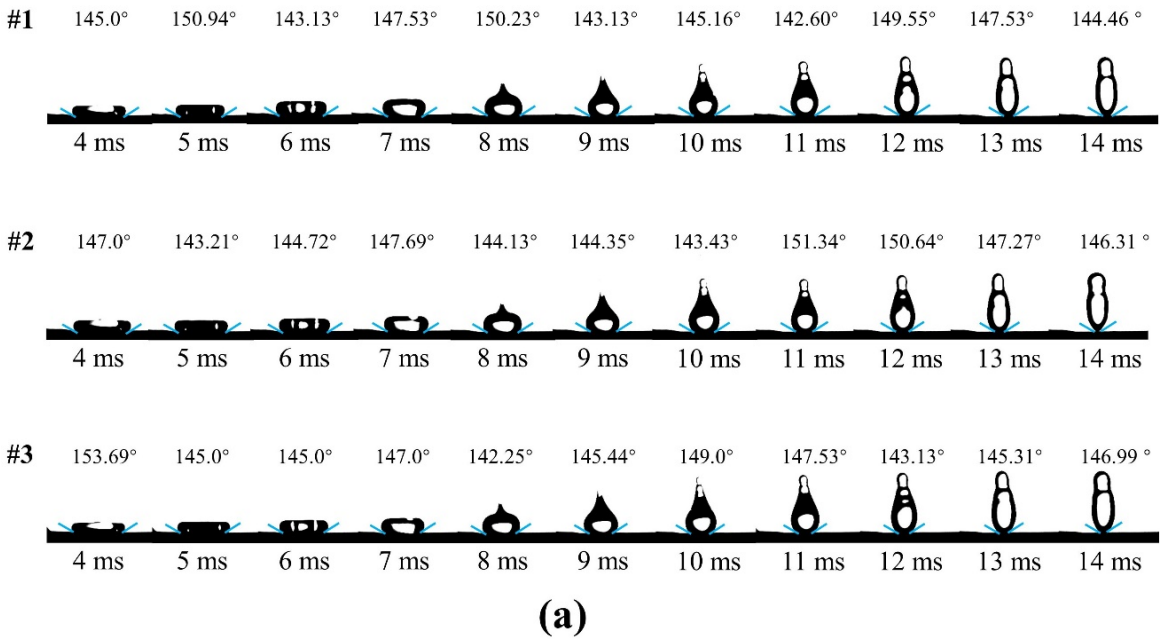

(a)

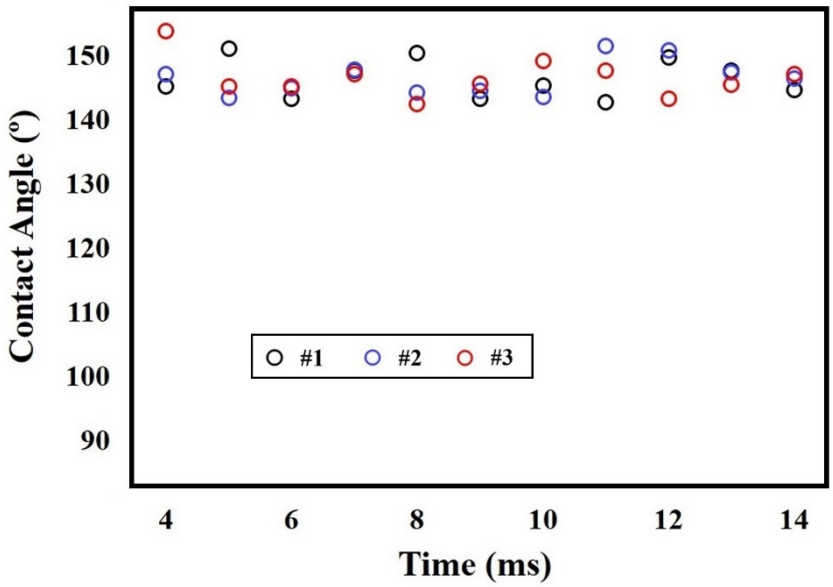

(b)

Figure 4.1 (a) Side-view images depicting the impact behaviors of water droplets with diameters D_M and temperature T_{wd} = 278 K impinging on an SHS at T_s = 278 K of three repeat experiments and (b) the instantaneous contact angle vs. time curve from the moment of droplet recoiling to the moment of droplet separation (4–14 ms). The blue line refers to the manually fitting tangent to droplet at the triple-phase contact point.

4.2.2. Experiments of wetting transition of an SHS near freezing temperatures induced by a sessile water droplet

The experimental setup to measure the contact angles of a sessile water droplet on an SHS is illustrated in Figure 4.2. Experiments were conducted in the chamber (PL-3J, Espec) with a dry gas supply system, inside which the ambient temperature was controlled at 278 ± 0.2 K and the relative humidity was controlled within the range 2–5 %. A humidity sensor (Hygrolog-HL-NT3, Rotronic Instruments) was employed to simultaneously measure the ambient temperature and relative humidity. The water droplet temperature was in equilibrium with the ambient temperature inside the chamber. Thus, by altering the ambient temperature inside the chamber, droplet temperature could also be altered. The SHS was placed on a Peltier cooling stage (VTH3500, VICS), which could precisely control the temperature of SHS within the range 283–258 ± 0.2 K. The K-type thermocouple was attached to SHS to measure T_s. The thermocouple on the SHS was attached at a location far enough from the sessile water droplet. Cold light was employed as the backlight for the sessile water droplet on SHS.

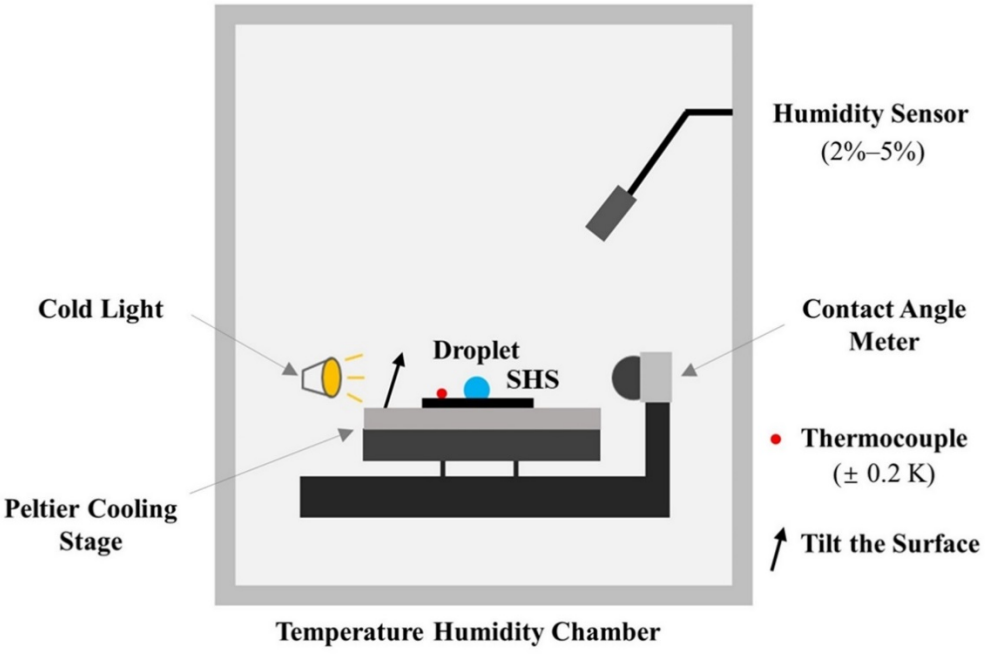

Figure 4.2 Schematic diagram of the experimental setup to measure the contact angles of a sessile water droplet on an SHS at different temperatures.

During experiments, SHS temperature T_s was varied from 283 K to 258 K and the initial droplet temperature T_{wd} was fixed at 278 K. The low ambient relative humidity condition (2–5 %) was chosen to avoid the condensation of water vapor on SHS from the ambient. T_s was initially set to a value of 10 K higher than the ambient temperature to prevent the deterioration of surface super-hydrophobicity caused by ambient vapor. Once the ambient relative humidity was stabilized within 2–5 %, T_s was tuned to the desired value. Then a deionized water droplet was generated gently on SHS via a home-made droplet generator. Immediately after generating the sessile droplet on SHS, static contact angle was measured. Then via the tilting cradle method, advancing contact angle, receding contact angle, and tilt angle were measured. For T_s = 283 K and 278 K, the surface was tilted at a speed of 0.1 ° s^{-1}. When T_s was below 268 K, the tilting speed was 0.5 ° s^{-1} to prevent droplet freezing. The experiment for each condition was repeated three times on random locations of SHS to ensure repeatability of data. All the relevant experimental parameters along with their measurement uncertainties are summarized in Table 4.1.

Table 4.1 Summary of the parameters involved in the experiments of measuring contact angles of a sessile water droplet on a super-hydrophobic surface.

Droplet volume, V	V_M = 7.63 ± 0.07 μL
Droplet diameter, D	D_M = 2.44 ± 0.01 mm
Droplet temperature, T_{wd}	278 ± 0.2 K
SHS temperature, T_s	283, 278, 268, 263, 258 ± 0.2 K
Relative humidity, RH	2–5 %

Figure 4.3 displays the schematic diagram of tilting cradle method adopted in this study. During each measurement, a droplet is deposited gently on SHS and θ_s is

measured, as shown in Figure 4.3a. Then the Peltier cooling stage is tilted until the triple-phase contact line moves, as shown in Figure 4.3b. At moment before contact line movement, θ_a and θ_r in Figure 4.3b are extracted from the images of the front and back of droplet, respectively. α is the angle of tilted surface at which contact line movement occurs. The lowest SHS temperature is selected as 258 K in this work because the droplet starts to freeze during the measurement when SHS temperature is further reduced to 253 K. In Figure 4.3 the real-time images of a sessile droplet on SHS at T_s = 268 K during measurement are shown.

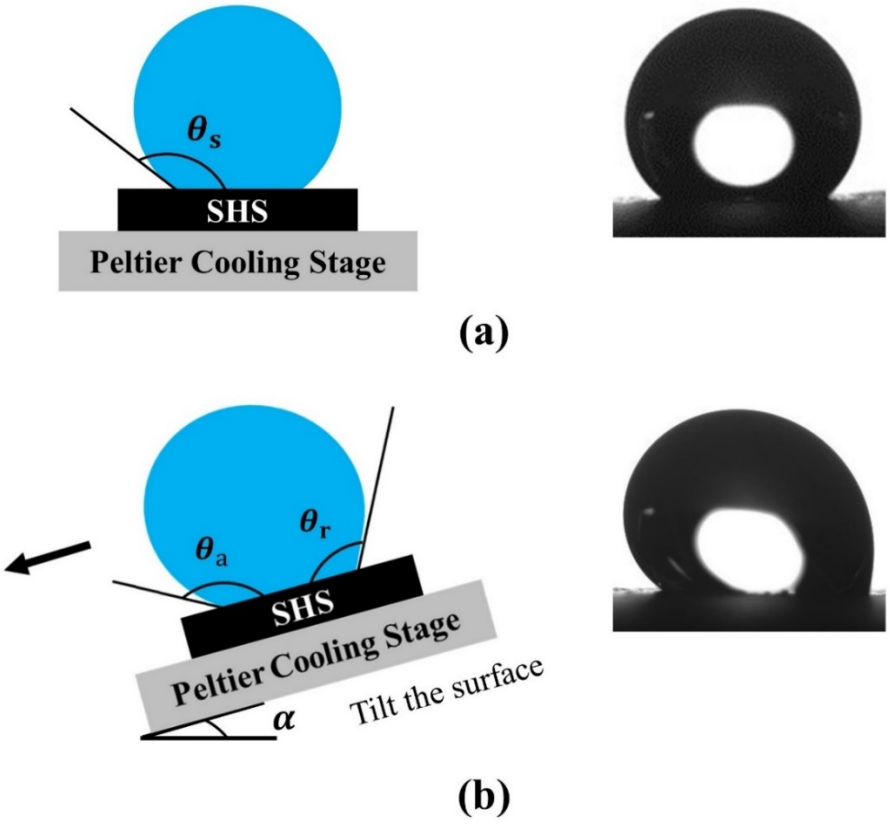

Figure 4.3 (a) Schematic diagram of measuring the static contact angle θ_s of a sessile droplet on a flat SHS, and the real-time image of a sessile droplet on SHS at T_s = 268 K during measurement. (b) Schematic diagram of measuring the advancing contact angle θ_a, receding contact angle θ_r, and sliding angle α of a sessile droplet on a tilted SHS and the real-time image of a sessile droplet on SHS at T_s = 268 K before triple-phase contact line movement.

4.3. Experimental results

In this chapter, the condensation-initiated wetting transition of an impact water droplet on an SHS under various experimental conditions is compared in Chapter 4.3.1. In Chapter 4.3.2, the wetting transition of a sessile water droplet on an SHS is analyzed. Chapter 4.3.3 compares the wetting transition caused by an impact water droplet and a sessile water droplet on an SHS near freezing temperatures.

4.3.1. Condensation-initiated wetting transition from the Cassie-Baxter to Wenzel state during droplet impact

Previously, Heydari et al. [82] and Karmouch et al. [144] pointed out that there was a tremendous decrease in the receding contact angle of a sessile water droplet on SHS as the surface temperature decreased to below 273 K. Because the Cassie–Baxter state to Wenzel state wetting transition occurred as condensation or frost accumulated within SHS cavities. In these two studies [82,144], the receding contact angle was measured when triple-phase contact line receded on tilted SHS. As it can be seen from previously presented Figures. 3.5, 3.7 and 3.10, in this experiment although the contact between impinging water droplet and SHS occurs in the time scale of millisecond, the condensation inside hierarchical surface textures possibly causes the wetting transition from Cassie–Baxter state to Wenzel state. During droplet recoiling on SHS, the triplet-phase contact line keeps receding. In our work, to illustrate this wetting transition under different experimental conditions, the average contact angle $\overline{\theta_c}$ during receding process of an impinging water droplet on SHS is measured and compared (Figure 4.4). The average contact angle $\overline{\theta_c}$ on SHS is evaluated every millisecond from the moment of droplet recoil (3 ms, 4 ms, and 6 ms for D_S, D_M and D_L, respectively) to the moment of droplet break-up. When droplet adhesion to SHS occurs, $\overline{\theta_c}$ is recorded from 4 ms to 20 ms for droplet with diameter D_M, and from 6 ms to 30 ms for droplet with diameter D_L.

Figure 4.4a shows the change in $\overline{\theta_c}$ for droplet with diameter D_M at 278 K impinging on SHS as T_s is reduced. When T_s decreased from 283 K to 248 K, $\overline{\theta_c}$ reduced from approximately 150° to 90°. This demonstrated the occurrence of wetting transition from Cassie–Baxter state to Wenzel state as the accumulation of condensed water increased

(Figure 3.18). Figure 4.4b shows the influence of T_{wd} on surface wettability. When T_{wd} was increased from 278 K to 293 K, during recoiling process, the average contact angle $\overline{\theta_c}$ decreased apparently. This was because the increase in water droplet temperature accelerated condensation of water vapor on cold SHS (Figure 3.17). Fig. 4.4c shows the effects of droplet size D on wetting transition when T_{wd} = 283 K. For impinging droplet with larger diameter D_M or D_L, the contact time of droplet-SHS was prolonged. Accordingly, the amount of condensation inside micro/nano surface structures increased (Figure 3.19). Therefore, under same temperature conditions, as T_s decreased, a more conspicuous tendency of decrease in $\overline{\theta_c}$ was observed for larger droplets.

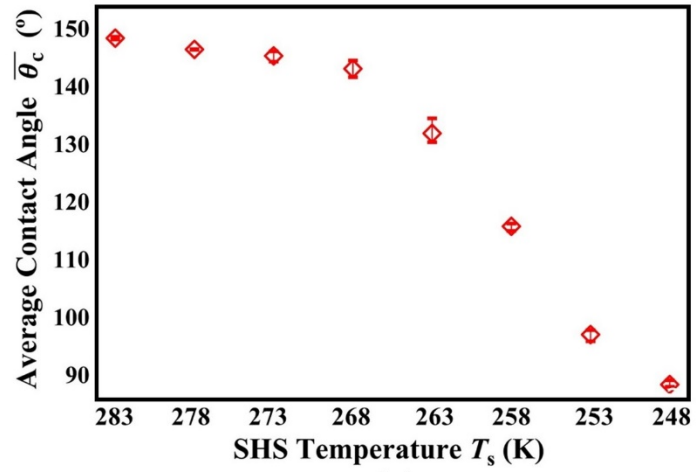

(a)

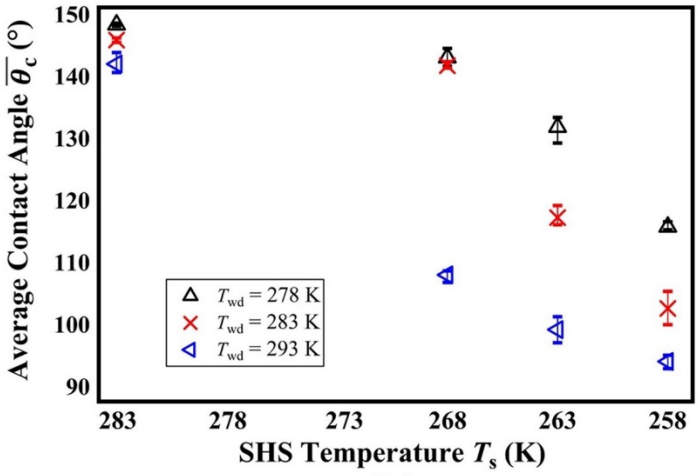

(b)

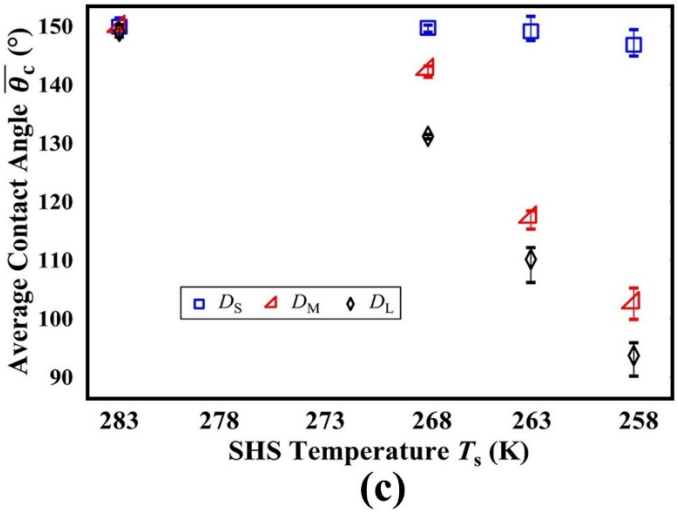

Figure 4.4 Average contact angle $\overline{\theta_c}$ during receding process of an impinging water droplet on SHS under different experimental conditions. (a) Water droplet of diameter D_M with T_{wd} = 278 K impinging on SHS at T_s = 283–248 K, (b) Water droplet of diameter D_M with T_{wd} = 278–293 K impinging on SHS at T_s = 283–258 K, and (c) Water droplet of temperature 283 K with diameters D_S, D_M and D_L impinging on SHS at T_s = 283–258 K.

4.3.2. Wetting transition induced by a sessile water droplet

Figure 4.5 shows the droplet profiles of contact angle measurement of a sessile water droplet with the initial temperature of 278 K on an SHS controlled at different temperatures form 283 K to 258 K. Figure 4.6 shows the experimental results of the contact angle changes. When SHS temperature T_s was decreased from 283 K to 278 K, all three contact angles (θ_s, θ_a, and θ_r) and SHS tilt angle α kept nearly unchanged. Because the SHS temperature was controlled higher than the initial temperature of the water droplet and vapor condensation did not take place within SHS textures. As T_s decreased to 268 K, there was a minor decrease in θ_s and θ_a, but an obvious decrease in θ_r and a conspicuous increase in α. This was caused by the increased adhesion between the sessile water droplet and SHS as the condensed water accumulated inside SHS structures [82,144]. When the SHS temperature was decreased from 268 K to 258 K, all three

contact angles (θ_s, θ_a, and θ_r) and SHS tilt angle α remained nearly the same. The underlying physics will be analyzed in Chapter 4.3.3.

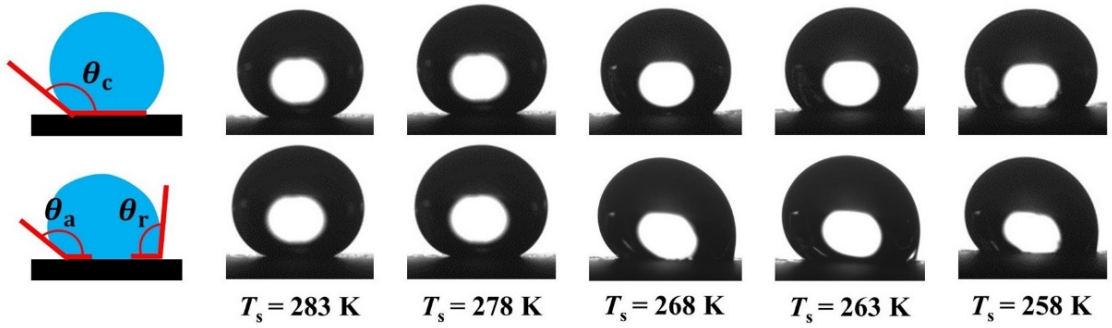

Figure 4.5 Profiles of a sessile water droplet of diameter D_M with T_{wd} = 278 K on super-hydrophobic surface controlled at different temperature T_s = 283–258 K during contact angle measurement.

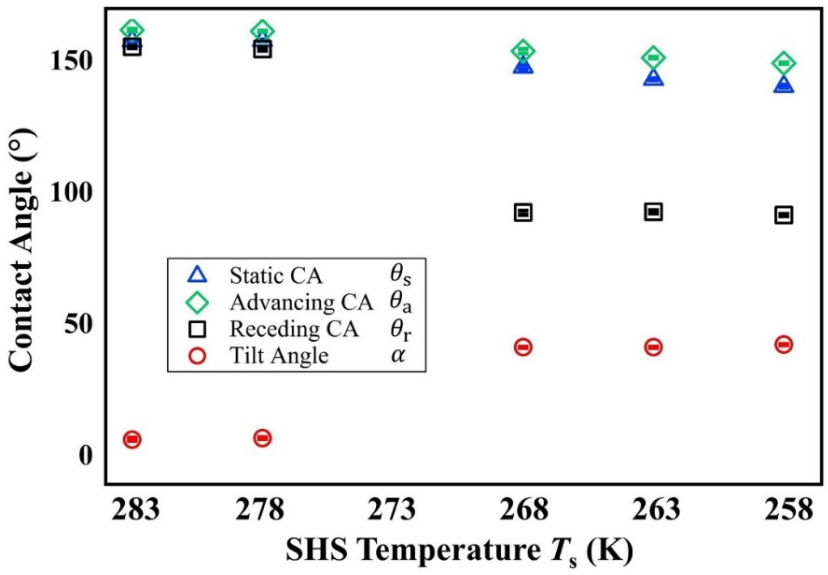

Figure 4.6 Static contact angle θ_s, advancing contact angle θ_a, receding contact angle θ_r, and surface tilt angle α of a sessile water droplet of diameter D_M with T_{wd} = 278 K on SHS controlled at different temperature T_s = 283–258 K.

4.3.3. Comparison of wetting transition of SHS induced by an impact droplet and a sessile droplet

Figure 4.7 compares $\overline{\theta_c}$ change of an impact water droplet (at 278 K) on an SHS (283–248 K) with θ_r change of a sessile water droplet (at 278 K) on an SHS (283–258 K). As T_s decreased from 283 K to 278 K, both $\overline{\theta_c}$ and θ_r demonstrated an ignorable change. However, when T_s was reduced to below 278 K, water condensation started within SHS textures so $\overline{\theta_c}$ and θ_r became smaller. Figure 4.8 compares different regimes of water condensation inside cold SHS micro/nano structures for an impact water droplet and a sessile water droplet. For impact water droplet, $\overline{\theta_c}$ gradually decreased as T_s changed from 273 K to 248 K (Figure 4.7). Nevertheless, for sessile water droplet, θ_r displayed a weak dependency on SHS temperature when T_s was reduced from 268 K to 258 K. For impact water droplet the contact time was within tens of milliseconds. But for sessile water droplet during the measurement of contact angles, the condensation lasted for approximate 80 s. Therefore, with the decrease of T_s, during droplet recoil the decease of $\overline{\theta_c}$ showed its dependency on surface temperature for impact water droplet. For a sessile water droplet, owing to the sufficient time for vapor condensation, SHS micro/nano textures might be completely filled with condensed water when T_s was below 268 K. Hence, as T_s was reduced from 268 K to 258 K, θ_r remained nearly the same.

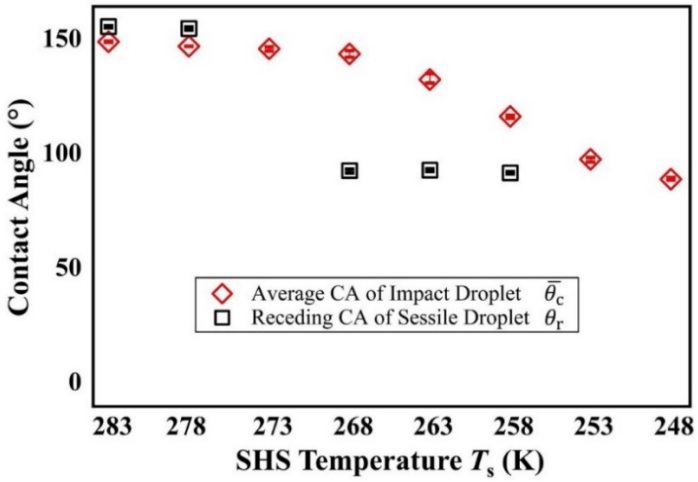

Figure 4.7 Comparison between $\overline{\theta_c}$ change of an impact water droplet of diameter D_M with T_{wd} = 278 K and θ_r change of a sessile water droplet of diameter D_M with T_{wd} = 278 K on a super-hydrophobic surface at different surface temperature T_s = 283–248 K.

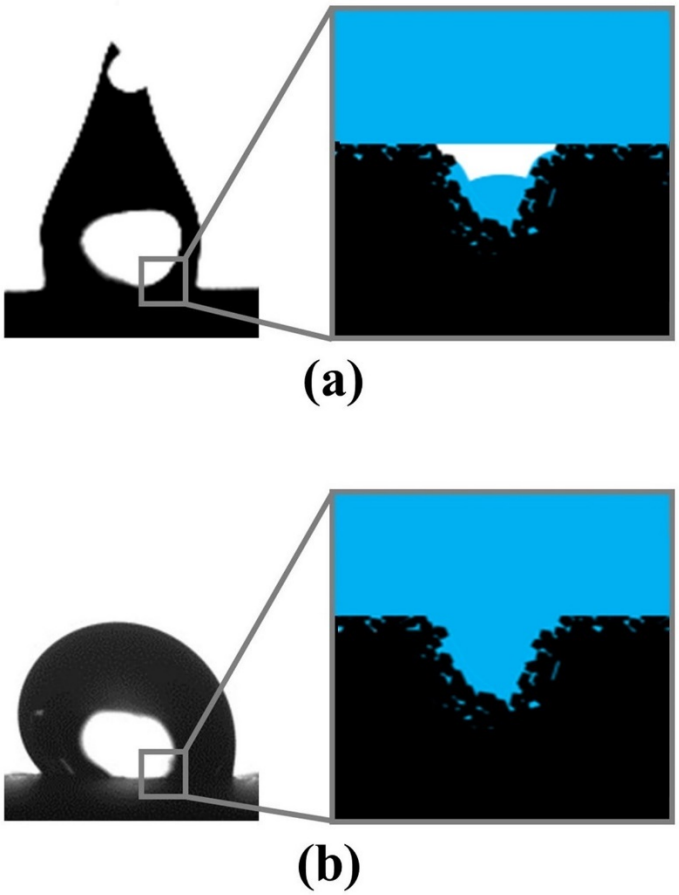

Figure 4.8 Comparison between the schematic diagram of water condensation regimes inside hierarchical micro/nano textures of a cold super-hydrophobic surface for an impact water droplet and a sessile water droplet. (a) An impact water droplet of diameter D_{M} with T_{wd} = 278 K on a cold SHS. (b) A sessile water droplet of diameter D_{M} with T_{wd} = 278 K on a cold SHS.

4.4. Discussions

During the impact process of a water droplet on an SHS near the freezing temperatures, because of the wetting transition initiated by the vapor condensation within SHS hierarchical micro/nano textures, the adhesion between impact droplet and SHS increases. Thus, during droplet rebound, there is an increase of energy loss due to

droplet-SHS adhesion. Chapter 4.4.1 introduces the theoretical modeling of the energy analysis during droplet impact. Chapter 4.4.2 illustrates the results of energy analysis and summarizes the droplet impact behaviors, condensation mechanisms, and energy losses when an impact water droplet collides on an SHS near freezing temperatures.

4.4.1. Theoretical modeling of energy analysis during droplet impact process

When wetting transition from the Cassie-Baxter state to Wenzel state happened, as mentioned in Chapter 4.3, the adhesion between droplet and SHS was enhanced, and thus more kinetic energy was spent during droplet impact. This chapter estimates the energy loss of completely rebounded droplets after impacting on SHS under various experimental conditions. When an impinging water droplet was spreading on SHS, the droplet deformation was dominated by inertial and viscous forces, and the effect of substrate was minor [58,61]. Therefore, it was assumed that there was no energy loss due to the adhesion between droplet and SHS during the spreading process. From the moment of initial droplet contact with SHS to the moment of maximum spreading, kinetic energy of droplet was converted to surface energy, meanwhile part of kinetic energy was lost because of viscous dissipation during droplet spreading. During droplet recoiling, the surface energy of droplet was converted to kinetic energy, at the same time, kinetic energy was reduced because of the viscous loss and droplet-SHS adhesion [55,145]. It was challenging to directly estimate the viscous loss E_{μ} owing to the complex droplet deformation during spreading and recoiling process. Therefore, the viscous loss E_{μ} was calculated by subtracting the energy loss due to droplet-SHS adhesion E_{a} from the total energy loss E_{loss} [145,146]. When a droplet broke up into small droplets or a droplet became stuck to SHS, it was challenging to estimate the droplet surface energy in the final state. Thus, the analysis was carried out only when a single droplet rebounded. Details of the calculation are as follows:

Total energy loss E_{loss} during droplet impact can be calculated as,

$$E_{\mathrm{loss}} = E_0 - E_{\mathrm{r}} \tag{4.1}$$

where E_0 and E_{r} are the total energy of the droplet before impinging and after rebounding respectively. The total energy is the summation of potential energy and surface energy of

the droplet. When the droplet rebounds completely, it can be assumed that surface energy of the droplet before impinging and after rebounding are almost the same as the droplet size does not change so much. (The droplet size changes due to evaporation during droplet impact can be estimated based on the mass balance as: $\sqrt{\mathcal{D}t_c} \cdot 4\pi R^2 \cdot \rho_{wv} = 4/3\pi(R^3 - (R-\delta)^3) \cdot \rho_w$. Taking the contact time t_c = 15 ms, the thickness of evaporated water is calculated as $\delta = 2.7e^{-6}m$, then $\delta/D = 0.11\ \%$). Hence, E_{loss} is given by the difference of potential energy:

$$E_{loss} = E_{p0} - E_{pr} = mg(H_0 - H_r) \tag{4.2}$$

In literature, to evaluate the adhesion between an impact water droplet and SHS, the work of adhesion W_a based on the Young-Dupré equation [147–149] was widely employed. For instance, Lee et al. [148] and Li et al. [149] mentioned the adhesion increase between an impact water droplet and SHS with decreasing contact angle via the Young-Dupré equation. In addition, Heydari et al. [82,83] calculated the work of adhesion W_a based on the modified Young-Dupré equation [53,150,151] using the receding contact angle θ_r to estimate the energy spent to separate a sessile droplet from SHS, which was,

$$W_a = \gamma(1 + \cos\theta_r) \tag{4.3}$$

where γ is the surface tension between water and air. The receding contact angle θ_r is defined as the threshold value for the triple-phase contact line movement when droplet recedes [140,141]. In the present work recoiling of droplet on SHS was accompanied by the triple-phase contact line movement with a small change of instantaneous contact angle (Figure 4.1a and Figure 5.3), the work of adhesion W_a was estimated by taking the average value of $\bar{\theta}_c$ during the recoiling process (Figure 4.4),

$$W_a = \gamma(1 + \cos\bar{\theta}_c) \tag{4.4}$$

The value of γ was determined by the equation for the temperature-dependent surface tension between water and air in the literature [132] and the energy loss due to droplet-SHS adhesion E_a was calculated as,

$$E_a = W_a A_c \tag{4.5}$$

where A_c is the contact area calculated as,

$$A_c = (\pi/4)d_{max}^2 \quad (4.6)$$

where d_{max} denotes the maximum contact length of impinging water droplet on SHS (Table A.3 in Appendix E). The energy loss due to viscosity E_μ is approximated as,

$$E_\mu = E_{loss} - E_a \quad (4.7)$$

Figure. 4.9 displays the schematic diagram of energy analysis when a water droplet collides on the SHS in initial state of droplet impact, droplet receding process, and final state of the rebound droplet. In this work, direct validation of Equation 4.4 and Equation 4.5 is challenging via the current experimental setup. Through calculating the viscous loss using CFD simulations, Chapter 5.3.2 validates the energy loss analysis.

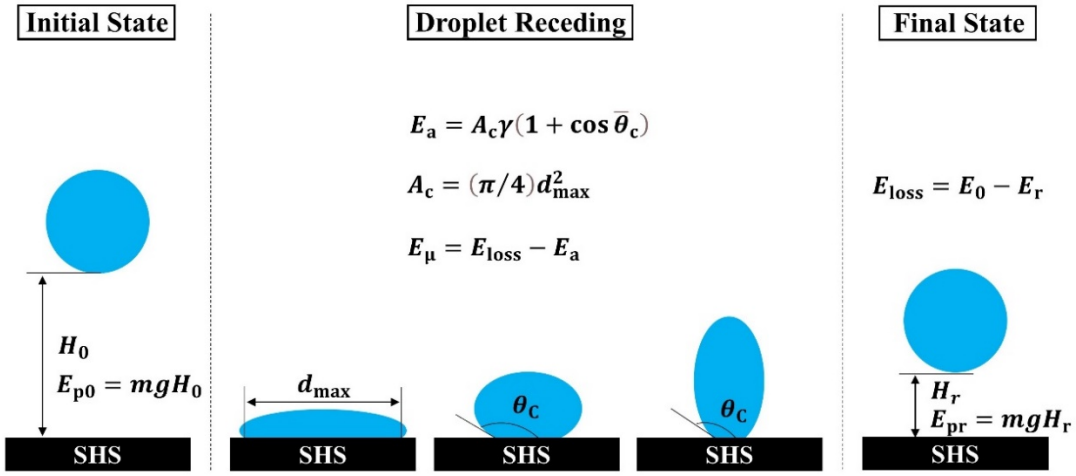

Figure 4.9 Schematic diagram of energy analysis during the initial state, droplet receding process, and final state of an impact water droplet on an SHS.

4.4.2. Energy analysis of droplet bouncing on a super-hydrophobic surface

Figure 4.10 shows the potential energy of rebounding water droplet and the energy losses when a water droplet with diameter D_M and temperature 278 K impinges on SHS as T_s decreases from 283 K to 258 K. When T_s was 253 and 248 K, a water droplet did not rebound completely (Figure 3.5). As T_s was maintained between 283 K to 268 K, the amount of condensed water on SHS was minimal. Therefore, the average contact angle $\bar{\theta}_c$ remained almost unchanged and E_a was also identical. Then, the impinging droplet had a similar amount of residual energy to rebound to an approximately equal height. As T_s

further decreased to 263 K and 258 K, the wetting transition occurred which was evident from the average contact angle $\overline{\theta_c}$ (Figure 4.4a). Accordingly, the energy loss caused by droplet-SHS adhesion E_a steadily increased. Therefore, the droplet possessed less energy to depart from SHS and bounced to a lower height.

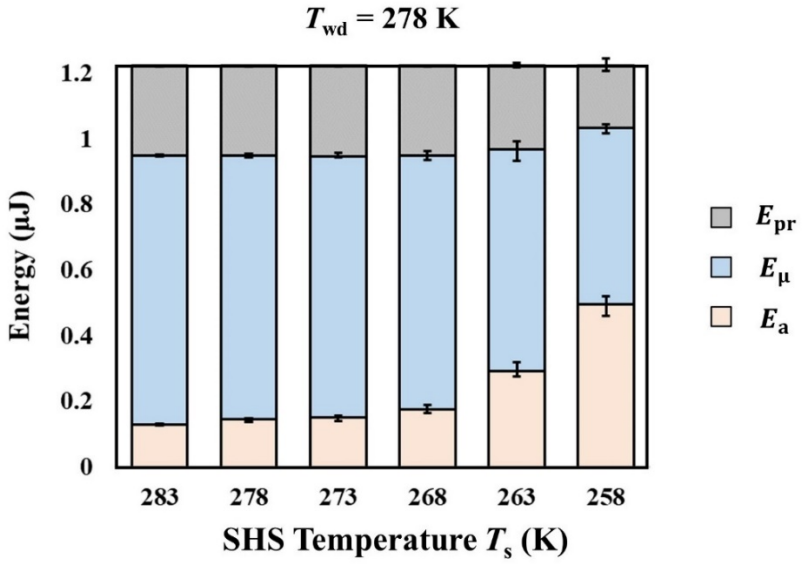

Figure 4.10 Potential energy E_{pr}, energy loss due to viscosity E_μ, and energy loss due to adhesion E_a of a water droplet with diameter D_M and temperature T_{wd} = 278 K impinging on an SHS at T_s = 283 K to 258 K.

Figure 4.11 illustrates the energy losses affected by the water droplet temperatures. The increase in water droplet temperature accelerated the rate of vapor condensation on a cold SHS (Figure 3.17), and thus an increase in the amount of condensed water during droplet-SHS contact (Figure 3.18) and a more apparent wetting transition took place (Figure 4.4b). Due to droplet-SHS adhesion, more energy was consumed for the impinging water droplet with higher temperatures (Figure 4.11). Therefore, the impinging water droplet had less residual energy to rebound lower or even became adhered to SHS.

Figure 4.12 displays the energy losses affected by the droplet sizes. The increase in water droplet size caused the prolongment of contact time of impinging water droplet on SHS (Figure 3.11). Accordingly, the amount of condensed water on SHS increased (Figure 3.19), and a more apparent trend of decrease in $\overline{\theta_c}$ was observed (Figure 4.4c). Therefore, with the increase in droplet diameter, there was a more apparent trend in

energy loss caused by droplet-SHS adhesion (Figure 4.12). Correspondingly, a clearer trend of decreasing residual energy with the decrease in T_s was observed.

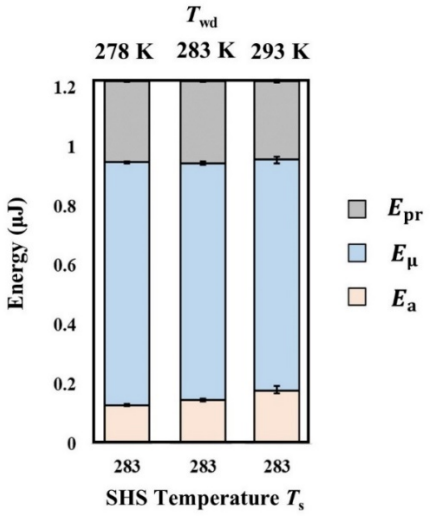

Figure 4.11 Potential energy E_{pr}, energy loss due to viscosity E_μ, and energy loss due to adhesion E_a of a water droplet with diameter D_M and temperature T_{wd} = 278–293 K impinging on an SHS at T_s = 283 K.

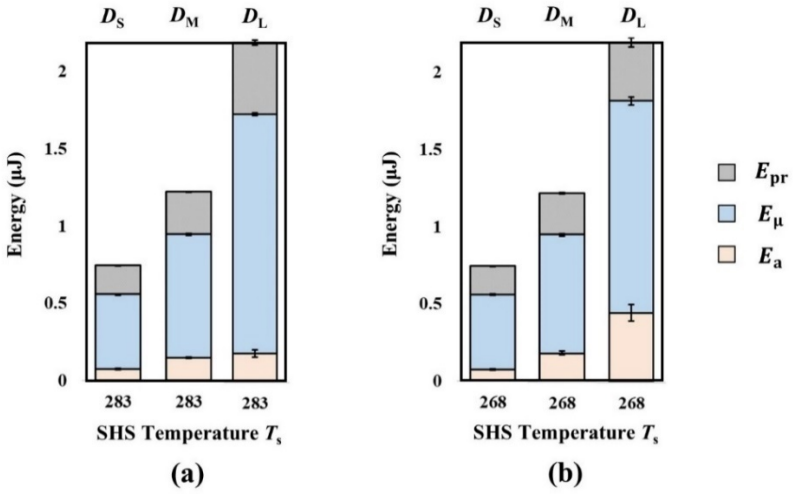

Figure 4.12 Potential energy E_{pr}, energy loss due to viscosity E_μ, and energy loss due to adhesion E_a of a water droplet with temperature 283 K and diameters D_S, D_M, and D_L impinging on an SHS at T_s = 283 K and 268 K. (a) T_s = 283 K and (b) T_s = 268 K.

4.5. Summary

Because the condensed water accumulated inside hierarchical micro/nano textures of cold SHS, wetting transition from Cassie-Baxter state to Wenzel state occurred and the super-hydrophobicity of the surface could no longer be preserved. The formed water bridges also yielded the increase of droplet-SHS adhesion. Owing to the adhesion between impinging droplet and water bridges within micro/nano surface cavities, a larger amount of kinetic energy was spent during droplet rebound. Therefore, less residual energy remained. The decrease in the residual energy resulted in an extended contact time and a reduction in rebounding height. At a lower SHS temperature or a higher water droplet temperature, an increment of the rate of water condensation on SHS and a more obvious tendency of wetting transition were observed. In addition, with an increase in droplet size there was an extended droplet-SHS contact time as well as an increase of the amount of condensed water, enhancing the wetting transition.

In addition, this study investigated the wetting transition of a sessile water droplet on a cold SHS from the Cassie-Baxter state to Wenzel state induced by the condensation of evaporated water vapor inside SHS hierarchical micro/nano textures. The receding contact angle of a sessile water droplet with the initial temperature of 278 K on an SHS with different temperatures (283–258 K) was measured and selected as the performance parameter. Compared with SHS at 283 K and 278 K, there was a significant decrease in receding contact angle when SHS temperature was reduced to 268 K, which might be caused by the existence of condensed water inside SHS micro/nano structures. When SHS was changed from 268 K to 258 K, the receding contact angle demonstrated a weak dependency on surface temperature owing to the sufficient time for vapor condensation to completely fill SHS micro/nano structures with condensed water.

This chapter demonstrated the wetting transition caused by an impact water droplet on a cold SHS and the significance of wetting transition to the behaviors of droplet rebounding on an SHS near freezing temperatures. In Chapter 5, the occurrence of wetting transition ($\overline{\theta_c}$ in Figure 4.4) measured from experiments will be added a wall boundary condition in the CFD simulation to investigate the droplet impinging behaviors on SHS near freezing temperatures.

Chapter 5 Numerical Study of a Water Droplet Impact on a Super-hydrophobic Surface near Freezing Temperatures

5.1. Introduction

Droplet impact phenomena [152] onto solid surfaces are critical to a variety of industrial applications and natural processes such as 3D printings [153], spray coatings [154], pesticide depositions [155], raindrops falling on buildings [156], and in-flight cloud droplets impacting on airflight surfaces [42]. Recently, various approaches have been developed to fabricate artificial SHSs [11,157] and an impact droplet has been found to completely retract and elastically rebound on an artificial SHS [55]. Owing to this unique characteristic, SHS has been widely considered in many engineering technologies related to droplet impingements such as anti-icing [74], self-cleaning [39], anti-fogging [158], and anti-biofouling [159]. Therefore, a systematic understanding of droplet impact behaviors on a surface is necessary to the industrial processes mentioned above.

When a droplet impacts on surface, depending upon the surface properties (e.g., surface wettability) and droplet physical parameters (e.g., viscosity, surface tension coefficient, impact velocity, and droplet dimension), there are possible outcomes [59] including deposition, break-up, splashing, and fully rebound. For the impact of a droplet on a surface, it undergoes a lateral spreading with the conversion of kinetic energy to interfacial energy. Extensive attentions [60–64] have been devoted to the experimentally measuring and mathematically deriving the maximum contact areas of impact droplets on surfaces due to its importance to practical applications. To predict the maximum droplet spreading, through balancing droplet inertia, surface energy, and viscous loss, several theoretical correlations [60–64] have been developed. During the droplet spreading process, the effect of the droplet-surface adhesion is minor and thus ignorable [60–64].

After the maximum spreading, especially for an impact droplet on SHS, the droplet surface energy decreases [131] as the retraction takes place. The retraction dynamics of droplet is governed by surface energy, inertia, viscosity, and droplet-surface adhesion [55,160]. Retraction velocity [160] has been employed to evaluate the de-wetting process. Bartolo et al. [160] showed that with the increase of droplet viscosity or Ohnesorge number (i.e., the ratio of viscous forces over inertial and capillary forces, mathematically expressed as, $Oh = \mu/\sqrt{\rho\gamma D}$) to around 0.05, droplet retraction velocity changes from capillary-inertial regime to capillary-viscous regime. Maitra et al. [125] investigated that due to the viscosity increment of supercooled metastable water, an impact water droplet forfeits its rebounding capability on an SHS. Aria et al. [161] investigated the influence of Weber number ($We = \rho v D/\gamma$) on droplet impact behaviors through altering the impact velocity and demonstrated the formation of secondary droplets at moderate Weber number (57.5) and droplet splashing at higher Weber number (151.8). Mishchenko et al. [74] focused on the behaviors of supercooled droplets impinging on SHSs maintained down to 243 K and concluded that as ice nucleation occurs, the droplet-SHS adhesion increases, hindering the droplet retraction and rebound. Shen et al. [142] experimentally compared droplet impacting performance on surfaces with different contact angle hysteresis (CAH) and demonstrated that the increase in CAH generates a larger droplet-surface resistance force, against which there is an increase in the work done during the droplet recoiling process. Correspondingly, as surface CAH increases, the retraction of impact droplet decelerates with the increment of contact time. For many practical applications [74,158], to shorten the contact between droplet and surface is crucial in that it determines the extent of thermal energy conversions [94]. Therefore, by altering the surface texture and surface roughness, the droplet recoiling dynamics can be modified to reduce contact time, such as non-asymmetric droplet retraction [67] and pancaking bouncing [68].

However, under certain circumstances, it is challenging to probe the droplet impact process on a surface via experiments [94]. Therefore, numerical simulations have been carried out. For instance, Dwiyantoro et al. [97] and Liu et al. [73] presented that with the increase of surface tension there is a reduction in the maximum spreading of an impact water droplet on a surface. Lee et al. [63] showed that the increment in droplet viscosity

confines the droplet maximum deformation on a surface. Qu et al. [98] demonstrated the influence of droplet impact velocities and Weber numbers on droplet maximum deformations and the occurrence of droplet splashing at high Weber number of 197.5. In addition, some interesting droplet bouncing behaviors have been investigated numerically, including the coalescence of an impinging water droplet with a sessile water droplet [99], droplet impact on an inclined SHS [100], and droplet impact on a spherical SHS [73].

Furthermore, when a water droplet impacts on a supercooled surface, ice nucleation inside the droplet has been taken into consideration numerically [101–104]. These works [101–104] assume that droplet freezing takes place at the moment of contact with a substrate. In these works [101–104], a source term is added in the momentum equation accounting for the adhesion increase due to droplet freezing. Zhang et. al. [101] compared the numerical and experimental droplet rebounding performance on an SHS at different temperatures and demonstrated that ice nucleation led to the forfeit of droplet rebound when surface temperature was reduced to 243 K. Chang et al. [102] studied the impacting dynamics and freezing behaviors of a micro-meter size water droplet on a surface in supercooled environment for the sake of exploring the mechanism of aircraft icing. Yao et. al. [103] numerically investigated the impacting and freezing process of a water droplet on an inclined surface at ultra-cold temperatures (173K). Attarzadeh et. al. [104] focused on the freezing of a supercooled microscale water droplet on an SHS in consideration of the SHS uniform surface textures. The outcomes of these numerical simulations [101–104] show that the droplet freezing determines the rebounding or sticking performance of an impact water droplet on a cold SHS. The above-mentioned numerical modeling studies are important to industrial applications and theoretical processes relevant to droplet impact phenomena. However, majority of available mathematical investigations model the non-bouncing droplets, the lack of analysis of bouncing state is noticeable in literature, requiring further studies [94].

This chapter executes CFD simulations based on VOF method to reproduce droplet impacting behaviors on SHS near freezing temperatures observed from experiments in Chapter 3 and Chapter 4. The contact angle measured in experiment is added as a wall boundary condition via the continuum surface force model and wall adhesion model.

Viscous loss of the rebounding water droplet is calculated numerically to validate the energy loss analysis in Chapter 4.4. Time-course viscous losses during droplet spread, recoil, and rebound processes are analyzed to elucidate the droplet impact behaviors. Via parameter study (incl., receding contact angle, water viscosity, and surface tension), this work seeks to investigate the dominant mechanism determining droplet impacting behaviors observed in our experiments and further analyze the droplet rebounding dynamics in bouncing state from the perspective of energy loss and surface tension force. In addition, this work seeks to come up with an approach to predict droplet rebounding performance on a surface in consideration of the maximum viscous loss and adhesion loss during droplet impact. Interpretation of the physics of an impact water droplet in bouncing state and the viscous losses during droplet impingement on surfaces will give valuable hints on super-hydrophobic surface designs for real applications.

5.2. Simulation methodology

In this work, the explicit volume of fluid (VOF) method in ANSYS Fluent [162] is employed to capture the two-phase flow between immiscible liquid and gas. VOF method is utilized because it is a simple but powerful computational method of flexibly and efficiently treating complicated boundary configurations [95]. Although VOF suffers from a lack of resolution at the interface region, level set method [96] is not utilized due to the concerns of mass conservation and instability of boundaries [163]. Governing equations and related models are summarized in Chapter 5.2.1. Geometry of the computational domain, boundary conditions, and initial conditions are explained in Chapter 5.2.2. Mesh information and fluid properties considered in this work are introduced in Chapter 5.2.3 and Chapter 5.2.4, respectively. The computational solvers employed in this work are mentioned in Chapter 5.2.5.

5.2.1. Governing equations and related models

For VOF method [95], liquid volume fraction α_l is employed, which is defined as the ratio of volume of liquid over the volume of the computational cell. Liquid phase and

gas phase can be identified based on the value of α_l. As shown in Equation 5.1, when α_l equals to 1 and 0 the phase is liquid and gas, respectively. When the value is between 1 and 0, the cell belongs to the interface region. In this work, liquid fraction equation, mass conservation equation, momentum conservation equation, and energy conservation equation are solved.

$$\begin{aligned} &\alpha_l = 1 \quad \text{liquid} \\ &0 < \alpha_l < 1 \quad \text{interface} \\ &\alpha_l = 0 \quad \text{gas} \end{aligned} \tag{5.1}$$

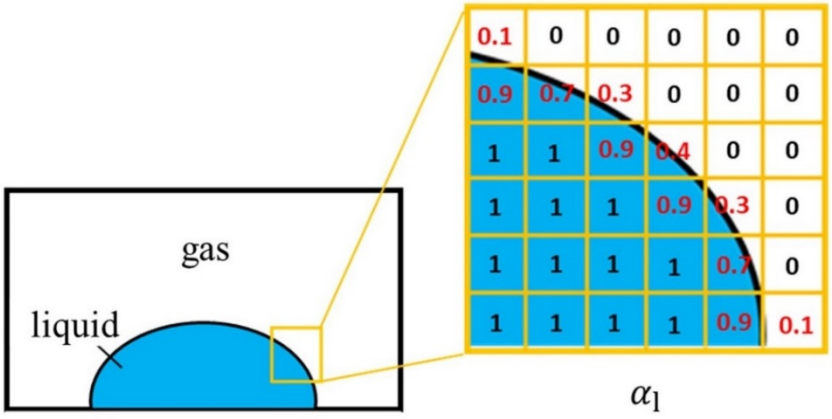

Figure 5.1 Schematic diagram of the liquid volume fraction α_l employed in the volume of fluid (VOF) method.

5.2.1.1 Liquid fraction equation

The liquid fraction equation is given as,

$$\frac{\partial \alpha_l}{\partial t} + \nabla \cdot (\alpha_l \boldsymbol{V}) = 0 \tag{5.2}$$

where $\boldsymbol{V}$ is velocity and t is time. Then the volume fraction of gas α_g defined as the ratio of volume of air over volume of computational cell, which can be computed as,

$$\alpha_g = 1 - \alpha_l \tag{5.3}$$

5.2.1.2 Mass conservation equation

The mass conservation equation between liquid and gas phases can be expressed as,

$$\frac{\partial \rho}{\partial t} + \nabla \cdot (\rho \boldsymbol{V}) = 0 \tag{5.4}$$

where the density ρ is obtained depending upon the volume fraction of liquid and gas, as follows,

$$\rho = \alpha_{\mathrm{l}} \rho_{\mathrm{l}} + \alpha_{\mathrm{g}} \rho_{\mathrm{g}} \tag{5.5}$$

where ρ_{l} and ρ_{g} are the density of liquid and gas, respectively.

5.2.1.3 Momentum conservation equation

The governing equation for momentum conservation is calculated as,

$$\frac{\partial (\rho \boldsymbol{V})}{\partial t} + \nabla \cdot (\rho \boldsymbol{V}\boldsymbol{V}) = -\nabla p + \nabla \cdot \mu [\nabla \boldsymbol{V} + (\nabla \boldsymbol{V})^T] + \rho \boldsymbol{g} + \boldsymbol{F}_{\boldsymbol{\gamma}} \tag{5.6}$$

where p is pressure, $\boldsymbol{g}$ is gravitational constant, and $\boldsymbol{F}_{\boldsymbol{\gamma}}$ is volumetric surface tension force acting on the liquid-gas interface. For the volumetric gravity $\rho \boldsymbol{g}$**,** the direction is the same as the direction of droplet impact on SHS. The viscosity μ is calculated based on the volume fraction of liquid as well, which is given by,

$$\mu = \alpha_{\mathrm{l}} \mu_{\mathrm{l}} + (1 - \alpha_{\mathrm{l}}) \mu_{\mathrm{g}} \tag{5.7}$$

For the volumetric surface force term $\boldsymbol{F}_{\boldsymbol{\gamma}}$ in the momentum conservation equation, the continuum surface force (CFS) model developed by Brackbill et al. [164] has been adopted by previous researchers [101–104], in which a water droplet impacts on an SHS under different temperature conditions with the occurrence of droplet rebounding from or sticking to the surface. CFS model [164] was developed through balancing the pressure difference between interface of liquid and gas and correlating the surface force with curvature of the interface. This method makes it possible that the surface tension can be modeled as a body force $\boldsymbol{F}_{\boldsymbol{\gamma}}$. Owing to the good agreement between experimental and simulation results [101–104], this work also utilizes the continuum surface force model. Through this continuum surface force model, the surface force could be plotted and

analyzed as well. Based on the surface tension coefficient γ, curvature of the liquid-gas interface κ, and the interface normal $\boldsymbol{n}$, $\boldsymbol{F_\gamma}$ (towards the liquid) is calculated as,

$$\boldsymbol{F_\gamma} = \frac{\gamma \rho \kappa \boldsymbol{n}}{0.5\left(\rho_g + \rho_l\right)} \tag{5.8}$$

where the curvature of the interface κ and the interface normal $\boldsymbol{n}$ are calculated as [168],

$$\kappa = -(\nabla \cdot \hat{\boldsymbol{n}}) = -\left(\nabla \cdot \frac{\boldsymbol{n}}{|\boldsymbol{n}|}\right) \tag{5.9}$$

$$\boldsymbol{n} = \nabla \alpha_l \tag{5.10}$$

where $\hat{\boldsymbol{n}}$ represents the unit vector normal to the interface.

5.2.1.4 Energy conservation equation

To calculate the temperature distribution in computational domain during the droplet impact process on SHS, energy conservation equation is adopted. The droplet-SHS contact occurs within around 15 ms as the experimental results demonstrate in Chapter 3. During this short contact between droplet and SHS, the released heat due to condensation of water vapor inside SHS textures with the average height of 5.92 μm is ignorable to the temperature variation of water droplet with the diameter of 2.44 mm. (Released heat due to vapor condensation: $L^3 \rho_w H_{fg} = (5.92e^{-6}\text{m})^3 \times 998\ \text{kg m}^{-3} \times 2257\text{kJ kg}^{-1} = 4.67e^{-10}\text{kJ}$, temperature change of droplet: $4/3\pi R^3 \rho_w\, c_p = 4/3 \times \pi \times (1.22e^{-3}\text{m})^3 \times 998\text{kg m}^{-3} \times 4.21\text{kJ kg}^{-1}\ \text{K}^{-1} = 3.19e^{-5}\ \text{kJ K}^{-1}$, $4.67e^{-10}\text{kJ}/3.19e^{-5}\ \text{kJ K}^{-1} = 1.46e^{-5}$ K, where L is average height of SHS texture, R is droplet radius, ρ_w is water density, H_{fg} is water enthalpy, and c_p is specific heat.) Thus, the heat flux due to vapor condensation is not considered in the energy conservation equation, which is shown as,

$$\frac{\partial\left(\rho c_p T\right)}{\partial t} + \nabla \cdot \left(\rho c_p T \boldsymbol{V}\right) = \nabla \cdot \lambda[\nabla T] \tag{5.11}$$

where T is temperature and the specific heat capacity c_p is obtained based on liquid volume fraction, which is given by,

$$c_p = \alpha_l c_{pl} + (1 - \alpha_l) c_{pg} \tag{5.12}$$

where c_{pl} and c_{pg} are the specific heat of liquid and gas, respectively. The thermal conductivity λ is obtained based on liquid volume fraction, which is given by,

$$\lambda = \alpha_l \lambda_l + (1 - \alpha_l)\lambda_g \tag{5.13}$$

where λ_l and λ_g are the thermal conductivity of liquid and gas, respectively. Specific heat and thermal conductivity of liquid and gas are considered as constant in current simulation due to small deviations within the temperature range of this work as shown in Table 5.1.

For the surface tension coefficient of water in air γ [248–293 K, 165] and viscosity of water μ_w [239–293 K, 124], this work calculates the value based on the temperature of water as shown in Equation 5.14 and Equation 5.15, respectively. These two material properties are involved through the user defined function (UDF) written in C program.

$$\gamma = 75.796 - 0.145(T - 273) - 0.00024(T - 273)^2 \tag{5.14}$$

$$\mu_w = 1.3069 \times 10^{-4} \cdot \left(\frac{T}{224.8} - 1\right)^{-1.7044} \tag{5.15}$$

5.2.1.5 Wall adhesion model

When wetting transition from the Cassie-Baxter to Wenzel state takes place with the accumulation of condensed water in SHS micro/nano textures, as investigated in Chapter 4, the droplet-SHS adhesion increases and the contact angle between droplet and SHS reduces. The wall adhesion model proposed by Brackbill et al. [164] is employed to adjust the curvature of interface at the contact line between droplet and the wall boundary, based on the contact angle values. Then the volumetric surface force term $\boldsymbol{F_\gamma}$ as shown in Equation 5.8 is changed.

To be specific, for the one cell away from the wall boundary (as shown in Figure 5.2), the unit vector normal to the interface between liquid and gas phases $\hat{\boldsymbol{n}}$ can be calculated as a function of contact angle θ between droplet and the wall boundary, as follows,

$$\hat{\boldsymbol{n}} = \hat{\boldsymbol{n}}_{\mathbf{t}}\cos\theta + \hat{\boldsymbol{t}}_{\mathbf{w}}\sin\theta \tag{5.16}$$

where $\hat{\boldsymbol{n}}_{\mathbf{t}}$ is the unit vector tangential to the boundary wall and $\hat{\boldsymbol{t}}_{\mathbf{w}}$ is the unit vector normal to the boundary wall. Based on the unit vector normal to the interface $\hat{\boldsymbol{n}}$, the local curvature near the wall boundary is adjusted.

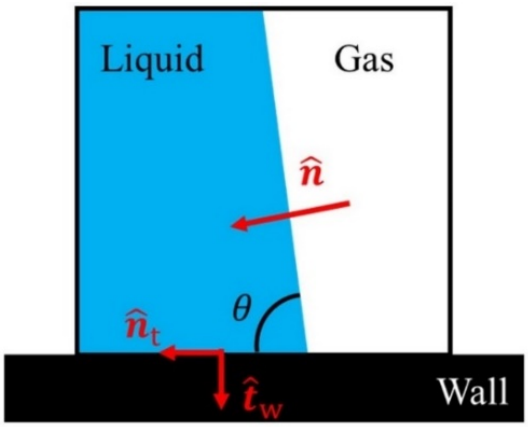

Figure 5.2 Schematic diagram of the unit vector normal to the interface at one cell away from the wall boundary.

5.2.1.6 Quasi-dynamic contact angle model

In literature, several contact angle models have been employed to simulate droplet impinging behaviors on a surface when contact line moves, including fixed contact angle model [61,166], quasi-dynamic contact angle model [167–171], stepwise time variation model (measured via experiments) [61,172], dynamic contact angle model [63,73,99,173], and wetting force model [168], which is to add a volumetric force to momentum equation based on the contact angle value.

In this work, the Weber number is merely at around 10 and the average contact line recoiling velocity is approximately at 0.38 m s^{-1} ($d_{\max}/t_{\text{recoil}} = 3.8e^{-3}$ m$/\,1.0e^{-2} =$ 0.38 m s^{-1}, $d_{\max}$ is shown in Table A.3 and t_{recoil} refers to droplet recoiling time). This small contact line recoiling velocity makes the change of contact angle within 3° based on Kistler's law [174]. (See Appendix F for the calculation of contact angle change). This

work adopts the quasi-dynamic contact angle model [167–171] to the value of contact angle θ during droplet impinging process on SHS. During the droplet spreading process, advancing contact angle θ_a is used because the triplet-phase contact line keeps advancing and θ_a is defined as the threshold value for the advancement of contact line. During droplet recoiling process, since the contact angle is related to the amount of condensed water inside SHS textures and the contact angle has a minor change during the recoiling process (Figure 4.1a and Figure 5.3), this work employs the average contact angle during droplet recoil $\overline{\theta_c}$ measured from experiment (Figure 4.4a) as the contact angle [100]. Figure 5.3 compares the temporal contact angle changes of three repeat experiments and the average contact angle ($\overline{\theta_c}$) utilized in simulations. The quasi-dynamic contact angle is calculated as shown in Equation 5.17 and employed via UDF. For parametric study, receding contact angle θ_r is adopted as the triplet-phase contact line keeps receding in that θ_r is defined as the threshold value for receding of contact line.

$$\begin{aligned} \theta &= \theta_a \quad \text{before maximum spreading} \\ \theta &= \overline{\theta_c} \quad \text{after maximum spreading} \end{aligned} \tag{5.17}$$

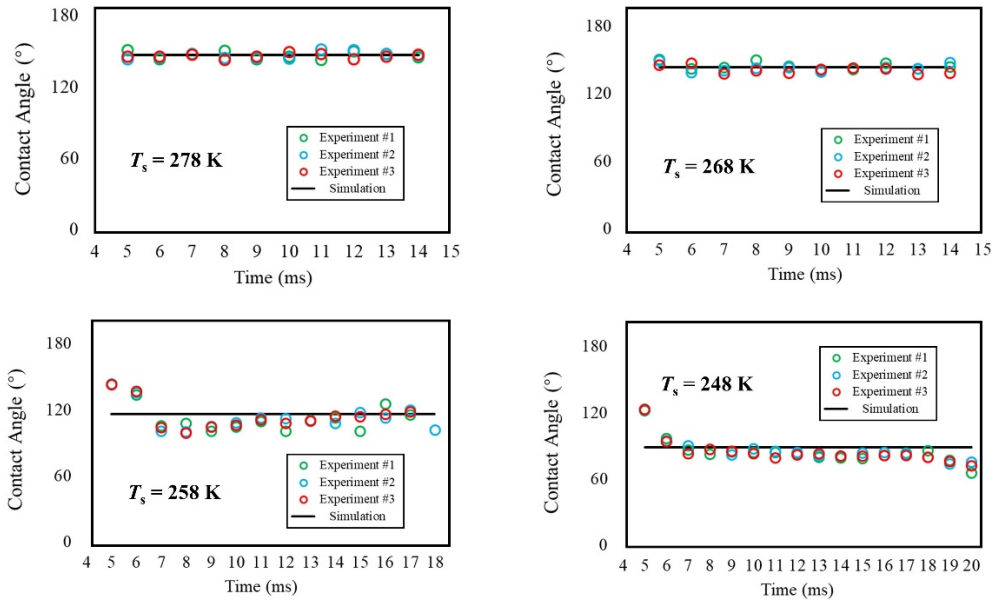

Figure 5.3 Contact angle values measured from experiments and the contact angles utilized in the simulation for SHS at different temperatures from 278 K to 248 K. The temporal contact angles of three repeat experiments during droplet recoil are shown.

5.2.2. Geometry, boundary conditions, and initial values

Figure 5.4a and Figure 5.4b show the dimensions of experimental setup and 2D axisymmetric computational domain in the CFD simulations, respectively. In this work, air and liquid are taken as the primary phase and secondary phase, respectively.

There are three boundaries called SHS, domain boundary, and symmetric axis [162]. For SHS, non-slip boundary condition is adopted so that $\boldsymbol{V} = 0$. Fixed SHS temperature is given and the heat flux q between substrate and the computational cell is calculated as $q = \lambda(T_\mathrm{s} - T_\mathrm{cell})$, where T_cell refers to the temperature of the computation cell next to the SHS. For pressure at the SHS, normal gradient is zero. For domain boundary, normal gradient of velocity and temperature are given as zero. Pressure condition of domain boundary is set the same as the standard atmospheric pressure. At the symmetric axis, normal gradients of all variables are zero.

At the beginning of computation, an impact water droplet with the diameter of 2.44 mm is patched inside the computational domain, where the initial liquid volume fraction α_l is given as 1. Initial impact velocity of the water droplet is calculated as $v = \sqrt{2gH_0}$. Taking H_0 as 16.4 mm, then the initial velocity v is obtained as 0.57 m s^{-1}. Since the droplet impacts on the SHS from a small height, from experiments the droplet shape remains almost circular before contacting the SHS. Meanwhile, due to air resistance during droplet falling, the ratio of deformation of droplet over droplet diameter is 3.9 % ($\Delta x = 1/2\, at^2 = 1/2\, F_\mathrm{drag}/(4/3\,\pi R^3 \rho_\mathrm{w})\,(H_0/v)^2$, the resistance force $F_\mathrm{drag} = 1/2\,\rho_\mathrm{a} A c v^2$, c is the drag coefficient taken as 0.45 for sphere [176]), this study does not take the droplet deformation during falling into consideration. Initial water droplet temperature is set the same as the ambient temperature T_a. Due to the air circulating system within the humidity chamber, a uniform ambient temperature is employed without considering the temperature gradient near the SHS [101–104].

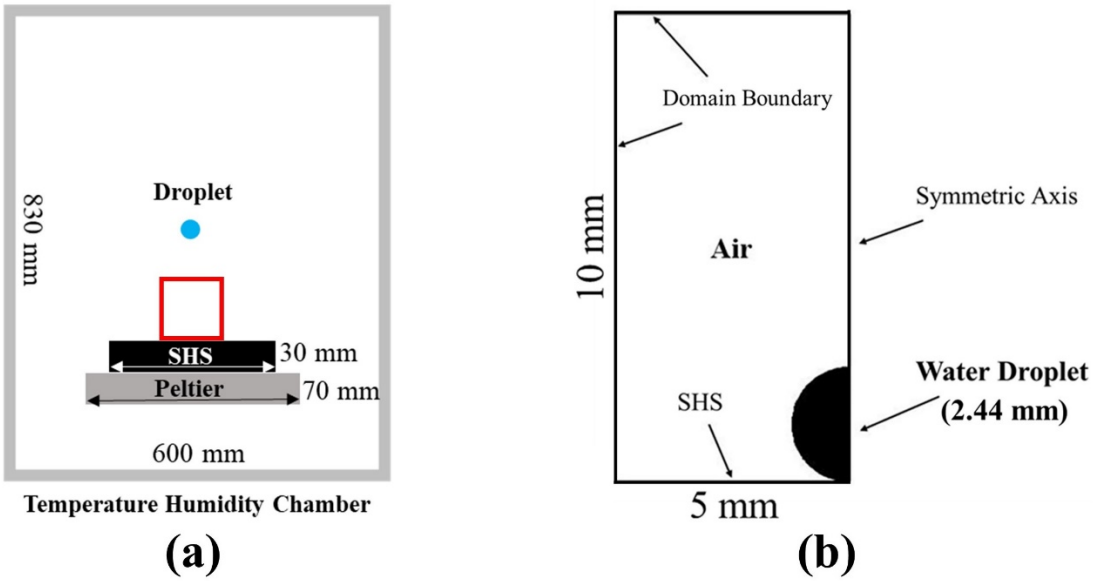

Figure 5.4 Comparison between the dimensions of experimental setup and 2D axisymmetric computational domain. (a) Experimental setup, (b) 2D axisymmetric computational domain. The red frame marks the considered computational region of the experimental setup.

5.2.3. Grid independence and meshing

In this work, as shown in Figure 5.5, throughout the computational domain, the uniform square meshing with the dimension of 0.02 × 0.02 mm is employed, producing 125000 elements. Grid independence study is carried out as shown in Figure 5.6. Four different mesh sizes are utilized with the cell per diameter (CPD) ranging from 50 to 150. CPD is defined as the ratio of the diameter of the impact droplet (2.44 mm) over the side length of the square computational cell. The mesh independent study is executed under the condition that water droplet temperature is 278 K and SHS temperature is 268 K. Contact length during the spreading and recoiling process of the impact droplet is adopted as the performance parameter to evaluate the meshing independency. The results showed that when CPD was more than 100, there was a minor change in droplet-SHS contact length during droplet impact. In this work, CPD 122 (uniform square mesh dimension 0.02 × 0.02 mm) is selected.

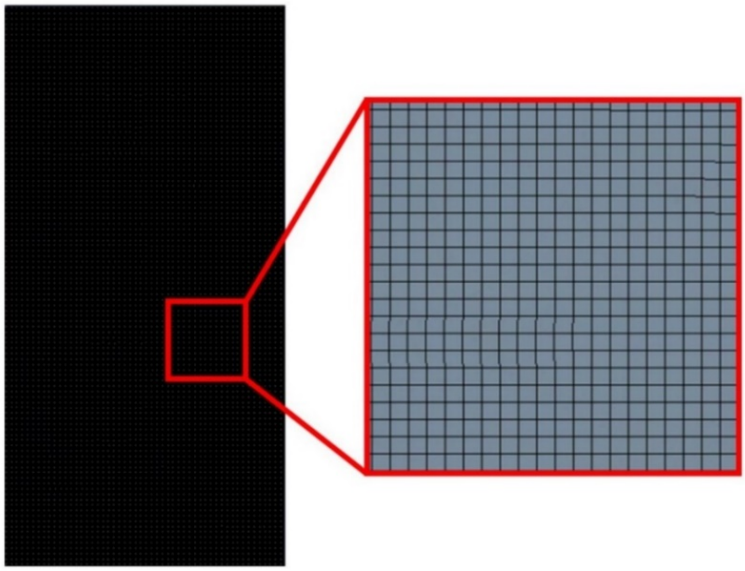

Figure 5.5 The uniform square mesh with the dimension of 0.02 × 0.02 mm throughout the computational domain.

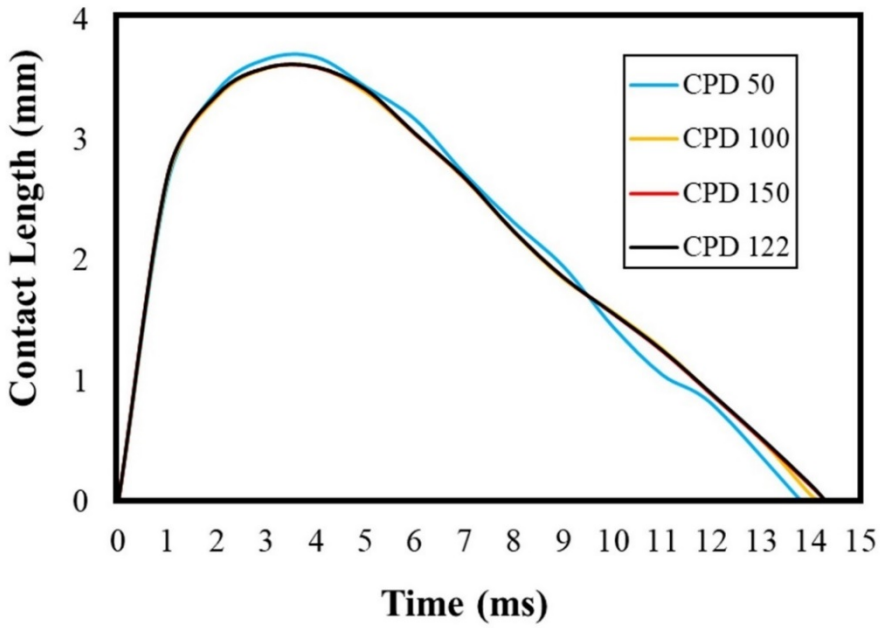

Figure 5.6 Grid independent study result when different cell per diameter (CPD) numbers were employed.

5.2.4. Fluid properties

For the CFD simulation work, the temperature range of water and air is within 248 K to 278 K. For the material properties of water and air utilized in this work, Table 5.1 compares the changes in density, viscosity, surface tension coefficient, specific heat, and thermal conductivity when temperature changes between 248 K and 278 K. For the viscosity of water, when the temperature reduces from 278 K to 248 K, there is an increase of 312.5 %. Therefore, water viscosity is adopted as a function of temperature as illustrated in Equation 5.15. For the surface tension coefficient of water in air, though there is a change of merely 6.1 %, this value is adopted as a function of water temperature as shown in Equation 5.14 in that surface tension plays a significant role in droplet bouncing phenomenon on an SHS. For other material properties, constant values at 278 K (initial temperature condition) are adopted throughout the simulation as listed in Table 5.1.

Table 5.1 Material properties of water and air at temperature 278 K and 248 K, and the deviations.

Water			
Physical Properties	278 K	248 K	Deviation (%)
Density, ρ_{w}	998.0 kg m^3	989.5 kg m^3	1.0
Viscosity [124], μ_{w}	$1.52e^{-3}$ N s m^{-2}	$6.27e^{-3}$ N s m^{-2}	312.5
Surface tension coefficient [165], γ	$7.49e^{-2}$ N m^{-1}	$7.93e^{-2}$ N m^{-1}	6.1
Specific heat, $c_{p\mathrm{w}}$	4.21 kJ kg^{-1} K^{-1}	4.45 kJ kg^{-1} K^{-1}	5.7
Thermal conductivity, λ_{w}	$5.67e^{-2}$ W m^{-1} K^{-1}	$5.28e^{-2}$ W m^{-1} K^{-1}	6.9
Air			
Physical Properties	278 K	248 K	Deviation (%)
Density, ρ_{a}	1.268 kg m^3	1.402 kg m^3	9.6
Viscosity, μ_{a}	$1.74e^{-5}$ N s m^{-2}	$1.59e^{-5}$ N s m^{-2}	8.6
Specific heat, $c_{p\mathrm{a}}$	1.005 kJ kg^{-1} K^{-1}	1.005 kJ kg^{-1} K^{-1}	0
Thermal conductivity, λ_{a}	$2.4e^{-2}$ W m^{-1} K^{-1}	$2.2e^{-2}$ W m^{-1} K^{-1}	8.3

5.2.5. Solver

ANSYS Fluent 2020 R1 [162] is employed to solve the droplet impact dynamics on SHS. This work employs computational schemes based on several related studies [104–107]. The computational schemes contain geo-reconstruction scheme for volume fraction discretization, least squares cell-based scheme for gradient, second-order upwind scheme for momentum and energy conservation, pressure staggering option (PRESTO!) scheme for pressure interpolation, splitting of operators (PISO) algorithm for pressure-velocity coupling, and explicit and first-order temporal integration scheme for transient flow. During the computation, approximate 250000 iterations of time step at 10^{-5} s is adopted to calculate the droplet impinging behaviors from initial contact to 50 ms. The Courant number throughout the computation is less than 0.1.

5.3. Validation of simulation results with experimental results

In this work, to verify the numerical modeling, experimental results of water droplet impact behaviors on SHS are compared with numerical outcomes regarding the droplet spreading and recoiling dynamics, droplet-SHS contact time, and droplet rebounding height under different temperature conditions in Chapter 5.3.1. Chapter 5.3.2 compares the viscous loss in experiments and simulations and validate the energy loss analysis in Chapter 4.4.

5.3.1. Comparison of droplet impacting behaviors in experiments and simulations

The droplet size and initial velocity are selected as $D = D_{\mathrm{M}} = 2.44$ mm and $v = 0.57$ m s^{-1}, respectively. Initial water droplet temperature and ambient air temperature are chosen as 278 K. For the values of contact angles, the advancing contact angle $\theta_{\mathrm{a}} = 161.4$ ° and the measured contact angle during droplet recoil $\overline{\theta_{\mathrm{c}}}$ (Figure 4.4a) are utilized when droplet spreads and recoils, respectively. Surface tension coefficient of water γ and water viscosity μ were correlated with temperature of water as shown in Equation 5.14

and 5.15, respectively. Table 5.2 summarizes the parameters used in experiments and simulations.

Figure 5.7 displays the temporal evolution of droplet shapes of both experiments and simulations. When the SHS temperature T_s was controlled at 278 K, as shown in Figure 5.7a, the impact water droplet reached maximum spreading at around 4 ms in both experiment and simulation. Then the droplet started recoiling on SHS and became fully rebounded from SHS at 14.5 ms for experiment and at 14.1 ms for simulation. In Figure 5.7b, when T_s = 268 K the droplet spreading, and recoiling dynamics was similar to T_s = 278 K. In Figure 5.7c, at T_s = 258 K the impact droplet remained longer time on SHS in both experiment (18.75 ms) and simulation (15.2 ms), but both droplets completely bounced off from SHS. When SHS temperature was reduced to 248 K, the impact droplet still spread to its maximum on SHS at around 4 ms, while during droplet recoiling, the impact droplet got adhered to SHS without rebounding (Figure 5.7d).

To further demonstrate the droplet spreading and recoiling dynamics when SHS temperature changes, in Figure 5.8, the contact lengths of impact droplet on SHS at different SHS temperatures are plotted to compare the droplet spreading and recoiling dynamics. The contact line dynamics in Figure 5.8 demonstrates that the droplet spreading and recoiling behaviors via current modellings agree well with the droplet impinging behaviors on SHS with different temperatures measured in experiments.

In addition, when the SHS temperature T_s was reduced from 278 K to 248 K, Figure 5.9 and Figure 5.10 display the contact time t_c and rebounding height H_r of an impact water droplet on SHS, respectively, and compare the numerical results with experimental data (Figure 3.6). For contact time in Figure 5.9, the average deviation between measured experimental values and the calculated numerical values is 6.5 %. For rebounding height in Figure 5.10, the average deviation between measured experimental values and the calculated numerical values is 5.9 %. In both experiments and simulations, when SHS temperature was decreased from 278 K to 248 K, the impact water droplet tended to stay longer on SHS and forfeited its rebounding capability (the contact time was infinite) when T_s was at 248 K. Meanwhile, there was a decrease in the rebounding height as SHS temperature was reduced from 278 K to 248 K.

Table 5.2 Summary of parameters in experiments and CFD simulations employed for verification of numerical modeling.

Parameter	Experiment	Simulation
Droplet size, D	2.44 ± 0.01 mm	2.44 mm
Droplet velocity, v	–	$\sqrt{2H_0/g} = 0.57$ m s^{-1}
Initial height, H_0	16.4 mm	–
Contact angles, θ	Measured θ_a & $\overline{\theta_c}$ through experiment	$\theta = \theta_a$ droplet spread $\theta = \overline{\theta_c}$ droplet recoil
Water droplet temperature, T_{wd}	278 ± 0.2 K	278 K
Ambient air temperature, T_a	278 ± 0.2 K	278 K
SHS temperature, T_s	278–248 ± 0.2 K	278–248 K

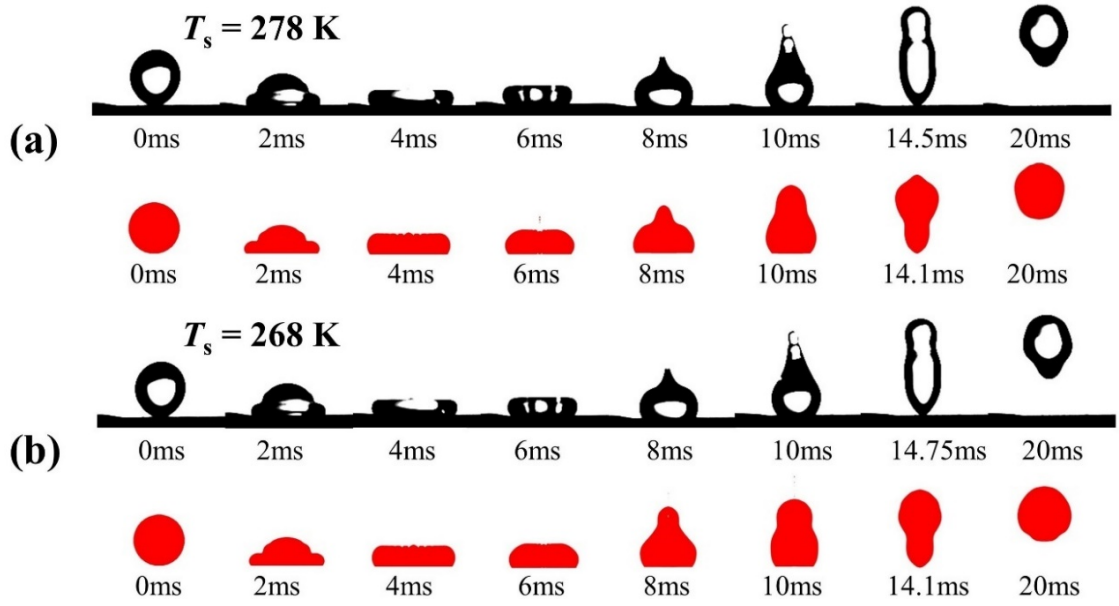

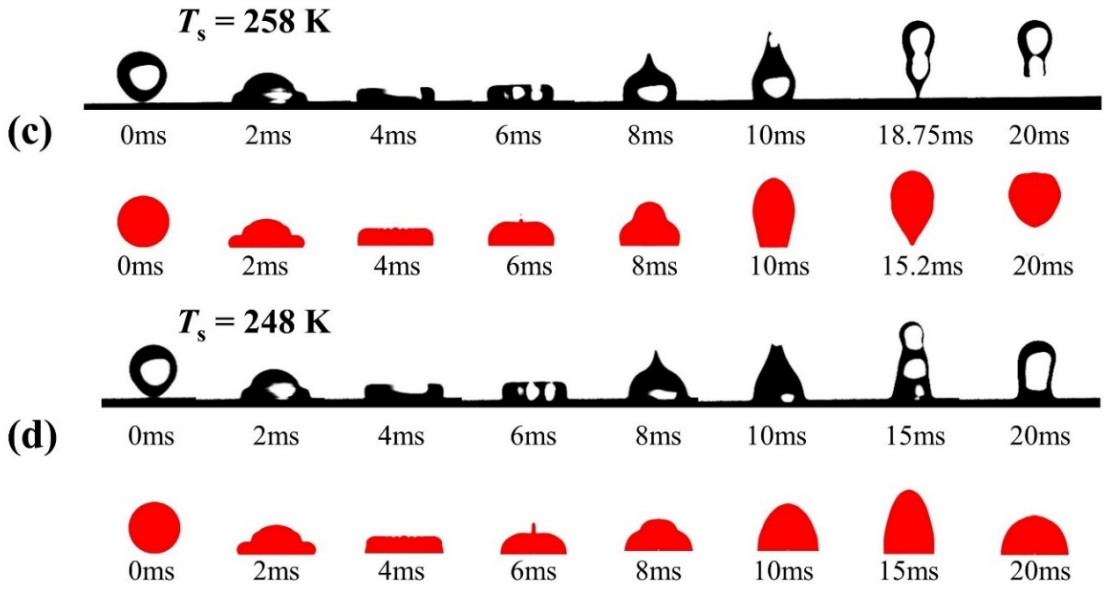

Figure 5.7 Comparison of spreading and recoiling behaviors of an impact water droplet with diameter D_M and temperature T_{wd} = 278 K on an SHS at T_s = 278–248 K in both experiments and simulations. (a) T_s = 278 K, (b) T_s = 268 K, (c) T_s = 258 K, and (d) T_s = 248 K.

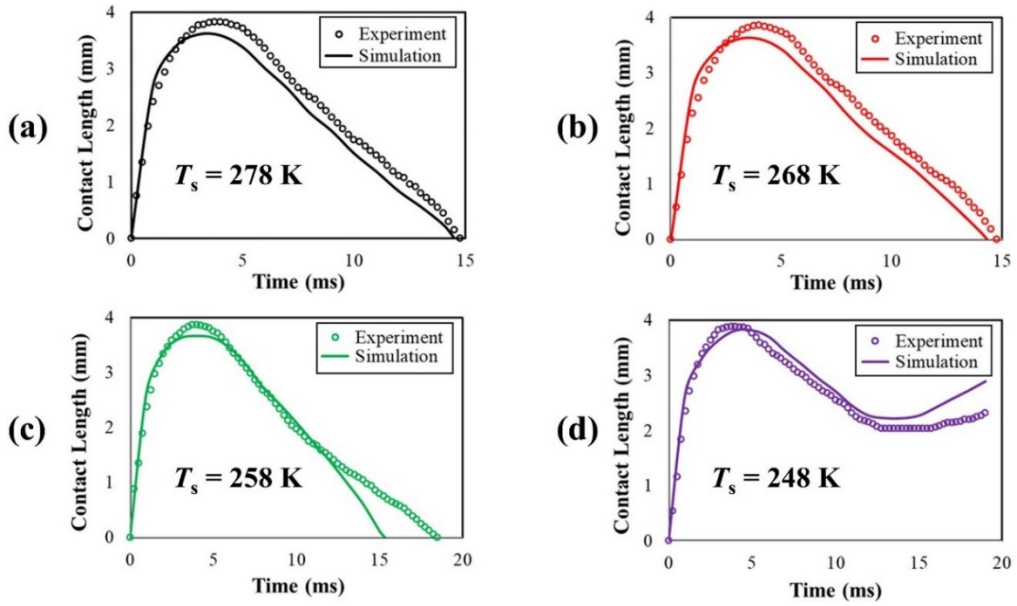

Figure 5.8 Comparison of the contact length of impact droplet D_M and temperature T_{wd} = 278 K impinging on an SHS at T_s = 278–248 K during the spreading and recoiling processes in experiments and simulations. (a) T_s = 278 K, (b) T_s = 268 K, (c) T_s = 258 K, and (d) T_s = 248 K.

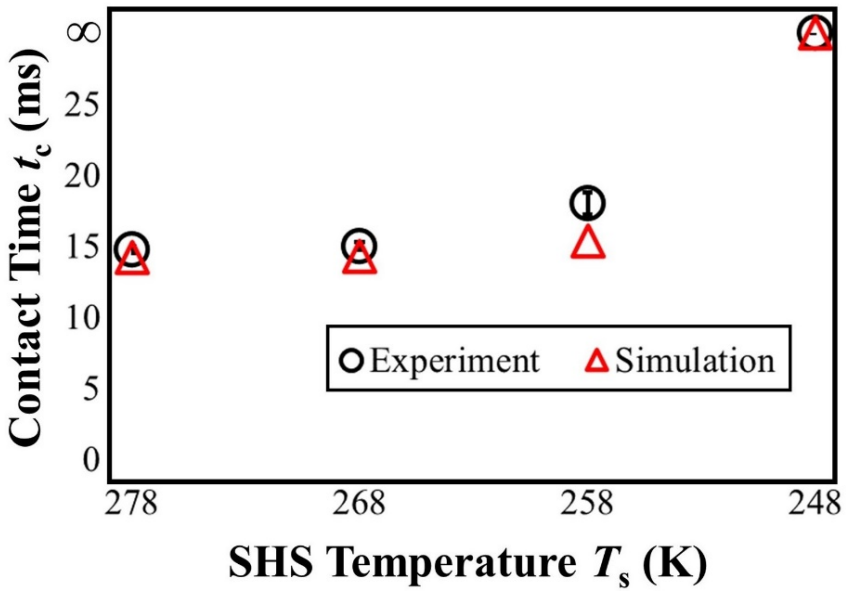

Figure 5.9 Contact time t_c of a water droplet with diameter D_M and temperature T_{wd} = 278 K impinging on an SHS at T_s = 278–248 K. For experiments, under each temperature condition, it was conducted three times at different positions of SHS.

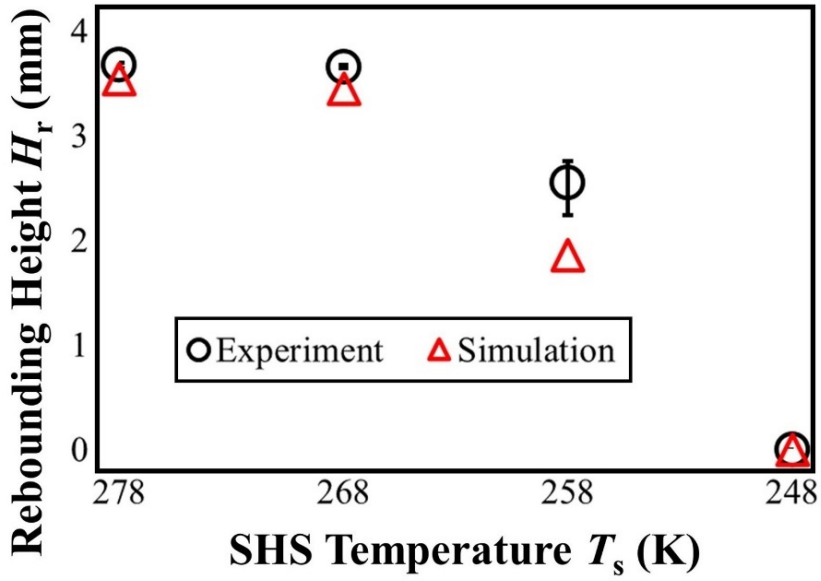

Figure 5.10 Rebounding height H_r of a water droplet with diameter D_M and temperature T_{wd} = 278 K impinging on an SHS at T_s = 278–248 K. For experiments, under each temperature condition, it was conducted three times at different positions of SHS.

5.3.2. Comparison of viscous loss in experiments and simulations

In Chapter 4.4, for rebounded water droplet, the modified Young-Dupré equation (Equation 4.4) based on the average contact angle during droplet recoiling $\overline{\theta_c}$ was employed to evaluate the energy loss due to adhesion E_a between droplet and SHS under different temperature conditions. Then the viscous loss E_μ was the balance between total energy loss and adhesion loss. To validate the energy loss analysis, this chapter calculates the viscous loss numerically under different experimental conditions. In simulation, the total viscous loss can be calculated through integrating the viscous dissipation function ϕ [177] over liquid domain from the moment of initial droplet contact with surface to the moment of maximum droplet rebounding t_{maxr},

$$E_\mu = \int_0^{t_{maxr}} \int_{V_{ld}} \phi dV dt \tag{5.18}$$

$$\phi = 2\mu\left(\left(\frac{\partial v_r}{\partial r}\right)^2 + \left(\frac{v_r}{r}\right)^2 + \left(\frac{\partial v_z}{\partial z}\right)^2\right) + \mu\left(\frac{\partial v_r}{\partial z} + \frac{\partial v_z}{\partial r}\right)^2 \tag{5.19}$$

where V_{ld} is the volume of the liquid computational domain. v_r and v_z represents the radial velocity and axial velocity under 2D cylindrical coordinate, respectively. In this work, under the cylindrical coordinate, viscous loss inside each computational cell is calculated. Then, the viscous loss of every millisecond $E_{\mu-\Delta t}$ ($\Delta t = 1$ ms) within the liquid domain is calculated, as follows,

$$E_{\mu-\Delta t} = \sum_{V_{ld}} \left[2\mu_{cell}\left(\left(\frac{\partial v_r}{\partial r}\right)^2 + \left(\frac{v_r}{r}\right)^2 + \left(\frac{\partial v_z}{\partial z}\right)^2\right) + \mu_{cell}\left(\frac{\partial v_r}{\partial z} + \frac{\partial v_z}{\partial r}\right)^2\right] V_{cell}\Delta t \tag{5.20}$$

where μ_{cell} represents the viscosity of the computational cell and V_{cell} represents the volume of the computational cell. After that, E_μ is calculated by integrating the viscous loss in liquid domain from the moment of initial droplet contact to the moment of maximum droplet rebounding, as follows,

$$E_{\mu} = \int_{0}^{t_{\mathrm{maxr}}} E_{\mu-\Delta \mathrm{t}} dt \tag{5.21}$$

$$= \sum_{t_{\mathrm{maxr}}} \sum_{V_{\mathrm{ld}}} \left[2\mu_{\mathrm{cell}} \left(\left(\frac{\partial v_{\mathrm{r}}}{\partial r} \right)^2 + \left(\frac{v_{\mathrm{r}}}{r} \right)^2 + \left(\frac{\partial v_{\mathrm{z}}}{\partial z} \right)^2 \right) + \mu_{\mathrm{cell}} \left(\frac{\partial v_r}{\partial z} + \frac{\partial v_{\mathrm{z}}}{\partial r} \right)^2 \right] V_{\mathrm{cell}} \Delta t$$

Figure 5.11 compares the calculation results of viscous loss E_{μ} of rebounding water droplet in experiment and simulation when the SHS temperature T_{s} is decreased from 278 K to 258 K, water droplet temperature T_{wd} is fixed at 278 K, and droplet diameter equals to D_{M}. In experiment, the viscous loss E_{μ} is calculated using Equation 4.1 to Equation 4.7, and the result is plotted in Figure 4.10. Figure 5.11 shows that the viscous loss calculated from simulations agree well with that in experiments, with a maximum deviation of 9.8 %. This validates the energy loss analysis executed in Chapter 4.4 and demonstrates that the current CFD modellings can reproduce the droplet impacting behaviors on an SHS near the freezing temperatures. For the time-course variation in viscous loss $E_{\mu-\Delta \mathrm{t}}$, it will be shown and discussed in Chapter 5.4.1.

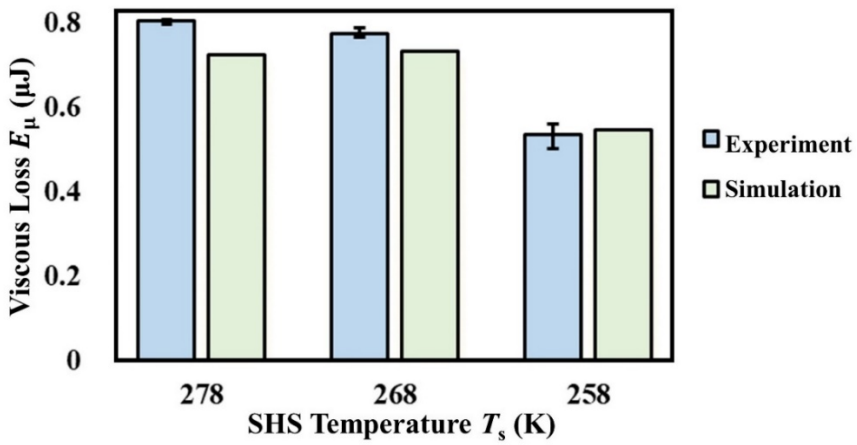

Figure 5.11 Comparison of viscous loss in experiments and simulations when impact water droplet successfully rebounds from the SHS as the surface temperature T_{s} reduces from 278 K to 258 K. For E_{μ} in experiment, it is calculated based on Equation 4.1 to Equation 4.7 and shown in Figure 4.10.

5.4. CFD simulation results and discussions

Chapter 5.4.1 exhibits and discusses the time-course viscous loss during the droplet spread, recoil, and rebound processes and elaborates the droplet impacting dynamics. Chapter 5.4.2 shows the results of parametric study and analyzes the dominant factor affecting droplet impacting behaviors on an SHS near freezing temperatures. Chapter 5.4.3 discusses some limitations when calculating the droplet impacting dynamics via the current modeling employed in this work.

5.4.1. Viscous loss analysis during droplet impacting process

In Chapter 5.3.2, the viscous loss calculated numerically has been demonstrated and compared with experimental results. In this chapter, the time-course viscous loss $E_{\mu-\Delta t}$ is shown when the impact water droplet becomes fully rebounded from the SHS. The water droplet temperature T_{wd} is 278 K, droplet size is D_M, and SHS temperature T_s varies from 278 K to 258 K. Figure 5.12 plots the viscous loss every millisecond $E_{\mu-\Delta t}$ from the moment of initial droplet contact with SHS to the moment of droplet maximum rebound. When T_s was controlled at 278 K and 268 K, the maximum droplet rebound happened at around 44 ms. For T_s equaled 258 K, the maximum droplet rebound took place at around 21 ms.

As shown in Figure 5.12, during droplet spreading from 0 ms to around 4 ms (Figure 5.7), the viscous loss $E_{\mu-\Delta t}$ showed the tendency to decrease due to the deceleration of the droplet with the conversion from kinetic energy to surface energy for all three SHS temperatures. After the droplet maximum spreading, droplet recoil initiated as shown in Figure 5.7. At the beginning of droplet recoil, because of the huge droplet deformation and the large curvature of deformed droplet, surface energy of droplet was large, resulting in the increase of the viscous loss $E_{\mu-\Delta t}$. Gradually, the kinetic energy transferred from droplet surface energy was reduced due to viscous loss and droplet-SHS adhesion. Thus, the kinetic energy inside the droplet decreased and the viscous loss demonstrated the trend to decrease for all three SHS temperatures. During the droplet

recoil and rebound processes, there were some fluctuations in viscous loss because of the droplet deformations.

Figure 5.13 shows the total viscous loss during droplet spread, recoil, and rebound. The droplet spreading process happened from 0 ms to around 4 ms for all three SHS temperatures. For SHS temperatures at 278 K and 268 K, viscous loss during droplet recoil process was calculated from 4 ms to 14 ms and viscous loss of droplet rebound process was evaluated from 14 ms to 44 ms. For SHS temperature at 258 K, the viscous loss in recoil and rebound was calculated from 4 ms to 15 ms and from 15 ms to 21 ms, respectively. When T_s was 278 K or 268 K, during droplet impact the wetting transition was not obvious (Figure 4.4a), therefore the viscous loss due to droplet-SHS adhesion was nearly the same (Figure 4.10) and the droplet had similar impinging behaviors (Figure 5.7). When T_s was reduced to 258 K, during droplet spread, the viscous loss was still close to higher SHS temperatures, because the effect of substrate was minor [58,148] and the maximum spreading area was similar (Table A.3). After maximum spread, the droplet recoiled more slowly (Figure 5.7) but still became fully rebounded from SHS. During this recoil process, the viscous loss was nearly equal to droplet impact on an SHS at higher temperatures. However, due to wetting transition (Figure 4.4a), more kinetic energy was loss due to droplet-SHS adhesion (Figure 4.10) when droplet recoiled. As a result, when droplet rebounded, less kinetic energy remained. This residual kinetic energy was further dissipated by the viscous loss during droplet rebound and droplet reached the maximum rebounding height. The less kinetic energy caused the droplet rebounding height decrease (Figure 5.10) as well.

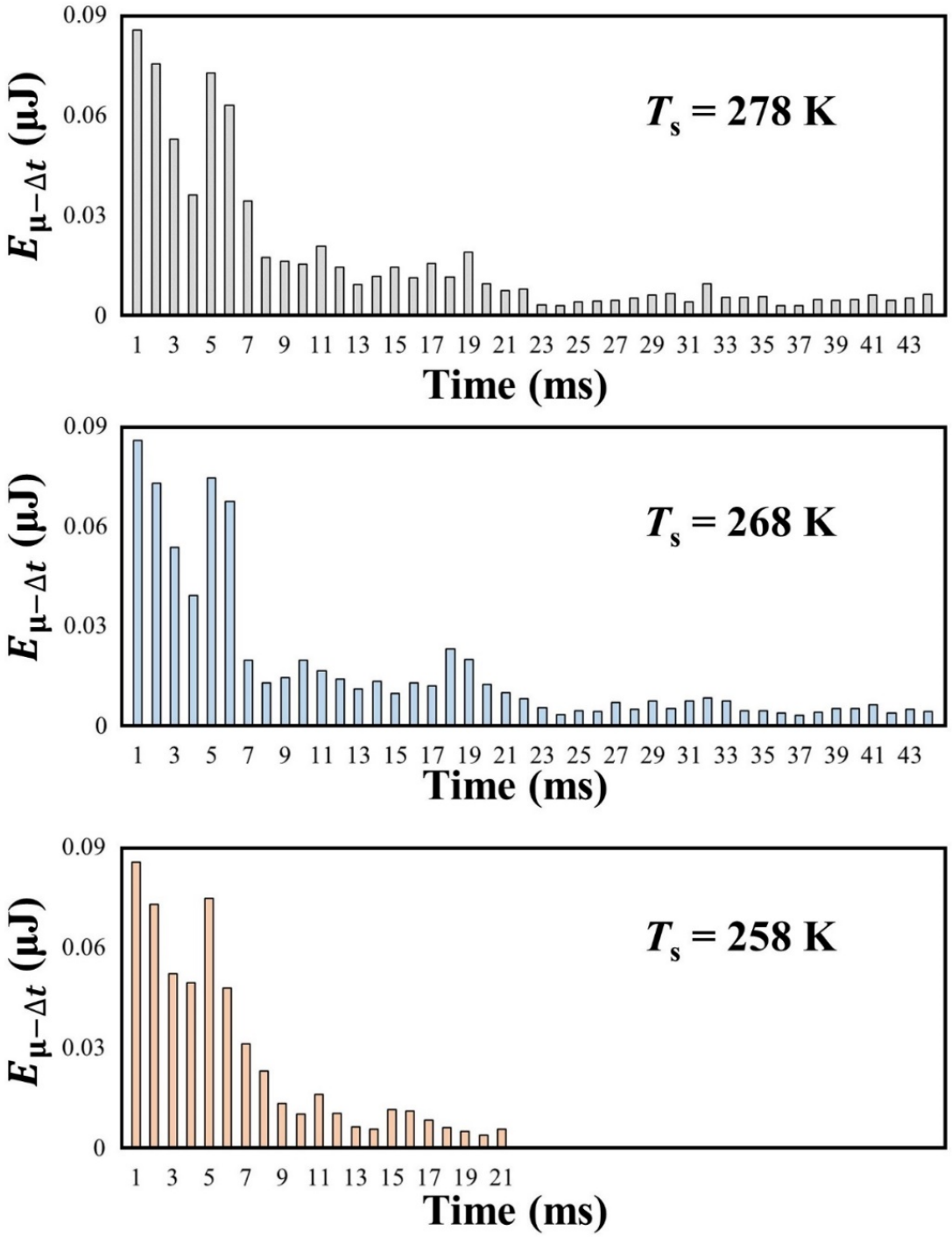

Figure 5.12 Viscous loss every millisecond $E_{\mu-\Delta t}$ from the moment of initial droplet contact with SHS to the moment of droplet maximum rebound of an impact water droplet with diameter D_M and temperature 278 K impacting on an SHS at three different surface temperatures T_s = 278 K, 268 K, and 258 K.

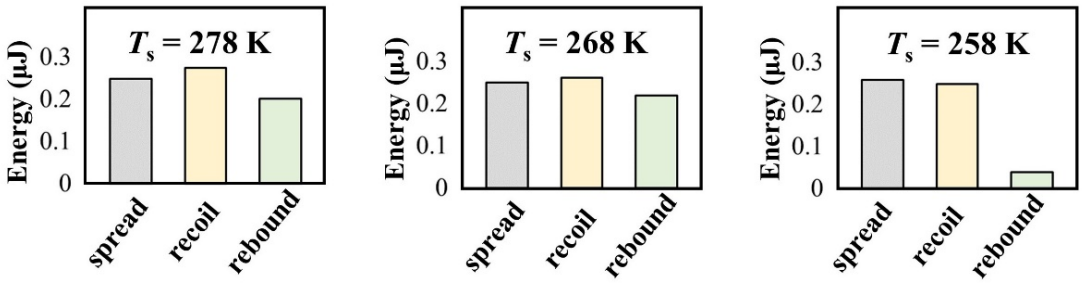

Figure 5.13 Viscous loss during the spread, recoil, and rebound process of an impact water droplet with diameter D_M and temperature 278 K impacting on an SHS at three different surface temperatures T_s = 278 K, 268 K, and 258 K.

Furthermore, taking T_s = 278 K as an example, Figure 5.14 displays the cross-sectional images of a water droplet during impacting processes and the velocity magnitude distribution of computational domain on the cross-sectional plane. During droplet spread (from 0 ms to around 4 ms), there was a rapid droplet deceleration, leading to a large velocity gradient, a high $E_{\mu-\Delta t}$ (Figure 5.12), and a great deal of viscous loss during droplet spread (nearly 35 % in Figure 5.13). After the droplet maximum spread on an SHS, droplet recoil started as the surface energy converted into kinetic energy. At the beginning of droplet recoil (e.g., 5 ms in Figure 14), due to large droplet deformation, droplet accelerated quickly so that the velocity gradient could be huge and there was a huge amount of viscous loss. Gradually, kinetic energy was dissipated due to droplet viscosity, meanwhile part of kinetic energy was lost because of droplet-SHS adhesion. This caused the velocity decrement inside the water droplet (e.g., 16 ms in Figure 5.14). Thus, there was an apparent decrease in $E_{\mu-\Delta t}$ at the later stage of droplet recoiling as depicted in Figure 5.12. Although $E_{\mu-\Delta t}$ during droplet spread was averagely larger than that during droplet recoil, the droplet recoil took a longer period so that the total viscous loss during droplet recoil (Figure 5.13) was around 35 % as well. After the impact water droplet became completely rebounded from the SHS, less kinetic energy remained, and the droplet velocity tremendously decreased compared with droplet spread and recoil processes as shown in Figure 5.14. Velocity gradient would become much smaller and the viscous loss $E_{\mu-\Delta t}$ showed a clear tendency to decrease (Figure 5.12).

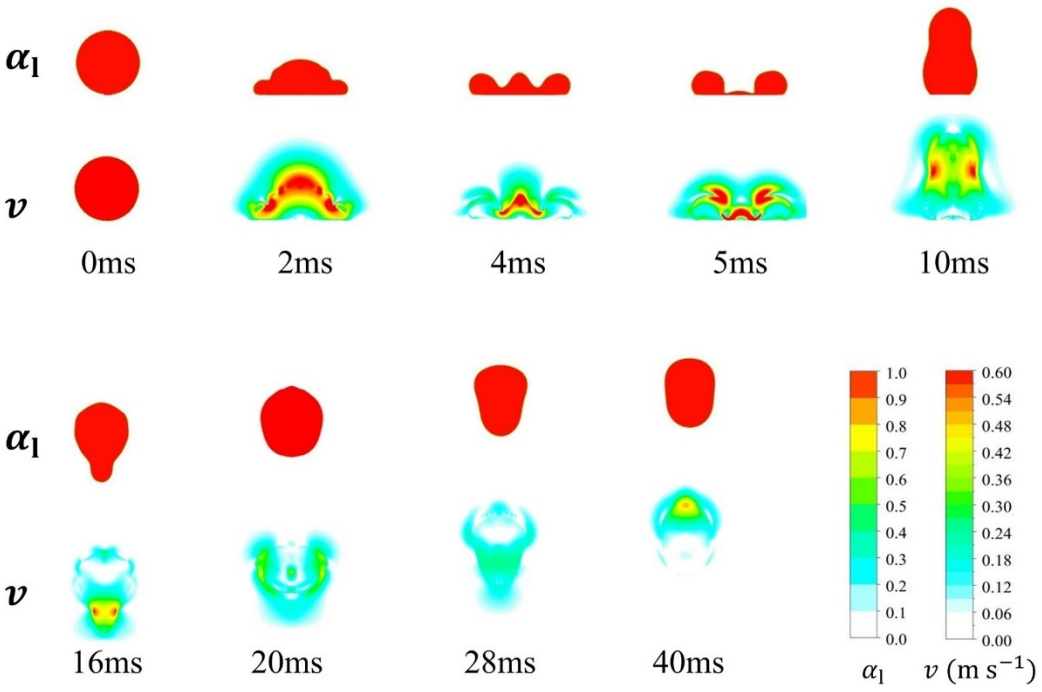

Figure 5.14 Cross-sectional images (liquid volume fraction α_l) of impact water droplet during spread, recoil, and rebound processes, and the velocity magnitude distribution (v) of the computational domain at the cross-sectional plane when both T_s and T_{wd} are equaled to 278 K.

5.4.2. Parametric study on dominant factor determining droplet rebound behaviors on SHS near freezing temperatures

In this work, to further analyze the dominant factor determining droplet rebounding or sticking performance on SHS near freezing temperatures, parametric studies are carried out. Three major parameters are considered including the wetting transition (receding contact angle), water viscosity, and surface tension coefficient. Table 5.3 lists the simulation conditions and material properties of parametric study in this work. In this chapter, the physics of droplet rebounding or sticking mechanisms affected by these three factors is analyzed as well. Non-wetting condition (θ_r = 180°) is adopted to evaluate the maximum viscous loss of an impact water droplet on a surface during droplet spread, recoil, and rebound processes. Considering maximum viscous loss and maximum adhesion loss, droplet rebound performance can be predicted. Then the parametric study

results are utilized to analyze the dominant factor and underlying physics affecting droplet impacting dynamics on an SHS near freezing temperatures.

Table 5.3 Simulation conditions and material properties of parametric study in this CFD numerical work.

Droplet Size, D	2.44 mm
Droplet velocity, v	0.57 m s^{-1}
Advancing contact angles, θ_a	160°
Receding contact angles, θ_r	80°–180°
Water droplet temperature, T_{wd}	278 K
Ambient air temperature, T_a	278 K
SHS temperature, T_s	278 K
Water viscosity, μ_w	$9.9e^{-4}$–$6.27e^{-3}$ N s m^{-2}
Surface tension coefficient, γ	$7.28e^{-2}$–$7.93e^{-2}$ N m^{-1}

5.4.2.1. Effect of receding contact angle on droplet impact behaviors

Figure 5.15 shows the droplet spreading and recoiling processes on a surface as the receding contact angle θ_r decreases from 180° to 80°. Water viscosity μ_w and surface tension coefficient of water were taken as $1.52e^{-3}$ N s m^{-2} and $7.49e^{-2}$ N m^{-1}, respectively. Other numerical conditions were selected as shown in Table 5.3. As shown in Figure 5.15, for receding contact angle 180°, the droplet reached maximum spreading at 4 ms, after which the droplet recoil process started. At 11.9 ms, the droplet became fully rebound from the surface. When θ_r was decreased to 160°, the impact droplet remained longer time on the surface and bounced off from the surface at 12.6 ms. As the receding contact angle decreased to 140° and 120°, the contact time increased to 14.3 ms and 16.5 ms, respectively. When θ_r was equaled to 100°and 80°, the impact water droplet got adhered to the surface without rebounding.

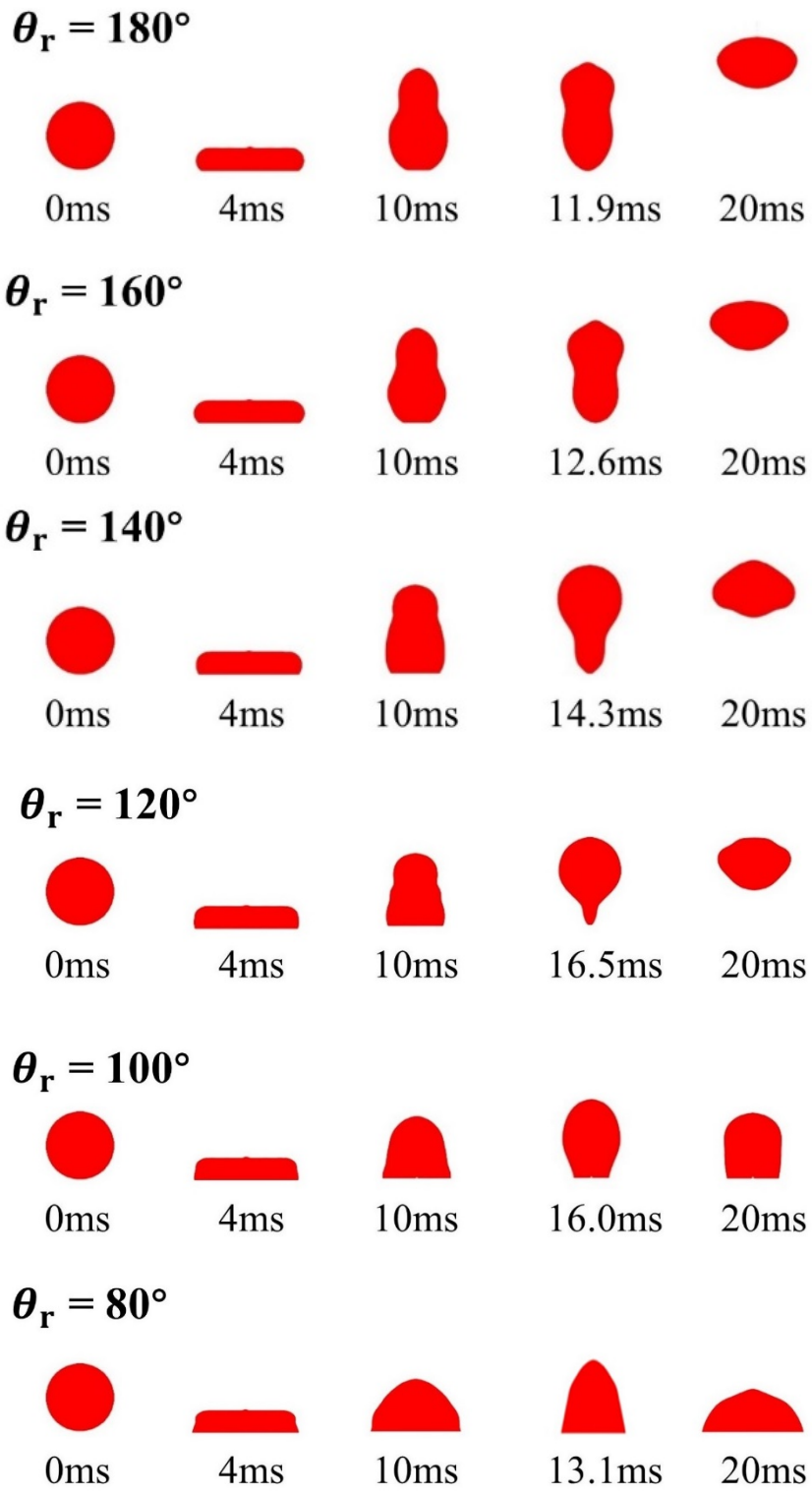

Figure 5.15 The spreading and receding process of an impact water droplet on a surface as the receding contact angle θ_r decreases from 180° to 80°.

Figure 5.16 summarizes the contact time t_c and rebounding height H_r when the receding contact angle is decreased from 180° to 80°. With the decrease of θ_r, the impact water droplet remained longer time on the surface and bounced off to a lower height. Finally, the impact water droplet forfeited its capability to rebound when θ_r was less than 100°.

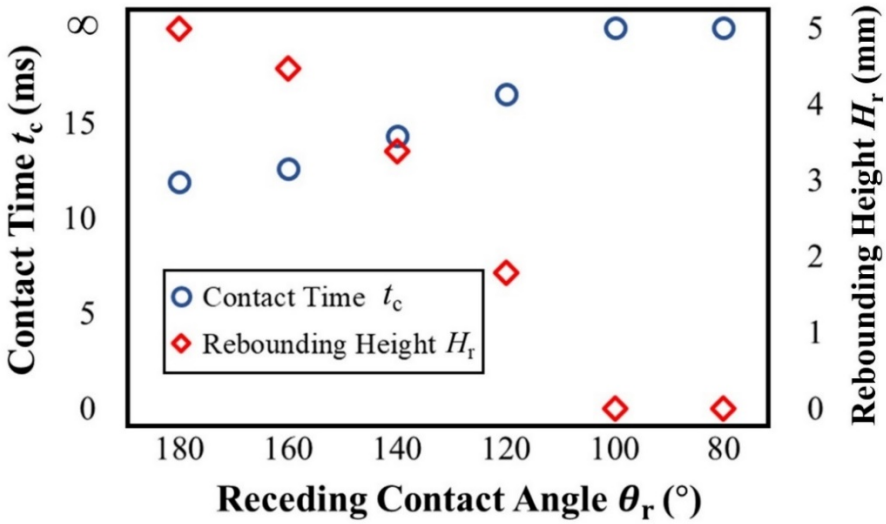

Figure 5.16 The contact time t_c and rebounding height H_r of an impact water droplet on a surface as the receding contact angle θ_r decreases from 180° to 80°.

In this work, the viscous loss E_μ and adhesion loss E_a during the spreading and recoiling process of an impact water droplet on the surface as the receding contact angle is decreased from 180° to 80° is calculated. For viscous loss E_μ, it is calculated as the integration of viscous dissipation function (Equation 5.19) over the liquid domain during the contact time t_c when θ_r is larger than 120°. When droplet becomes adhered to the surface (θ_r is 100° and 80°), the time period is chosen from initial droplet contact to droplet minimum contact with the surface. For energy loss due to droplet-surface adhesion, work of adhesion based on modified Young-Dupré equation (Equation 4.3) was adopted. Then for a droplet impact on a surface, based on maximum contact length d_{max} and minimum contact length d_{min} (Table A.4), the energy loss due to droplet-surface adhesion E_a can be calculated as,

$$E_a = (\pi/4)(d_{max}^2 - d_{min}^2)\gamma(1 + \cos\theta_r) \quad (5.22)$$

Figure 5.17 shows that calculation results. During the droplet spread and recoil process, the total viscous loss remained nearly the same when the receding contact angle θ_r decreased. When θ_r was 180°, there was no adhesion between droplet and surface and all the initial potential energy was dissipated due to water viscosity. For smaller receding contact angle, the adhesion loss E_a kept increasing, therefore, less kinetic energy was remained, and droplet rebounded to a lower height (Figure 5.16). For receding contact angle 100° and 80°, though droplet became stuck to the surface without rebounding, the summation of E_μ and E_a was less than the initial potential energy of droplet E_{p0}. This was because at the moment of droplet minimum contact with surface there was still some kinetic energy remained inside the water droplet and the potential energy of the droplet increased.

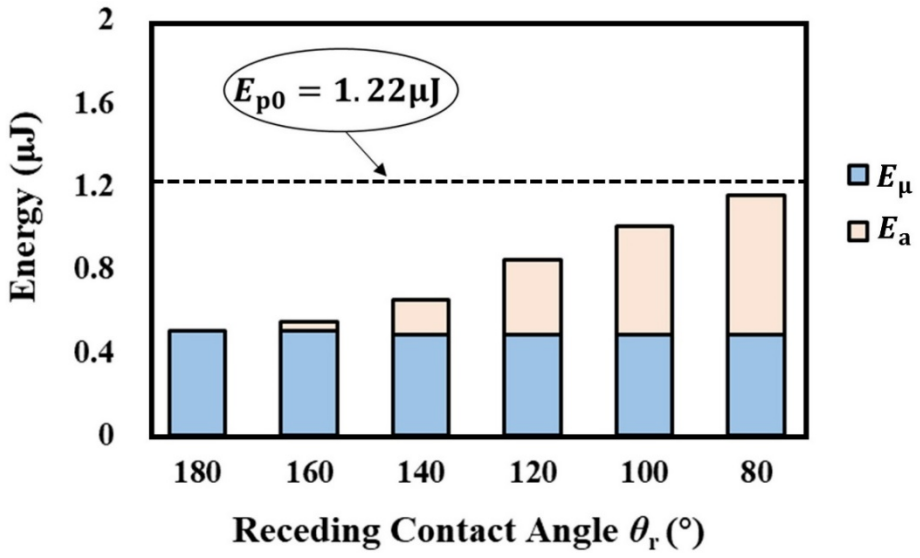

Figure 5.17 Viscous loss E_μ and adhesion loss E_a of an impact water droplet on a surface as the receding contact angle θ_r decreases from 180° to 80°.

Furthermore, this work comes up with an approach to predict droplet rebounding or sticking performance on a surface through employing θ_r = 180° to evaluate the maximum viscous loss of an impact water droplet on a surface. The viscous loss during droplet spreading process was similar (Figure 5.17), when θ_r = 180° droplet rebounded the highest (Figure 5.16) and the viscous loss during droplet recoil and rebound was at maximum. Assuming that the surface energy of droplet at the initial state of impact was

the same as the surface energy at the final state, the energy loss could be calculated as the difference between potential energy at the initial state and potential energy at the final state. For an impact water droplet on a surface, maximum value for energy loss due to viscosity $E_{\mu-\max}$ can be expressed as,

$$E_{\mu-\max} = E_{p0} - E_{pr} = mg(H_0 - H_r) \quad \text{when } \theta_r = 180° \tag{5.23}$$

Then for a droplet impact on a surface, the maximum value of energy loss of droplet-surface adhesion can be calculated as,

$$E_{a-\max} = (\pi/4)d_{\max}^2\gamma(1 + \cos\theta_r) \tag{5.24}$$

Figure 5.18 shows the calculation results when the receding contact angle θ_r was reduced from 180° to 80°. With a decrease in θ_r, it took the impact water droplet more energy for the adhesion loss during droplet impact. When θ_r was larger than 120°, the initial potential energy of the impact droplet was sufficient for energy losses due to droplet-surface adhesion and droplet viscosity, so the impact droplet was capable of fully rebounding from surface. When θ_r reduced to 100° or 80°, E_{p0} was smaller than the summation of $E_{\mu-\max}$ and $E_{a-\max}$, and the impact droplet became stuck to the surface without bouncing.

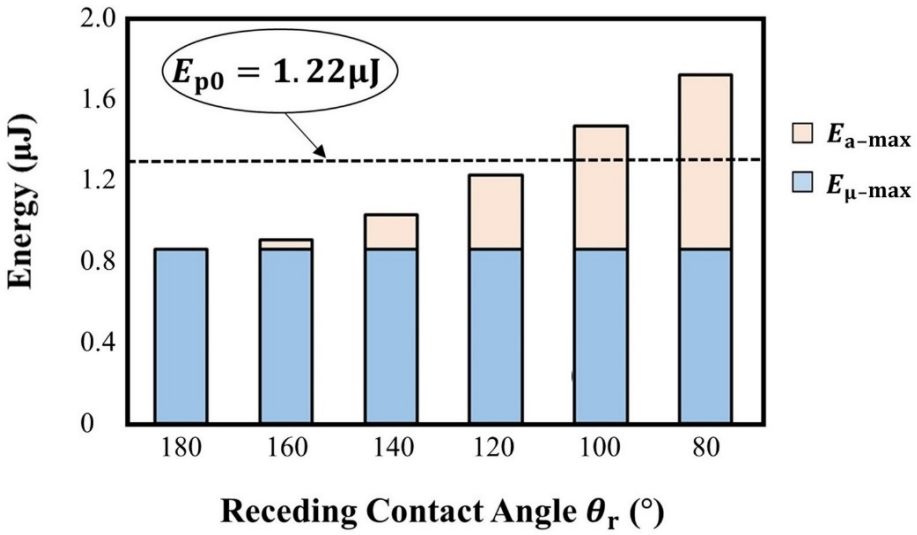

Figure 5.18 Energy loss analysis for an impact water droplet on a surface as the receding contact angle decreases from 180° to 80°. The dash line represents the initial potential energy of the impact water droplet E_{p0} = 1.22 μJ.

In addition, the maximum viscous loss $E_{\mu-\max}$ calculated from Equation 5.23 can further validate the energy loss analysis shown in Chapter 4.4. Because in Figure 4.10, when T_s and T_{wd} both equaled to 278 K, the receding contact angle of a D_M sessile water droplet on SHS was 155.2° (as shown in Table 3.1), demonstrating the great super-hydrophobicity of the surface. Therefore, under this temperature condition droplet-SHS adhesion was minor and viscous loss E_μ was supposed to be close to $E_{\mu-\max}$. In the simulation $E_{\mu-\max}$ was 0.849 μJ, while in Chapter 4.4 the viscous loss E_μ calculated through balancing total viscous loss with adhesion loss was 0.804 μJ (T_s = 278 K in Figure 4.10).

To further analyze the droplet impacting dynamics affected by wetting transition, Figure 5.19 plots the change of surface force term $\boldsymbol{F_\gamma}$ in the momentum equation at the beginning of droplet recoil (4 ms) as θ_r is decreased from 160° to 80°. Meanwhile, this force in vertical direction $\boldsymbol{F_{\gamma v}}$ and in horizontal direction $\boldsymbol{F_{\gamma h}}$ are illustrated separately. The results showed that when θ_r was reduced from 160° to 120°, there was an obvious reduction in the surface force, particularly in vertical direction $\boldsymbol{F_{\gamma v}}$. This decrease in $\boldsymbol{F_{\gamma v}}$ led to the increase of contact time and the decrease of rebounding height. Previously, Antonini et al. [140] experimentally observed that a millimeter-sized water droplet only rebounded from surfaces with a receding contact angle larger than 100° for a wide range of impact velocities. In this parametric study, when θ_r equaled to 100° the impact droplet became adhered to the surface without rebounding, showing a good agreement with previous experimental work [140]. In Figure 5.19, when θ_r was 120° there was an obvious decrease in the surface force $\boldsymbol{F_\gamma}$, so the impact droplet stayed longer time on the surface and rebounded to a lower height. For θ_r = 100°, there was a significant decrease in the surface force $\boldsymbol{F_\gamma}$, particularly in vertical direction $\boldsymbol{F_{\gamma v}}$ to around 0. Thus, the impact water droplet lost the momentum to bounce off from the surface. As θ_r was reduced to 80°, the direction of $\boldsymbol{F_{\gamma v}}$ turned to downward, hence the impact water droplet became stuck to the surface more easily.

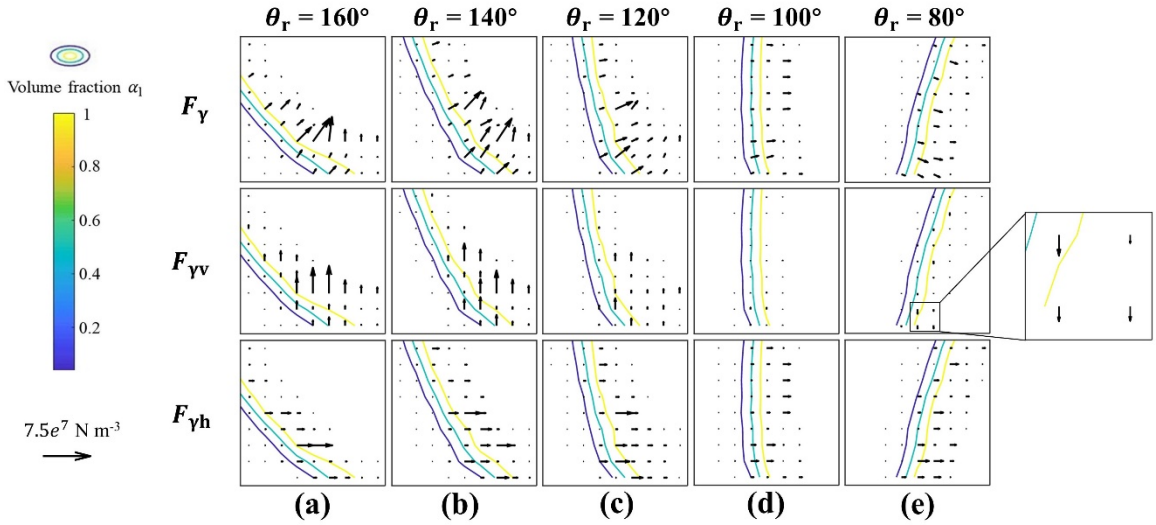

Figure 5.19 Plots of the surface force term $\boldsymbol{F_\gamma}$ in the momentum equation the surface force in vertical direction $\boldsymbol{F_{\gamma v}}$, and the surface force in horizontal direction $\boldsymbol{F_{\gamma h}}$ at the beginning of droplet recoil (4 ms) when θ_r is decreased from 160° to 80°.

5.4.2.2. Effect of viscosity on droplet impact behaviors

Figure 5.20 displays the droplet spreading and recoiling dynamics when the viscosity of water μ_w increases from $9.9e^{-4}$ N s m^{-2} to $6.27e^{-3}$ N s m^{-2}. Viscosity values $9.9e^{-4}$ N s m^{-2} and $6.27e^{-3}$ N s m^{-2} were selected based on Equation 5.15 when temperature equaled to 293 K and 248 K, respectively. Receding contact angle θ_r was selected as 140° and surface tension coefficient of water was taken as 7.49e^{-2} N m^{-1}. Figure 5.21 shows the changes of contact time t_c and rebounding height H_r. As the viscosity of water increased from $9.9e^{-4}$ N s m^{-2} to $6.27e^{-3}$ N s m^{-2}, there was a minor change in the droplet-SHS contact time but a clear decrease in droplet rebounding height. Previously, Bertolo et al. [160] experimentally presented that based on the Ohnesorge number (Oh) there were two regimes for the contact time of an impact droplet on an SHS: capillary-inertial regime ($Oh < 5e^{-2}$) to capillary-viscous regime ($Oh > 5e^{-2}$). Ohnesorge number is defined as the ratio of viscous forces over inertial and capillary forces, mathematically expressed as, $Oh = \mu/\sqrt{\rho\gamma D}$. In the current numerical work, Ohnesorge number was within the range of $1.5e^{-3} - 9e^{-3}$, which belonged to the

capillary-inertial regime. Therefore, contact time t_c was irrelevant to viscosity of water and remained nearly the same within the water viscosity range of $9.9e^{-4}$–$6.27e^{-3}$ N s m^{-2}.

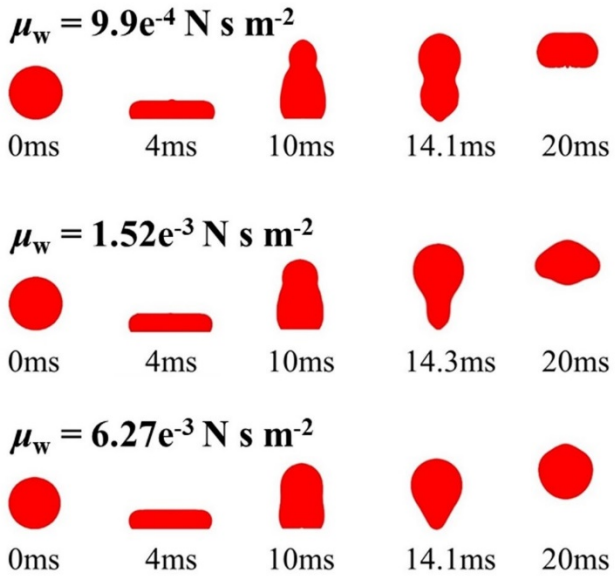

Figure 5.20 The spreading and receding process of an impact water droplet on a surface as the viscosity of water μ_w increases from $9.9e^{-4}$ N s m^{-2} to $6.27e^{-3}$ N s m^{-2}.

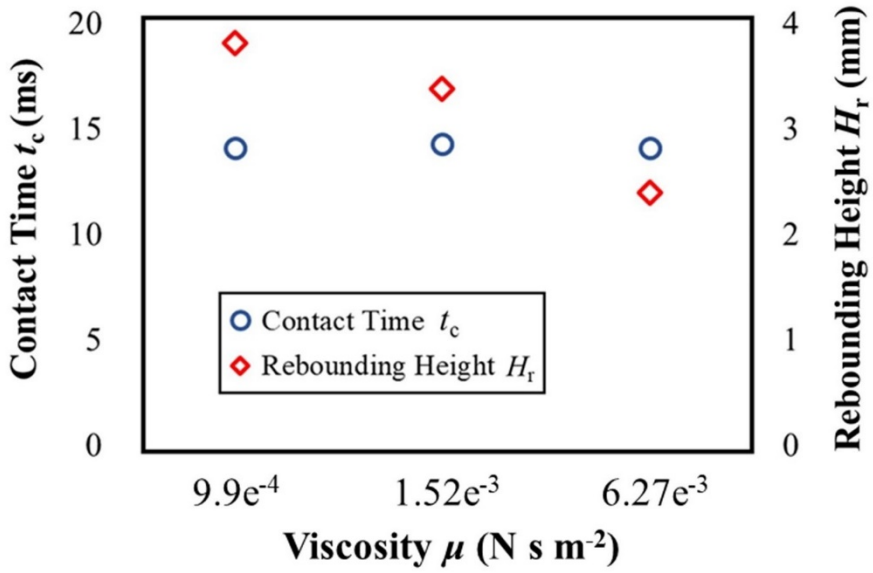

Figure 5.21 The contact time t_c and rebounding height H_r of an impact water droplet on a surface as the viscosity of water μ_w increases from $9.9e^{-4}$ N s m^{-2} to $6.27e^{-3}$ N s m^{-2}.

Figure 5.22 shows the energy analysis in consideration of the maximum energy loss due to viscosity $E_{\mu-\max}$ (Equation 5.23) and maximum energy loss due to adhesion $E_{a-\max}$ (Equation 5.24). When the summation of $E_{\mu-\max}$ and $E_{a-\max}$ was less than E_{p0}, the impact droplet completely bounced off the surface. As the increase of water viscosity, there was an ignorable change in $E_{a-\max}$ but an obvious increase in $E_{\mu-\max}$. For the impact water droplet, there was an increase in the loss of kinetic energy owing to water viscosity during the droplet spreading and recoiling process. Therefore, less kinetic energy was remained, and the rebounding height of the impact water droplet decreased.

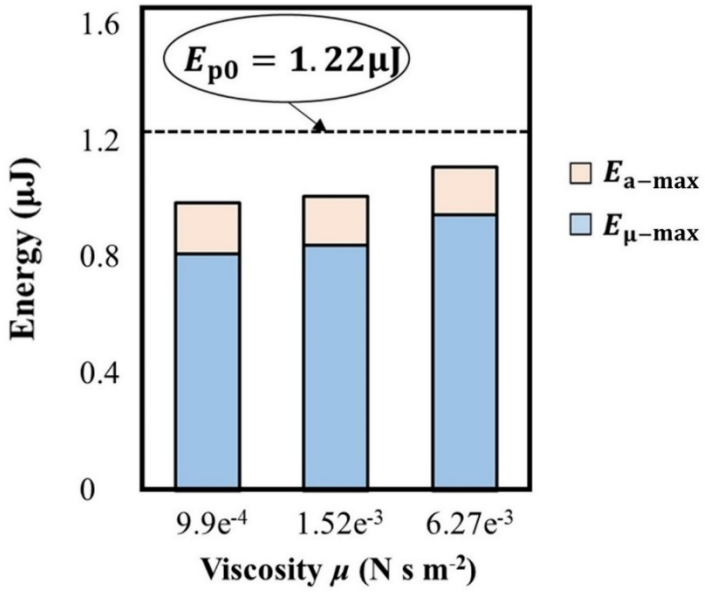

Figure 5.22 Energy loss analysis for an impact water droplet on a surface as the viscosity of water μ_w increases from $9.9e^{-4}$ N s m^{-2} to $6.27e^{-3}$ N s m^{-2}. The dash line represents the initial potential energy of the impact water droplet E_{p0} = 1.22 μJ.

5.4.2.3. Effect of surface tension coefficient on droplet impact behaviors

Figure 5.23 presents the droplet spreading and recoiling dynamics when the surface tension coefficient of water γ increases from $7.28e^{-2}$ N m^{-1} to $7.93e^{-2}$ N m^{-1}. The values $7.28e^{-2}$ N m^{-1} and $7.93e^{-2}$ N m^{-1} were selected based on Equation 5.14 when temperature equaled 293 K and 248 K, respectively. Receding contact angle θ_r was selected as 140° and water viscosity μ_w was taken as 1.52e^{-3} N s m^{-2}. Figure 5.24 shows

the changes of contact time t_c and rebounding height H_r. As the surface tension coefficient of water increased from $7.28e^{-2}$ N m^{-1} to $7.93e^{-2}$ N m^{-1}, there was a decrease in droplet-SHS contact time and an increase in droplet rebounding height.

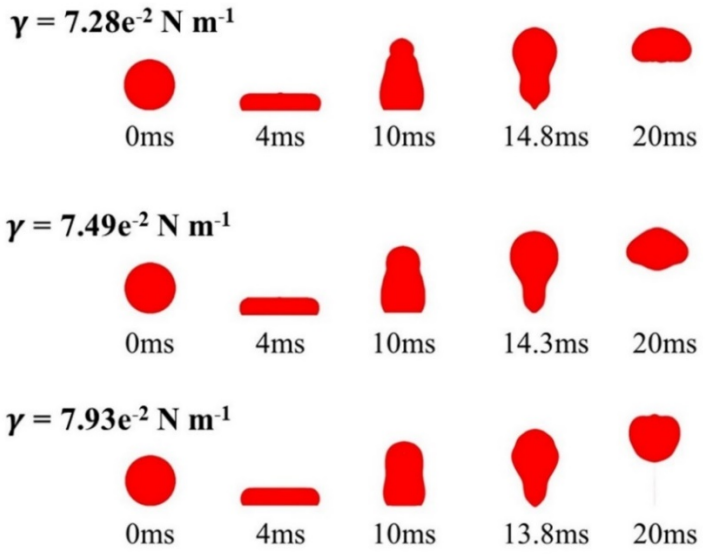

Figure 5.23 The spreading and receding process of an impact water droplet on a surface as the surface tension coefficient of water γ increases from $7.28e^{-2}$ N m^{-1} to $7.93e^{-2}$ N m^{-1}.

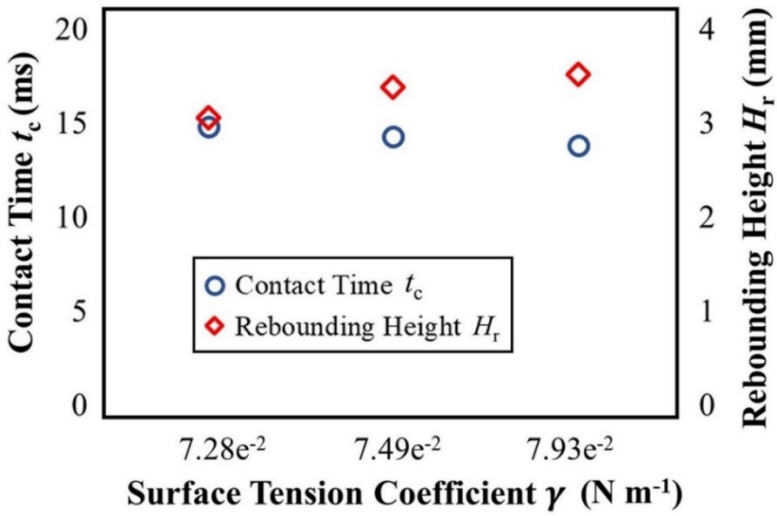

Figure 5.24 The contact time t_c and rebounding height H_r of an impact water droplet on a surface as the surface tension coefficient of water γ increases from $7.28e^{-2}$ N m^{-1} to $7.93e^{-2}$ N m^{-1}.

For the contact time t_c, it was a balance between droplet inertia and capillarity (Equation 3.2). Figure 5.25 compares the change of t_c, τ, and t_c/τ as γ increases from $7.28e^{-2}$ N m^{-1} to $7.93e^{-2}$ N m^{-1}. With the increase of γ, both t_c and τ decreased but the ratio kept nearly unchanged, demonstrating that contact time was balanced between inertia and capillarity.

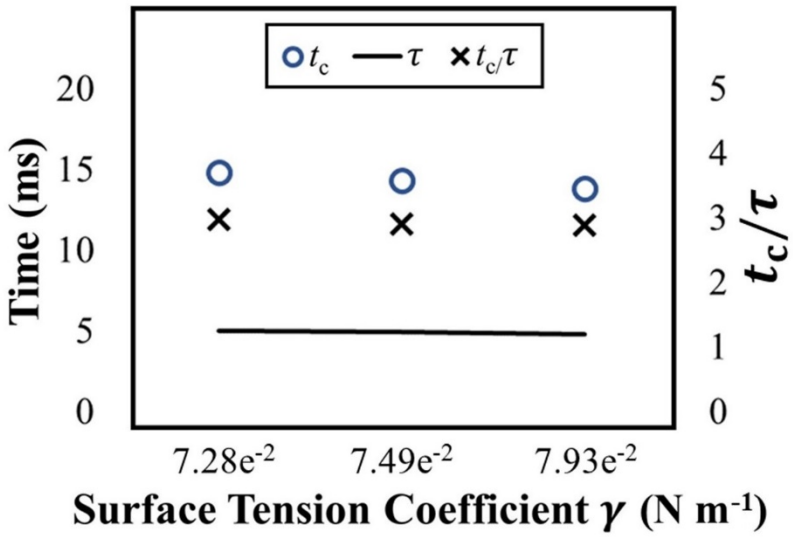

Figure 5.25 Comparison between droplet-SHS contact time t_c, characteristic contact time τ, and the ratio of t_c/τ when the surface tension coefficient of water γ increases from $7.28e^{-2}$ N m^{-1} to $7.93e^{-2}$ N m^{-1}.

For the change of rebounding height H_r, Figure 5.26 shows the results of energy analysis through Equation 5.23 and Equation 5.24. The droplet fully rebounded from the surface because the summation of $E_{\mu-max}$ and E_{a-max} was less than E_{p0}. With the increase of γ from $7.28e^{-2}$ N m^{-1} to $7.93e^{-2}$ N m^{-1}, the maximum energy loss of droplet-SHS adhesion E_{a-max} remained almost the same, but the maximum viscous loss $E_{\mu-max}$ showed a clear tendency to decrease. This was because when surface tension increased the maximum spreading on SHS was reduced as listed in Table 5.4. For the impact water droplet, owing to the decrease of $E_{\mu-max}$ more kinetic energy was remained, and the rebounding height of the impact water droplet increased.

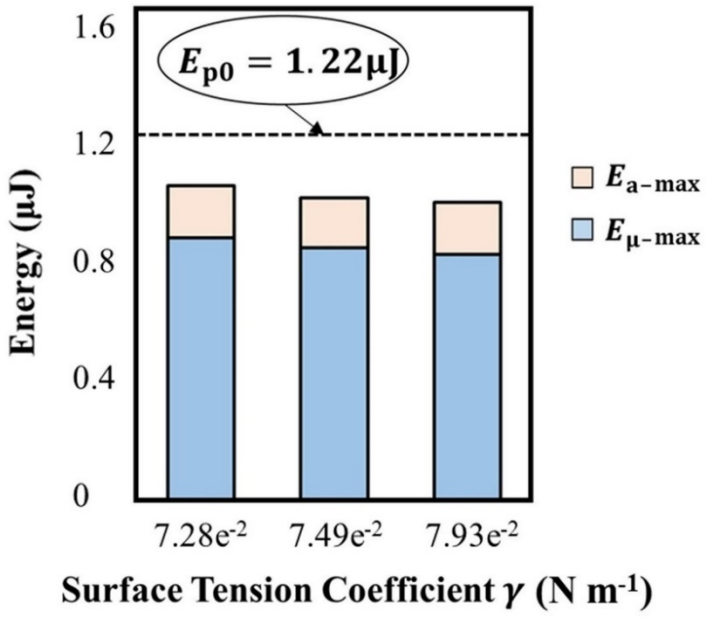

Figure 5.26 Energy loss analysis for an impact water droplet on a surface as the surface tension coefficient of water γ increases from $7.28e^{-2}$ N m^{-1} to $7.93e^{-2}$ N m^{-1}. The dash line represents the initial potential energy of the impact water droplet E_{p0} = 1.22 μJ.

Table 5.4 Maximum spreading of the impact water droplet on SHS when the surface tension coefficient γ changes.

Surface tension coefficient, γ (N m^{-1})	Maximum spreading on SHS, d_{max} (mm)
$7.28e^{-2}$	3.61
$7.49e^{-2}$	3.50
$7.93e^{-2}$	3.47

5.4.2.4 Summary of parametric study

In Chapter 5.4.2.1., as the occurrence of wetting transition (receding contact angle θ_r reduced from 160° to 80°), the impact water droplet showed the tendency to adhered to the surface with an increase in contact time and a decrease in rebounding height. This

was because the impact water droplet lost more kinetic energy owing to the adhesion increase between droplet and surface when wetting transition took place. Besides, the surface force especially in vertical direction decreased tremendously, resulting in the forfeit of rebounding capability of the impact water droplet. For the increase of droplet viscosity, as shown in Chapter 5.4.2.2., it had an ignorable influence on contact time but rebounding height displayed a clear reducing trend. Within capillary-inertia regime, the effect of droplet viscosity on contact time was minor. The decrease in rebounding height was due to the increase in viscous loss when droplet viscosity increased. In Chapter 5.4.2.3., the increase of surface tension coefficient showed a negative relation with contact time but a positive relation with rebounding height, in that contact time was a balance between inertia and capillarity, and the surface tension increase confined droplet spreading which reduced the viscous loss. For an impact water droplet on a surface, this work showed that summation of maximum viscous loss calculated via non-wetting condition and maximum adhesion loss evaluated via modified Young-Dupré equation can be compared with initial potential energy to predict droplet rebounding behaviors.

Figure 5.7 showed that when a water droplet impacted on an SHS near freezing temperatures, it tended to adhere to the SHS as T_s was reduced from 278 K to 248 K, with an increase in contact time and a decrease in rebounding height, as shown in Figure 5.9 and Figure 5.10. Based on the results of parametric study, it was apparent that wetting transition was the dominant factor determining the droplet impacting behaviors on an SHS near freezing temperatures. For fully droplet rebound, it was a necessity for the impact water droplet to possess sufficiently initial potential energy for energy loss due to droplet-surface adhesion and droplet viscosity (in Figure 5.18). Besides, the vertical surface force near SHS should be sufficiently large to drag the droplet away from the SHS (in Figure 5.19).

5.4.3. Limitation of modellings in this work

In Chapter 5.3, the numerical droplet impacting dynamics are compared with experimental results from the perspective of droplet shapes (Figure 5.7), contact length (Figure 5.8), contact time (Figure 5.9), rebounding height (Figure 5.10), and viscous loss

(Figure 5.11). The simulation results of current quasi-dynamic contact angle model agreed well with the droplet impacting behaviors in consideration of the droplet recoiling from an SHS. For example, the contact length and contact time showed consistency between experiments and simulations, and the modeling was sufficient to evaluate whether the droplet could fully rebound from an SHS under different conditions. However, the current modellings still had some drawbacks.

Firstly, during droplet rebound, (e.g., 10 ms and 14.1 ms for T_s = 278 K, 10 ms and 14.1 ms for T_s= 268 K, 10 ms and 15.2 ms for T_s = 258 K, and 10 ms and 15 ms for T_s = 248 K in Figure 5.7), for the upper half the water droplet, the droplet in CFD simulation was much more circular than in experiments. Meanwhile, the elongation of droplet in simulation was much shorter than in experiments. Besides, for lower SHS temperatures (258 K and 248 K) after droplet minimum recoiling the numerical simulation overestimated the droplet contact lengths compared with experiments. Therefore, the modeling needs improving for the sake of reproducing droplet impacting behaviors more precisely. For example, more accurate contact angle models and material properties of the impact droplet properties should be considered to optimize the current simulations.

Secondly, the current 2D axisymmetric simulation under cylindrical coordinate shows that during droplet impact, especially near the droplet maximum spreading, the droplet is in a doughnut shape instead of flattened. Figure 5.27 compares cross-sectional images, the numerical side-view images, and the experimental side-view images of an impact water droplet with the diameter of D_M at 278 K impacting on an SHS at 278 K from 3 ms to 5 ms. The impact water droplet is in concave shape at these moments. When developing models to calculate the maximum spreading of an impact water droplet on a surface, it is necessary to take the concave droplet shape into consideration. Besides, in current experiment setup the high-speed camera was arranged in line with the droplet to capture the droplet impacting process from the side view and to measure the contact angles. However, to study the droplet impacting dynamics, multiple high-speed cameras or taking images from different views are necessary to investigate the droplet impingement in a more comprehensive way.

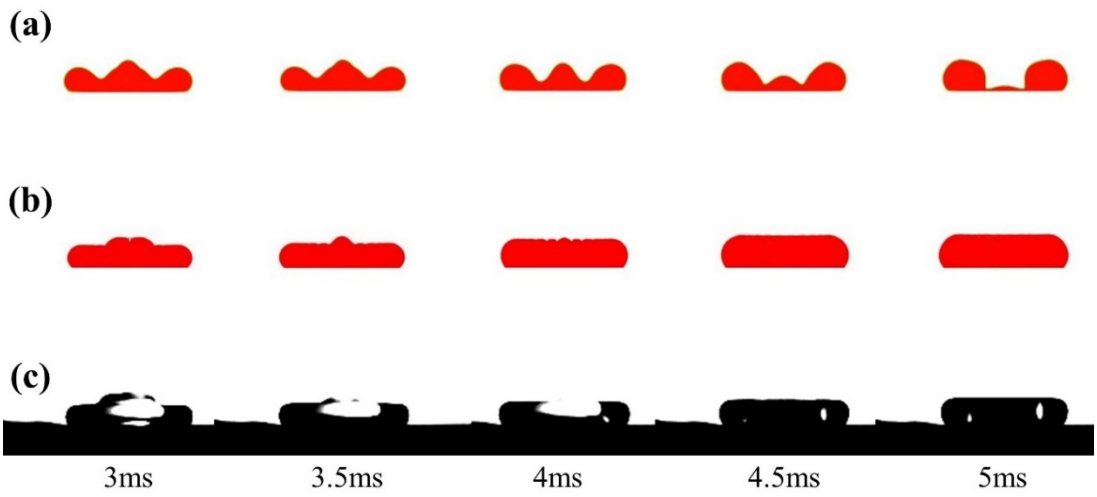

Figure 5.27 Comparison of the (a) cross-sectional images, (b) numerical side-view images, and (c) experimental side-view images of an impact water droplet on an SHS from 3 ms to 5 ms when both T_s and T_{wd} equal to 278 K.

Thirdly, the current numerical model failed to reproduce the droplet break-up phenomenon observed in Chapter 3 (e.g., T_s = 253 K in Figure 3.5). In Figure 5.14, it could be observed that during droplet recoil process (e.g., 10 ms), there was extremely non-uniform velocity distribution inside the water droplet. Specifically, for lower half of droplet near contact area between droplet and SHS droplet velocity approached to 0, while for upper half of droplet velocity was obviously larger owing to the conversion from surface energy to kinetic energy. This non-uniformity of velocity distribution could result in droplet break-up phenomenon. However, the droplet break-up phenomenon was not reproduced via the current numerical modellings.

5.5. Summary

In this CFD simulation work, VOF method was employed to interpret the spread and recoil process of a 278 K water droplet with diameter 2.44 mm impinging on an SHS at different temperatures (278 K–248 K). A body force based on continuum surface model was applied in momentum equation to account for the effect of surface tension. Wall adhesion model and quasi-dynamic contact angle model were utilized to involve contact angles measured in our previous experiments as a wall boundary condition. The modeling

was validated through comparing numerical droplet rebounding behaviors and viscous losses with experimental results. A detailed viscous loss analysis was carried out during droplet impacting process to interpret droplet impacting behaviors on an SHS at different temperatures, showing that over 70 % of the viscous loss occurred during droplet spreading and recoiling processes because of large droplet deformation and rapid transition between kinetic energy and surface energy.

Furthermore, the impinging physics of a water droplet affected by surface characteristics (droplet-surface adhesion) and water droplet properties (droplet viscosity and surface tension coefficient) was investigated via parametric study. With the increase of droplet-surface adhesion, contact time increased and rebounding height became lower or even 0 as a result of an increase in energy loss owing to droplet-surface adhesion and a reduction in vertical surface force near surface. Non-wetting condition was considered to evaluate maximum viscous loss. The results showed that when initial potential energy of impact droplet was insufficient for summation of maximum viscous loss and adhesion loss, droplet became stuck to surface. Within the temperature range of our current work, when viscosity of water increased, contact time demonstrated an irrelevant change but rebounding height was decreased owing to the increase of viscous loss. When surface tension coefficient of water increased, the contact time decreased, and the rebounding height increased. The parametric study demonstrated that as a water droplet impacted on an SHS near freezing temperatures, wetting transition was the dominant factor determining droplet rebounding behaviors.

Interpretation of the physics of an impact water droplet in bouncing state and the viscous losses during droplet impingement on surfaces would give valuable hints on SHS designs for real applications. For instance, super-hydrophobic structures could be designed to confine droplet spreading to reduce the viscous loss and adhesion loss during this process, and thus there would be more kinetic energy remained, increasing the chance of droplet fully rebounding.

Chapter 6 Conclusions and Prospects

Through mimicking surfaces of plants and animals in nature, the present research utilized AB nano particles and TMSS to successfully fabricate SHS with excellent super-hydrophobicity. Using this prepared SHS, the present research investigated the droplet impact behaviors on an SHS near freezing temperatures. Furthermore, the present research studied the droplet impact dynamics on a cold SHS via CFD simulations. The following conclusions have been obtained:

1. Through investigating the water droplet impacting behaviors on an SHS near freezing temperatures affected by SHS temperature, water droplet temperature, and droplet size, this research proposed that during droplet impact, water vapor evaporated from the impact water droplet and condensed inside cold SHS micro/nano textures, forming water bridges between the impact water droplet and SHS. The present research employed a 1D vapor-liquid phase transport model to estimate the thickness of condensed water to validate the proposed regime.
2. As the condensed water accumulated inside SHS hierarchical micro/nano textures, wetting transition from the Cassie-Baxter state to Wenzel state took place. The adhesion between impact water droplet and SHS increased. During droplet recoil, more kinetic energy was lost to separate droplet from surface and less kinetic energy was remained, so an increased contact time and a decreased rebounding height were observed. The present research analyzed the energy loss due to droplet-SHS adhesion and energy loss due to water viscosity during droplet impact. To validate the occurrence of wetting transition owing to condensed water, the present research also investigated the wetting transition of a sessile water droplet on an SHS near freezing temperatures and found that wetting transition of a sessile water droplet on a cold SHS was irrelevant to surface temperature owing to sufficient time of condensation.
3. Through adding the contact angle measured from experiments as a wall boundary condition, the CFD modellings reproduced droplet impact behaviors displayed in experiments and validated the energy loss analysis in experiments.

Time-course viscous loss of an impact water droplet was investigated to decipher the droplet impacting dynamics. Viscous loss during droplet spread and recoil accounted for over 70 % of total viscous loss. The parametric study in consideration of the contact angle, water viscosity, surface tension coefficient demonstrated that wetting transition was the dominant factor determining droplet impacting behaviors on an SHS near freezing temperatures. When wetting transition happened, the initial potential energy was insufficient to separate the droplet from surface due to the energy loss increase in adhesion. In addition, when wetting transition happened, there was a significant decrease in surface force especially in vertical direction, so the impact water droplet lost the momentum to bounce off. In addition, non-wetting condition was adopted to estimate maximum viscous loss and the results showed that droplet lost its rebounding capability when the summation of maximum viscous loss and maximum adhesion loss was larger than the initial potential energy.

4. The present research demonstrated a previously ignored regime for the forfeit of rebounding capacity of an impact water droplet on an SHS near freezing temperatures. For the design of SHS in the field of anti-icing, the SHS is expected to repel incoming water droplets under various practical conditions. Based on the outcomes of this research, inside SHS micro/nano textures, it is indispensable to consider the condensation of water vapors evaporated from the impact droplet. This can destroy surface wettability and determine the rebounding capability of incoming water droplets.

A consensus in the existing literature is that a more favorable condition for the droplet to lose its rebounding capability is at lower temperature due to the ease of ice nucleation inside the droplet. However, the present research revealed that, the rebounding capability of the droplet significantly reduced or even completely lost for higher droplet temperatures due to enhanced adhesion between the droplet and formed water bridges within micro/nano surface cavities by the condensation of evaporated water vapor from the droplet. It is anticipated that the proper understanding of this phenomenon will be beneficial to design improved SHS in passively anti-icing apparatus.

Conclusions and Prospects

Limited by the experimental facilities and SHS fabrication techniques, the current research has several drawbacks, meanwhile opens possibilities for future research. Firstly, the accumulation of condensed water inside SHS micro/nano cavities cannot be visually captured or measured, which makes the verification of condensation regime challenging. To solve this problem, SHS prepared with transparent materials and optical measurement methods might be considered to facilitate the evaluation of water condensation on SHS textures. Secondly, when water condensation accumulates and wetting transition from the Cassie-Baxter state to Wenzel state takes place, instead of the average contact angle measured from experiments, contact angle model incorporating the influence of wetting transition (as shown in Appendix H) could be developed. However, the current SHS is made of uniform surface textures from nanoscale to microscale. SHS with uniform surface textures of different dimensions is necessary for contact angle modelling and the model validating. Thirdly, so far in literature, when considering the droplet impacting behaviors for anti-icing, only low-humidity ambient environment is considered, which is a fatal limitation for real applications. Because water condensation and frost formation of the ambient vapors take place on SHS in freezing conditions. Thus, SHS design capable of preventing the destroy of surface wettability from the environmental vapors is required. Finally, when considered for practical applications, repeatability of SHS needs considering to improve the working efficiency of anti-icing.

Reference

[1] N.J. Shirtcliffe, G. McHale, S. Atherton, M.I. Newton, An introduction to superhydrophobicity, Adv. Colloid Interface Sci. 161 (2010) 124–138. https://doi.org/10.1016/j.cis.2009.11.001.

[2] J. Jeevahan, M. Chandrasekaran, G. Britto Joseph, R.B. Durairaj, G. Mageshwaran, Superhydrophobic surfaces: a review on fundamentals, applications, and challenges, J. Coatings Technol. Res. 15 (2018) 231–250. https://doi.org/10.1007/s11998-017-0011-x.

[3] S. Li, J. Huang, Z. Chen, G. Chen, Y. Lai, A review on special wettability textiles: theoretical models, fabrication technologies and multifunctional applications, J. Mater. Chem. A. 5 (2017) 31–55. https://doi.org/10.1039/c6ta07984a.

[4] W. Barthlott, C. Neinhuis, Purity of the scared lotus, or escape from contamination in biological surfaces, Q. J. Geol. Soc. 69 (1996) 85–116. https://doi.org/10.1144/GSL.JGS.1913.069.01-04.09.

[5] L. Feng, Y. Zhang, J. Xi, Y. Zhu, N. Wang, F. Xia, L. Jiang, Petal effect: A superhydrophobic state with high adhesive force, Langmuir. 24 (2008) 4114–4119. https://doi.org/10.1021/la703821h.

[6] X. Gao, L. Jiang, Water-repellent legs of water striders, Nature. 432 (2004) 36. https://doi.org/10.1038/432036a.

[7] G.D. Bixler, B. Bhushan, Rice- and butterfly-wing effect inspired self-cleaning and low drag micro/nanopatterned surfaces in water, oil, and air flow, Nanoscale. 6 (2014) 76–96. https://doi.org/10.1039/c3nr04755e.

[8] L. Feng, Y. Zhang, Y. Cao, X. Ye, L. Jiang, The effect of surface microstructures and surface compositions on the wettabilities of flower petals, Soft Matter. 7 (2011) 2977–2980. https://doi.org/10.1039/c0sm01032d.

[9] H. Taneda, A. Watanabe-Taneda, R. Chhetry, H. Ikeda, A theoretical approach to the relationship between wettability and surface microstructures of epidermal cells and

structured cuticles of flower petals, Ann. Bot. 115 (2015) 923–937. https://doi.org/10.1093/aob/mcv024.

[10] T. Young, An Essay on the Cohesion of Fluids. By Thomas Young, Philos. Trans. R. Soc. London. 95 (1805) 65–87. http://www.jstor.org/stable/107159.

[11] M. Liu, S. Wang, L. Jiang, Nature-inspired superwettability systems, Nat. Rev. Mater. 2 (2017). https://doi.org/10.1038/natrevmats.2017.36.

[12] J. Lv, Y. Song, L. Jiang, J. Wang, Bio-inspired strategies for anti-icing, ACS Nano. 8 (2014) 3152–3169. https://doi.org/10.1021/nn406522n.

[13] H. Ogihara, J. Xie, J. Okagaki, T. Saji, Simple method for preparing superhydrophobic paper: Spray-deposited hydrophobic silica nanoparticle coatings exhibit high water-repellency and transparency, Langmuir. 28 (2012) 4605–4608. https://doi.org/10.1021/la204492q.

[14] H. Ogihara, J. Okagaki, T. Saji, Facile fabrication of colored superhydrophobic coatings by spraying a pigment nanoparticle suspension, Langmuir. 27 (2011) 9069–9072. https://doi.org/10.1021/la200898z.

[15] E. Bormashenko, T. Stein, G. Whyman, Y. Bormashenko, R. Pogreb, Wetting properties of the multiscaled nanostructured polymer and metallic superhydrophobic surfaces, Langmuir. 22 (2006) 9982–9985. https://doi.org/10.1021/la061622m.

[16] N.J. Shirtcliffe, G. McHale, M.I. Newton, C.C. Perry, F.B. Pyatt, Plastron properties of a superhydrophobic surface, Appl. Phys. Lett. 89 (2006) 2005–2007. https://doi.org/10.1063/1.2347266.

[17] J.N. Mateo, S.S. Kulkarni, L. Das, S. Bandyopadhyay, G.C. Tepper, K. JWynne, S. Bandyopadhyay, Wetting behavior of polymer coated nanoporous anodic alumina films: Transition from super-hydrophilicity to super-hydrophobicity, Nanotechnology. 22 (2011). https://doi.org/10.1088/0957-4484/22/3/035703.

[18] K.B.K. Teo, D.B. Hash, R.G. Lacerda, N.L. Rupesinghe, M.S. Bell, S.H. Dalal, D. Bose, T.R. Govindan, B.A. Cruden, M. Chhowalla, G.A.J. Amaratunga, M. Meyyappan,

Reference

W.I. Milne, The significance of plasma heating in carbon nanotube and nanofiber growth, Nano Lett. 4 (2004) 921–926. https://doi.org/10.1021/nl049629g.

[19] H. Liu, J. Zhai, L. Jiang, Wetting and anti-wetting on aligned carbon nanotube films, Soft Matter. 2 (2006) 811–821. https://doi.org/10.1039/b606654b.

[20] S.Y. Chou, C. Keimel, J. Gu, Ultrafast and direct imprint of nanostructures in silicon, Nature. 417 (2002) 835–837. https://doi.org/10.1038/nature00792.

[21] D.M. Spori, T. Drobek, S. Zürcher, M. Ochsner, C. Sprecher, A. Mühlebach, N.D. Spencer, Beyond the lotus effect: Roughness influences on wetting over a wide surface-energy range, Langmuir. 24 (2008) 5411–5417. https://doi.org/10.1021/la800215r.

[22] M. Sun, X. Li, B. Ding, J. Yu, G. Sun, Mechanical and wettable behavior of polyacrylonitrile reinforced fibrous polystyrene mats, J. Colloid Interface Sci. 347 (2010) 147–152. https://doi.org/10.1016/j.jcis.2010.03.026.

[23] M.R. Karim, M.S. Islam, Thermal behavior with mechanical property of fluorinated silane functionalized superhydrophobic pullulan/poly (vinyl alcohol) blends by electrospinning method, J. Nanomater. 2011 (2011). https://doi.org/10.1155/2011/979458.

[24] C. Gu, T.Y. Zhang, Electrochemical synthesis of silver polyhedrons and dendritic films with superhydrophobic surfaces, Langmuir. 24 (2008) 12010–12016. https://doi.org/10.1021/la802354n.

[25] I.A. Larmour, S.E.J. Bell, G.C. Saunders, Remarkably simple fabrication of superhydrophobic surfaces using electroless galvanic deposition, Angew. Chemie - Int. Ed. 46 (2007) 1710–1712. https://doi.org/10.1002/anie.200604596.

[26] Y.H. Sung, Y.D. Kim, H.J. Choi, R. Shin, S. Kang, H. Lee, Fabrication of superhydrophobic surfaces with nano-in-micro structures using UV-nanoimprint lithography and thermal shrinkage films, Appl. Surf. Sci. 349 (2015) 169–173. https://doi.org/10.1016/j.apsusc.2015.04.141.

[27] R. Menini, M. Farzaneh, Elaboration of Al2O3/PTFE icephobic coatings for protecting aluminum surfaces, Surf. Coatings Technol. 203 (2009) 1941–1946. https://doi.org/10.1016/j.surfcoat.2009.01.030.

Reference

[28] L. Zhu, J. Xue, Y. Wang, Q. Chen, J. Ding, Q. Wang, Ice-phobic Coatings Based on Silicon-Oil-Infused Polydimethylsiloxane, (2013). https://doi.org/10.1021/am400704z.

[29] S. Wang, K. Liu, J. Liu, Z.T.F. Yu, X. Xu, L. Zhao, T. Lee, E.K. Lee, J. Reiss, Y.K. Lee, L.W.K. Chung, J. Huang, M. Rettig, D. Seligson, K.N. Duraiswamy, C.K.F. Shen, H.R. Tseng, Highly efficient capture of circulating tumor cells by using nanostructured silicon substrates with integrated chaotic micromixers, Angew. Chemie - Int. Ed. 50 (2011) 3084–3088. https://doi.org/10.1002/anie.201005853.

[30] H. Liu, Y. Li, K. Sun, J. Fan, P. Zhang, J. Meng, S. Wang, L. Jiang, Dual-responsive surfaces modified with phenylboronic acid-containing polymer brush to reversibly capture and release cancer cells, J. Am. Chem. Soc. 135 (2013) 7603–7609. https://doi.org/10.1021/ja401000m.

[31] P. Zhang, L. Lin, D. Zang, X. Guo, M. Liu, Designing Bioinspired Anti-Biofouling Surfaces based on a Superwettability Strategy, Small. 13 (2017) 1–9. https://doi.org/10.1002/smll.201503334.

[32] D. Zang, H. Yi, Z. Gu, L. Chen, D. Han, X. Guo, S. Wang, M. Liu, L. Jiang, Interfacial Engineering of Hierarchically Porous NiTi/Hydrogels Nanocomposites with Exceptional Antibiofouling Surfaces, Adv. Mater. 29 (2017) 1–7. https://doi.org/10.1002/adma.201602869.

[33] Z. Shi, W. Zhang, F. Zhang, X. Liu, D. Wang, J. Jin, L. Jiang, Ultrafast separation of emulsified oil/water mixtures by ultrathin free-standing single-walled carbon nanotube network films, Adv. Mater. 25 (2013) 2422–2427. https://doi.org/10.1002/adma.201204873.

[34] Z. Xue, Y. Cao, N. Liu, L. Feng, L. Jiang, Special wettable materials for oil/water separation, J. Mater. Chem. A. 2 (2014) 2445–2460. https://doi.org/10.1039/c3ta13397d.

[35] F. De Angelis, F. Gentile, F. Mecarini, G. Das, M. Moretti, P. Candeloro, M.L. Coluccio, G. Cojoc, A. Accardo, C. Liberale, R.P. Zaccaria, G. Perozziello, L. Tirinato, A. Toma, G. Cuda, R. Cingolani, E. Di Fabrizio, Breaking the diffusion limit with super-

hydrophobic delivery of molecules to plasmonic nanofocusing SERS structures, Nat. Photonics. 5 (2011) 682–687. https://doi.org/10.1038/nphoton.2011.222.

[36] S. Yang, X. Dai, B.B. Stogin, T.S. Wong, Ultrasensitive surface-enhanced Raman scattering detection in common fluids, Proc. Natl. Acad. Sci. U. S. A. 113 (2016) 268–273. https://doi.org/10.1073/pnas.1518980113.

[37] D. Tian, Y. Song, L. Jiang, Patterning of controllable surface wettability for printing techniques, Chem. Soc. Rev. 42 (2013) 5184–5209. https://doi.org/10.1039/c3cs35501b.

[38] D.P. McMeekin, G. Sadoughi, W. Rehman, G.E. Eperon, M. Saliba, M.T. Hörantner, A. Haghighirad, N. Sakai, L. Korte, B. Rech, M.B. Johnston, L.M. Herz, H.J. Snaith, A mixed-cation lead mixed-halide perovskite absorber for tandem solar cells, Science (80-.). 351 (2016) 151–155. https://doi.org/10.1126/science.aad5845.

[39] J. Zhu, C.M. Hsu, Z. Yu, S. Fan, Y. Cui, Nanodome solar cells with efficient light management and self-cleaning, Nano Lett. 10 (2010) 1979–1984. https://doi.org/10.1021/nl9034237.

[40] S. Zhang, J. Huang, Y. Cheng, H. Yang, Z. Chen, Y. Lai, Bioinspired Surfaces with Superwettability for Anti-Icing and Ice-Phobic Application: Concept, Mechanism, and Design, Small. 13 (2017) 1–20. https://doi.org/10.1002/smll.201701867.

[41] M. Farzaneh, C. Volat, A. Leblond, Anti-icing and de-icing techniques for overhead lines, Springer: Netherlands. (2008) 229–268.

[42] Y. Cao, Z. Wu, Y. Su, Z. Xu, Aircraft flight characteristics in icing conditions, Prog. Aerosp. Sci. 74 (2015) 62–80. https://doi.org/10.1016/j.paerosci.2014.12.001.

[43] K.W. Howard, J. Haynes, Groundwater contamination due to road de-icing chemicals salt balance implications, Geosci. Can. 20 (1993) 1–8. https://journals.lib.unb.ca/index.php/GC/article/view/3784/4298.

[44] J.L. Laforte, M.A. Allaire, J. Laflamme, State-of-the-art on power line de-icing, Atmos. Res. 46 (1998) 143–158. https://doi.org/10.1016/S0169-8095(97)00057-4.

Reference

[45] M.J. Kreder, J. Alvarenga, P. Kim, J. Aizenberg, Design of anti-icing surfaces: Smooth, textured or slippery?, Nat. Rev. Mater. 1 (2016). https://doi.org/10.1038/natrevmats.2015.3.\

[46] M.D. Mulroe, B.R. Srijanto, S.F. Ahmadi, C.P. Collier, J.B. Boreyko, Tuning Superhydrophobic Nanostructures to Enhance Jumping-Droplet Condensation, ACS Nano. 11 (2017) 8499–8510. https://doi.org/10.1021/acsnano.7b04481.

[47] J.B. Boreyko, C.P. Collier, Delayed frost growth on jumping-drop superhydrophobic surfaces, ACS Nano. 7 (2013) 1618–1627. https://doi.org/10.1021/nn3055048.

[48] T.M. Schutzius, S. Jung, T. Maitra, G. Graeber, M. Köhme, D. Poulikakos, Spontaneous droplet trampolining on rigid superhydrophobic surfaces, Nature. 527 (2015) 82–85. https://doi.org/10.1038/nature15738.

[49] G. Graeber, T.M. Schutzius, H. Eghlidi, D. Poulikakos, Spontaneous self-dislodging of freezing water droplets and the role of wettability, Proc. Natl. Acad. Sci. U. S. A. 114 (2017) 11040–11045. https://doi.org/10.1073/pnas.1705952114.

[50] S. Jung, M. Dorrestijn, D. Raps, A. Das, C.M. Megaridis, D. Poulikakos, Are superhydrophobic surfaces best for icephobicity?, Langmuir. 27 (2011) 3059–3066. https://doi.org/10.1021/la104762g.

[51] A. Alizadeh, M. Yamada, R. Li, W. Shang, S. Otta, S. Zhong, L. Ge, A. Dhinojwala, K.R. Conway, V. Bahadur, A.J. Vinciquerra, B. Stephens, M.L. Blohm, Dynamics of ice nucleation on water repellent surfaces, Langmuir. 28 (2012) 3180–3186. https://doi.org/10.1021/la2045256.

[52] S. Bengaluru Subramanyam, V. Kondrashov, J. Rühe, K.K. Varanasi, Low Ice Adhesion on Nano-Textured Superhydrophobic Surfaces under Supersaturated Conditions, ACS Appl. Mater. Interfaces. 8 (2016) 12583–12587. https://doi.org/10.1021/acsami.6b01133.

[53] A.J. Meuler, J.D. Smith, K.K. Varanasi, J.M. Mabry, G.H. McKinley, R.E. Cohen, Relationships between water wettability and ice adhesion, ACS Appl. Mater. Interfaces. 2 (2010) 3100–3110. https://doi.org/10.1021/am1006035.

Reference

[54] P. Kim, T.S. Wong, J. Alvarenga, M.J. Kreder, W.E. Adorno-Martinez, J. Aizenberg, Liquid-infused nanostructured surfaces with extreme anti-ice and anti-frost performance, ACS Nano. 6 (2012) 6569–6577. https://doi.org/10.1021/nn302310q.

[55] D. Richard, D. Quéré, Bouncing water drops, Europhys. Lett. 50 (2000) 769–775. https://doi.org/10.1209/epl/i2000-00547-6.

[56] Y. Liu, X. Yan, Z. Wang, Droplet dynamics on slippery surfaces: Small droplet, big impact, Biosurface and Biotribology. 5 (2019) 35–45. https://doi.org/10.1049/bsbt.2019.0004.

[57] L. Courbin, J.C. Bird, M. Reyssat, H.A. Stone, Dynamics of wetting: From inertial spreading to viscous imbibition, J. Phys. Condens. Matter. 21 (2009). https://doi.org/10.1088/0953-8984/21/46/464127.

[58] T. Mao, D.C.S. Kuhn, H. Tran, Spread and Rebound of Liquid Droplets upon Impact on Flat Surfaces, AIChE J. 43 (1997) 2169–2179. https://doi.org/10.1002/aic.690430903.

[59] R. Rioboo, C. Tropea, M. Marengo, Outcomes from a drop impact on solid surfaces, At. Sprays. 11 (2001) 155–165. https://doi.org/10.1615/atomizspr.v11.i2.40.

[60] C. Clanet, C. Béguin, D. Richard, D. Quéré, Maximal deformation of an impacting drop, J. Fluid Mech. 517 (2004) 199–208. https://doi.org/10.1017/S0022112004000904.

[61] M. Pasandideh-Fard, Y.M. Qiao, S. Chandra, J. Mostaghimi, Capillary effects during droplet impact on a solid surface, Phys. Fluids. 8 (1996) 650–659. https://doi.org/10.1063/1.868850.

[62] C. Ukiwe, D.Y. Kwok, On the maximum spreading diameter of impacting droplets on well-prepared solid surfaces, Langmuir. 21 (2005) 666–673. https://doi.org/10.1021/la0481288.

[63] J.B. Lee, D. Derome, A. Dolatabadi, J. Carmeliet, Energy Budget of Liquid Drop Impact at Maximum Spreading: Numerical Simulations and Experiments, Langmuir. 32 (2016) 1279–1288. https://doi.org/10.1021/acs.langmuir.5b03848.

Reference

[64] F. Wang, L. Yang, L. Wang, Y. Zhu, T. Fang, Maximum Spread of Droplet Impacting onto Solid Surfaces with Different Wettabilities: Adopting a Rim-Lamella Shape, Langmuir. 35 (2019) 3204–3214. https://doi.org/10.1021/acs.langmuir.8b03748.

[65] I. V. Roisman, R. Rioboo, C. Tropea, Normal impact of a liquid drop on a dry surface: Model for spreading and receding, Proc. R. Soc. A Math. Phys. Eng. Sci. 458 (2002) 1411–1430. https://doi.org/10.1098/rspa.2001.0923.

[66] D. Richard, C. Clanet, D. Quéré, Surface phenomena: Contact time of a bouncing drop, Nature. 417 (2002) 811–811. https://doi.org/10.1038/417811a.

[67] J.C. Bird, R. Dhiman, H.M. Kwon, K.K. Varanasi, Reducing the contact time of a bouncing drop, Nature. 503 (2013) 385–388. https://doi.org/10.1038/nature12740.

[68] Y. Liu, L. Moevius, X. Xu, T. Qian, J.M. Yeomans, Z. Wang, Pancake bouncing on superhydrophobic surfaces, Nat. Phys. 10 (2014) 515–519. https://doi.org/10.1038/nphys2980.

[69] B. Ding, H. Wang, X. Zhu, R. Chen, Q. Liao, Water droplet impact on superhydrophobic surfaces with various inclinations and supercooling degrees, Int. J. Heat Mass Transf. 138 (2019) 844–851. https://doi.org/10.1016/j.ijheatmasstransfer.2019.04.106.

[70] A. Al-Sharafi, B.S. Yilbas, H. Ali, N. Alaqeeli, A Water Droplet Pinning and Heat Transfer Characteristics on an Inclined Hydrophobic Surface, Sci. Rep. 8 (2018) 1–20. https://doi.org/10.1038/s41598-018-21511-w.

[71] R. Ma, X. Zhou, B. Dong, W. Li, J. Gong, Simulation of impacting process of a saturated droplet upon inclined surfaces by lattice Boltzmann method, Int. J. Heat Fluid Flow. 71 (2018) 1–12. https://doi.org/10.1016/j.ijheatfluidflow.2018.03.001.

[72] S. Ding, X. Liu, X. Wu, X. Zhang, Droplet breakup and rebound during impact on small cylindrical superhydrophobic targets, Phys. Fluids. 32 (2020). https://doi.org/10.1063/5.0024837.

[73] X. Liu, X. Zhang, J. Min, Maximum spreading of droplets impacting spherical surfaces, Phys. Fluids. 31 (2019). https://doi.org/10.1063/1.5117278.

Reference

[74] L. Mishchenko, B. Hatton, V. Bahadur, A. Taylor, J., T. Krupenkin, J. Aizenberg, Design of Ice-free Nanostructured Impacting Water Droplets, ACS Nano. 4 (2010) 7699–7707. https://doi.org/10.1021/nn102557p.

[75] V. Bahadur, L. Mishchenko, B. Hatton, J.A. Taylor, J. Aizenberg, T. Krupenkin, Predictive model for ice formation on superhydrophobic surfaces, Langmuir. 27 (2011) 14143–14150. https://doi.org/10.1021/la200816f.

[76] R. Zhang, P. Hao, X. Zhang, F. He, Supercooled Water Droplet Impact on Superhydrophobic Surfaces with Various Roughness and Temperature, International Journal of Heat and Mass Transfer 122 (2018) 395–402. https://doi.org/10.1016/j.ijheatmasstransfer.2018.01.076.

[77] B. Ding, H. Wang, X. Zhu, R. Chen, Q. Liao, How Supercooled Superhydrophobic Surfaces Affect Dynamic Behaviors of Impacting Water Droplets? International Journal of Heat and Mass Transfer 124 (2018) 1025–1032. https://doi.org/10.1016/j.ijheatmasstransfer.2018.03.112.

[78] Y. Shen, J. Tao, G. Wang, C. Zhu, H. Chen, M. Jin, Y. Xie, Bioinspired Fabrication of Hierarchical-Structured Superhydrophobic Surfaces to Understand Droplet Bouncing Dynamics for Enhancing Water Repellency, The Journal of Physical Chemistry C 122 (13) (2018) 7312–7320. https://doi.org/10.1021/acs.jpcc.8b01538.

[79] A. B. D. Cassie, S. Baxter, Wettability of porous surfaces, Trans. Faraday Soc., 1944, 40, 546–551. https://doi.org/10.1039/TF9444000546.

[80] R. N. Wenzel, Resistance of solid surfaces to wetting by water, Ind. Eng. Chem. 28, 988 (1936). https://doi.org/10.1021/ie50320a024.

[81] G. Heydari, E. Thormann, M. Järn, E. Tyrode, P.M. Claesson, Hydrophobic surfaces: Topography effects on wetting by supercooled water and freezing delay, J. Phys. Chem. C. 117 (2013) 21752–21762. https://doi.org/10.1021/jp404396m.

[82] G. Heydari, M. Sedighi Moghaddam, M. Tuominen, M. Fielden, J. Haapanen, J.M. Mäkelä, P.M. Claesson, Wetting hysteresis induced by temperature changes: Supercooled

water on hydrophobic surfaces, J. Colloid Interface Sci. 468 (2016) 21–33. https://doi.org/10.1016/j.jcis.2016.01.040.

[83] M. Macias-Montero, C. Lopez-Santos, A.N. Filippin, V.J. Rico, J.P. Espinos, J. Fraxedas, V. Perez-Dieste, C. Escudero, A.R. Gonzalez-Elipe, A. Borras, In Situ Determination of the Water Condensation Mechanisms on Superhydrophobic and Superhydrophilic Titanium Dioxide Nanotubes, Langmuir. 33 (2017) 6449–6456. https://doi.org/10.1021/acs.langmuir.7b00156.

[84] V. Bahadur, S. V. Garimella, Preventing the cassie-wenzel transition using surfaces with noneommunicating roughness elements, Langmuir. 25 (2009) 4815–4820. https://doi.org/10.1021/la803691m.

[85] R. Wen, Z. Lan, B. Peng, W. Xu, R. Yang, X. Ma, Wetting Transition of Condensed Droplets on Nanostructured Superhydrophobic Surfaces: Coordination of Surface Properties and Condensing Conditions, ACS Appl. Mater. Interfaces. 9 (2017) 13770–13777. https://doi.org/10.1021/acsami.7b01812.

[86] Y. Zhao, H. Zhang, W. Wang, C. Yang, Wetting transition of sessile and condensate droplets on copper-based superhydrophobic surfaces, Int. J. Heat Mass Transf. 127 (2018) 280–288. https://doi.org/10.1016/j.ijheatmasstransfer.2018.07.153.

[87] J. Gerber, T. Lendenmann, H. Eghlidi, T.M. Schutzius, D. Poulikakos, Wetting transitions in droplet drying on soft materials, Nat. Commun. 10 (2019). https://doi.org/10.1038/s41467-019-12093-w.

[88] T. Mouterde, P. Lecointre, G. Lehoucq, A. Checco, C. Clanet, D. Quéré, Two recipes for repelling hot water, Nat. Commun. 10 (2019) 1–7. https://doi.org/10.1038/s41467-019-09456-8.

[89] S. Shiri, A. Murrizi, J.C. Bird, Trapping a hot drop on a superhydrophobic surface with rapid condensation or microtexture melting, Micromachines. 9 (2018) 1–11. https://doi.org/10.3390/mi9110566.

Reference

[90] D. Bartolo, F. Bouamrirene, É. Verneuil, A. Buguin, P. Silberzan, S. Moulinet, Bouncing or sticky droplets: Impalement transitions on superhydrophobic micropatterned surfaces, Europhys. Lett. 74 (2006) 299–305. https://doi.org/10.1209/epl/i2005-10522-3.

[91] T. Vasileiou, T.M. Schutzius, D. Poulikakos, Imparting Icephobicity with Substrate Flexibility, Langmuir. 33 (2017) 6708–6718. https://doi.org/10.1021/acs.langmuir.7b01412.

[92] T. Maitra, C. Antonini, M. Auf Der Mauer, C. Stamatopoulos, M.K. Tiwari, D. Poulikakos, Hierarchically nanotextured surfaces maintaining superhydrophobicity under severely adverse conditions, Nanoscale. 6 (2014) 8710–8719. https://doi.org/10.1039/c4nr01368a.

[93] Y.C. Jung, B. Bhushan, Dynamic effects of bouncing water droplets on superhydrophobic surfaces, Langmuir. 24 (2008) 6262–6269. https://doi.org/10.1021/la8003504.

[94] D. Khojasteh, M. Kazerooni, S. Salarian, R. Kamali, Droplet impact on superhydrophobic surfaces: A review of recent developments, J. Ind. Eng. Chem. 42 (2016) 1–14. https://doi.org/10.1016/j.jiec.2016.07.027.

[95] C.W. Hirt, B.D. Nichols, Volume of fluid (VOF) method for the dynamics of free boundaries, J. Comput. Phys. 39 (1981) 201–225. https://doi.org/10.1016/0021-9991(81)90145-5.

[96] E. Olsson, G. Kreiss, A conservative level set method for two phase flow, J. Comput. Phys. 210 (2005) 225–246. https://doi.org/10.1016/j.jcp.2005.04.007.

[97] B.A. Dwiyantoro, Capillary effects during droplet formation on the solid surface, Adv. Mater. Res. 683 (2013) 889–893.

https://doi.org/10.4028/www.scientific.net/AMR.683.889.

[98] J. Qu, Y. Yang, S. Yang, D. Hu, H. Qiu, Droplet impingement on nano-textured superhydrophobic surface: Experimental and numerical study, Appl. Surf. Sci. 491 (2019) 160–170. https://doi.org/10.1016/j.apsusc.2019.06.104.

Reference

[99] M.M. Farhangi, P.J. Graham, N.R. Choudhury, A. Dolatabadi, Induced detachment of coalescing droplets on superhydrophobic surfaces, Langmuir. 28 (2012) 1290–1303. https://doi.org/10.1021/la203926q.

[100] S.F. Lunkad, V. V. Buwa, K.D.P. Nigam, Numerical simulations of drop impact and spreading on horizontal and inclined surfaces, Chem. Eng. Sci. 62 (2007) 7214–7224. https://doi.org/10.1016/j.ces.2007.07.036.

[101] X. Zhang, X. Liu, X. Wu, J. Min, Impacting-freezing dynamics of a supercooled water droplet on a cold surface: Rebound and adhesion, Int. J. Heat Mass Transf. 158 (2020) 119997. https://doi.org/10.1016/j.ijheatmasstransfer.2020.119997.

[102] S.N. Chang, D. Liang, M.J. Song, M.Y. Leng, Numerical investigation on impingement dynamics and freezing performance of micrometer-sized water droplet on dry flat surface in supercooled environment, Int. J. Multiph. Flow. 118 (2019) 150–164. https://doi.org/10.1016/j.ijmultiphaseflow.2019.06.011.

[103] Y. Yao, C. Li, H. Zhang, R. Yang, Modelling the impact, spreading and freezing of a water droplet on horizontal and inclined superhydrophobic cooled surfaces, Appl. Surf. Sci. 419 (2017) 52–62. https://doi.org/10.1016/j.apsusc.2017.04.085.

[104] R. Attarzadeh, A. Dolatabadi, Icephobic performance of superhydrophobic coatings: A numerical analysis, Int. J. Heat Mass Transf. 136 (2019) 1327–1337. https://doi.org/10.1016/j.ijheatmasstransfer.2019.03.079.

[105] J.G. Leidenfrost, On the fixation of water in diverse fire, Int. J. Heat Mass Transf. 9 (1966) 1153–1166. https://doi.org/10.1016/0017-9310(66)90111-6.

[106] N. Nikolopoulos, A. Theodorakakos, G. Bergeles, A numerical investigation of the evaporation process of a liquid droplet impinging onto a hot substrate, Int. J. Heat Mass Transf. 50 (2007) 303–319. https://doi.org/10.1016/j.ijheatmasstransfer.2006.06.012.

[107] G. Strotos, M. Gavaises, A. Theodorakakos, G. Bergeles, Numerical investigation of the cooling effectiveness of a droplet impinging on a heated surface, Int. J. Heat Mass Transf. 51 (2008) 4728–4742. https://doi.org/10.1016/j.ijheatmasstransfer.2008.02.036.

Reference

[108] G. Strotos, M. Gavaises, A. Theodorakakos, G. Bergeles, Numerical investigation on the evaporation of droplets depositing on heated surfaces at low Weber numbers, Int. J. Heat Mass Transf. 51 (2008) 1516–1529.

https://doi.org/10.1016/j.ijheatmasstransfer.2007.07.045.

[109] D.J.E. Harvie, D.F. Fletcher, A hydrodynamic and thermodynamic simulation of droplet impacts on hot surfaces, part I: Theoretical model, Int. J. Heat Mass Transf. 44 (2001) 2633–2642. https://doi.org/10.1016/S0017-9310(00)00303-3.

[110] D.J.E. Harvie, D.F. Fletcher, A hydrodyamic and thermodynamic simulation of droplet impacts on hot surfaces, Part II: Validation and applications, Int. J. Heat Mass Transf. 44 (2001) 2643–2659. https://doi.org/10.1016/S0017-9310(00)00304-5.

[111] Y. Tanaka, Y. Washio, M. Yoshino, T. Hirata, Numerical simulation of dynamic behavior of droplet on solid surface by the two-phase lattice Boltzmann method, Comput. Fluids. 40 (2011) 68–78. https://doi.org/10.1016/j.compfluid.2010.08.007.

[112] S. Chen, B. Zhang, X. Gao, Z. Liu, X. Zhang, Direction Dependence of Adhesion Force for Droplets on Rough Substrates, Langmuir. 33 (2017) 2472–2476. https://doi.org/10.1021/acs.langmuir.6b04668.

[113] R. Zhang, S. Farokhirad, T. Lee, J. Koplik, Multiscale liquid drop impact on wettable and textured surfaces, Phys. Fluids. 26 (2014). https://doi.org/10.1063/1.4892083.

[114] F. Mosher, D. Schaum, C. Herbster, T. Guinn, Analysis of Causes of Icing Conditions Which Contributed to the Crash of Continental Flight 3407. 14th Conference on Aviation, Range, and Aerospace Meteorology, 2010.

[115] A.R. Betz, Accelerated freezing due to droplet pinning on a nanopillared surface, AIP Adv. 8 (2018). https://doi.org/10.1063/1.5048933.

[116] M.R. Haque, S.R. Das, A.R. Betz, Experimental investigation of condensation and freezing phenomena on hydrophilic and hydrophobic graphene coating, Appl. Therm. Eng. 160 (2019) 113987. https://doi.org/10.1016/j.applthermaleng.2019.113987.

Reference

[117] S.K. Thomas, R.P. Cassoni, C.D. MacArthur, Aircraft anti-icing and de-icing techniques and modeling, Journal of Aircraft 33 (1996) 841-854. https://arc.aiaa.org/doi/pdfplus/10.25 14/3.47027

[118] M.I. Jamil, A. Ali, F. Haq, Q. Zhang, X. Zhan, F. Chen, Icephobic Strategies and Materials with Superwettability: Design Principles and Mechanism, Langmuir 34 (50) (2018) 15425–15444. https://doi.org/10.1021/acs.langmuir.8b03276.

[119] A.S. Van Dyke, D. Collard, M.M. Derby, A.R. Betz, Droplet coalescence and freezing on hydrophilic, hydrophobic, and biphilic surfaces, Applied Physical Letters 107 (2015) 1–5. https://doi.org/10.1063/1.4932050.

[120] P. Tourkine, M.L. Merrer, D. Quéré, Delayed Freezing on Water Repellent Materials, Langmuir 25 (13) (2009) 7214–7216. https://doi.org/10.1021/la900929u.

[121] K.K. Varanasi, T. Deng, J.D. Smith, M. Hsu, N. Bhate, Frost formation and ice adhesion on superhydrophobic surfaces, Applied Physical Letters 97 (234102) (2010). https://doi.org/10.1063/1.3524513.

[122] Sarkar, D. K.; Farzaneh, M. Superhydrophobic Coatings with Reduced Ice Adhesion. J. Adhes. Sci. Technol. 2009, 23 (9), 1215–1237.

https://doi.org/10.1163/156856109X433964.

[123] Cao, L.; Jones, A. K.; Sikka, V. K.; Wu, J.; Gao, D. Anti-Icing Superhydrophobic Coatings. Langmuir 2009, 25 (21), 12444–12448. https://doi.org/10.1021/la902882b.

[124] A. Dehaoui, B. Issenmann, F. Caupin, Viscosity of Deeply Supercooled Water and Its Coupling to Molecular Diffusion, Proceedings of the National Academy of Sciences of the United States of America 112 (39) (2015) 12020–12025. https://doi.org/10.1073/pnas.1508996112.

[125] T. Maitra, C. Antonini, M.K. Tiwari, A. Mularczyk, Z. Imeri, P. Schoch, D. Poulikakos, Supercooled Water Drops Impacting Superhydrophobic Textures, Langmuir 30 (36) (2014) 10855–10861. https://doi.org/10.1021/la502675a.

Reference

[126] T. Deng, K.K. Varanasi, M. Hsu, N. Bhate, C. Keimel, J. Stein, M. Blohm, Nonwetting of Impinging Droplets on Textured Surfaces, Applied Physics Letters 94 (13) (2009) 2–5. https://doi.org/10.1063/1.3110054.

[127] T. Maitra, M.K. Tiwari, C. Antonini, P. Schoch, S. Jung, P. Eberle, D. Poulikakos, On the Nanoengineering of Superhydrophobic and Impalement Resistant Surface Textures below the Freezing Temperature, Nano Letters 14 (1) (2014) 172–182. https://doi.org/10.1021/nl4037092.

[128] K.A. Wier, T.J. McCarthy, Condensation on Ultrahydrophobic Surfaces and Its Effect on Droplet Mobility: Ultrahydrophobic Surfaces Are Not Always Water Repellant, Langmuir 22 (6) (2006) 2433–2436. https://doi.org/10.1021/la0525877.

[129] Y. Wang, J. Xue, Q. Wang, Q. Chen, J. Ding, Verification of Icephobic/Anti-Icing Properties of a Superhydrophobic Surface, ACS Applied Materials & Interfaces 5 (8) (2013) 3370–3381. https://doi.org/10.1021/am400429q.

[130] P.T. Naveen, R.R. Simhadri, S.K. Ranjith, Simultaneous Effect of Droplet Temperature and Surface Wettability on Single Drop Impact Dynamics, Fluid Dyn. 55 (2020) 640–652. https://doi.org/10.1134/S0015462820040084.

[131] A. Alizadeh, V. Bahadur, S. Zhong, W. Shang, R. Li, J. Ruud, M. Yamada, L. Ge, A. Dhinojwala, M. Sohal, Temperature dependent droplet impact dynamics on flat and textured surfaces, Appl. Phys. Lett. 100 (2012). https://doi.org/10.1063/1.3692598.

[132] N.B. Vargaftik, B.N. Volkov, L.D. Voljak, International Tables of the Surface Tension of Water, Journal of Physical and Chemical Reference Data 12 (3) (1983) 817–820. https://doi.org/10.1063/1.555688.

[133] Engineering ToolBox, Air Diffusion Coefficients of Gases in Excess of Air, 2018.

[134] S. Kim, K.J. Kim, Dropwise Condensation Modeling Suitable for Superhydrophobic Surfaces, Journal of Heat Transfer 133 (8) (2011) 1–8. https://doi.org/10.1115/1.4003742.

[135] K. Rykaczewski, Microdroplet Growth Mechanism during Water Condensation on Superhydrophobic Surfaces, Langmuir 28 (20) (2012) 7720–7729. https://doi.org/10.1021/la301618h.

Reference

[136] V.P. Carey, Liquid-vapor Phase-change Phenomena, third ed., CRC Press, Taylor & Francis Group, Boca Raton, 2020.

[137] R. Marek, J. Straub, Analysis of the Evaporation Coefficient and the Condensation Coefficient of Water, International Journal of Heat and Mass Transfer 44 (1) (2001) 39–53. https://doi.org/10.1016/S0017-9310.

[138] R.E.H. Miles, J.P. Reid, I. Riipinen, Comparison of Approaches for Measuring the Mass Accommodation Coefficient for the Condensation of Water and Sensitivities to Uncertainties in Thermophysical Properties, The Journal of Physical Chemistry A 116 (44) (2012) 10810–10825. https://doi.org/10.1021/jp3083858.

[139] Engineering ToolBox, Water Vapor and Saturation Pressure in Humid Air, 2004.

[140] C. Antonini, F. Villa, I. Bernagozzi, A. Amirfazli, M. Marengo, Drop Rebound after Impact: The Role of the Receding Contact Angle, Langmuir 29 (52) (2013) 16045–16050. https://doi.org/10.1021/la4012372.

[141] C. Antonini, F.J. Carmona, E. Pierce, M. Marengo, A. Amirfazli, General methodology for evaluating the adhesion force of drops and bubbles on solid surfaces, Langmuir 25 (11) (2009) 6143–6154. https://doi.org/10.1021/la804099z.

[142] Y. Shen, J. Tao, H. Tao, S. Chen, L. Pan, T. Wang, Relationship between Wetting Hysteresis and Contact Time of a Bouncing Droplet on Hydrophobic Surfaces, ACS Applied Materials & Interfaces 7 (37) (2015) 20972–20978. https://doi.org/10.1021/acsami.5b06754.

[143] Y. Xiu, L. Zhu, D.W. Hess, C.P. Wong, Relationship between work of adhesion and contact angle hysteresis on superhydrophobic surfaces, The Journal of Physical Chemistry C 112 (30) (2008) 11403–11407. https://doi.org/10.1021/jp711571k.

[144] R. Karmouch, G.G. Ross, Experimental Study on the Evolution of Contact Angles with Temperature near the Freezing Point, The Journal of Physical Chemistry C 114 (9) (2010) 4063–4066. https://doi.org/10.1021/jp911211m.

[145] K.R. Khedir, G.K. Kannarpady, H. Ishihara, J. Woo, M.P. Asar, C. Ryerson, A.S. Biris, Temperature-dependent bouncing of super-cooled water on teflon-coated

superhydrophobic tungsten nanorods, Applied Surface Science 279 (2013) 76–84. https://doi.org/10.1016/j.apsusc.2013.04.038.

[146] B. Bin Wang, Y.P. Zhao, T. Yu, Fabrication of novel superhydrophobic surfaces and droplet bouncing behavior - Part 2: Water droplet impact experiment on superhydrophobic surfaces constructed using ZnO nanoparticles, J. Adhes. Sci. Technol. 25 (2011) 93–108. https://doi.org/10.1163/016942410X501115.

[147] M.E. Schrader, Young-Dupre Revisited, Langmuir. 9 (1995) 3585–3589. https://pubs.acs.org/doi/pdf/10.1021/la00009a049.

[148] D.J. Lee, H.M. Kim, Y.S. Song, J.R. Youn, Water droplet bouncing and superhydrophobicity induced by multiscale hierarchical nanostructures, ACS Nano. 6 (2012) 7656–7664. https://doi.org/10.1021/nn3032547.

[149] Z. Li, Q. Kong, X. Ma, D. Zang, X. Guan, X. Ren, Dynamic effects and adhesion of water droplet impact on hydrophobic surfaces: Bouncing or sticking, Nanoscale. 9 (2017) 8249–8255. https://doi.org/10.1039/c7nr02906c.

[150] L. Gao, T.J. McCarthy, Teflon is hydrophilic. Comments on definitions of hydrophobic, shear versus tensile hydrophobicity, and wettability characterization, Langmuir 24 (2008) 9183–9188. https://doi.org/10.1021/la8014578.

[151] L. Gao, T.J. McCarthy, Wetting 101, Langmuir. 25 (2009) 14105–14115. https://doi.org/10.1021/la902206c.

[152] A.L. Yarin, Drop impact dynamics: splashing, spreading, receding, bouncing…, Annu. Rev. Fluid Mech. 38 (2006) 159–192. https://doi.org/10.1146/annurev.fluid.38.050304.092144.

[153] C.W. Visser, P.E. Frommhold, S. Wildeman, R. Mettin, D. Lohse, C. Sun, Dynamics of high-speed micro-drop impact: Numerical simulations and experiments at frame-to-frame times below 100 ns, Soft Matter. 11 (2015) 1708–1722. https://doi.org/10.1039/c4sm02474e.

Reference

[154] S.D. Aziz, S. Chandra, Impact, recoil and splashing of molten metal droplets, Int. J. Heat Mass Transf. 43 (2000) 2841–2857. https://doi.org/10.1016/S0017-9310(99)00350-6.

[155] V. Bergeron, D. Bonn, J.Y. Martin, L. Vovelle, Controlling droplet deposition with polymer additives, Nature. 405 (2000) 772–775. https://doi.org/10.1038/35015525.

[156] M. Abuku, H. Janssen, J. Poesen, S. Roels, Impact, absorption and evaporation of raindrops on building facades, Build. Environ. 44 (2009) 113–124. https://doi.org/10.1016/j.buildenv.2008.02.001.

[157] P. Zhang, F.Y. Lv, A review of the recent advances in superhydrophobic surfaces and the emerging energy-related applications, Energy. 82 (2015) 1068–1087. https://doi.org/10.1016/j.energy.2015.01.061.

[158] X. Gao, X. Yan, X. Yao, L. Xu, K. Zhang, J. Zhang, B. Yang, L. Jiang, The dry-style antifogging properties of mosquito compound eyes and artificial analogues prepared by soft lithography, Adv. Mater. 19 (2007) 2213–2217. https://doi.org/10.1002/adma.200601946.

[159] H. Chen, P. Zhang, L. Zhang, H. Liu, Y. Jiang, D. Zhang, Z. Han, L. Jiang, Continuous directional water transport on the peristome surface of Nepenthes alata, Nature. 532 (2016) 85–89. https://doi.org/10.1038/nature17189.

[160] D. Bartolo, C. Josserand, D. Bonn, Retraction dynamics of aqueous drops upon impact on non-wetting surfaces, J. Fluid Mech. 545 (2005) 329–338. https://doi.org/10.1017/S0022112005007184.

[161] A.I. Aria, M. Gharib, Physicochemical characteristics and droplet impact dynamics of superhydrophobic carbon nanotube arrays, Langmuir. 30 (2014) 6780–6790. https://doi.org/10.1021/la501360t.

[162] Ansys Fluent Theory Guide, Release 15.0, 2013.

[163] M. Moog, R. Keck, A. Zemitis, Some numerical aspects of the level set method, Math. Model. Anal. 3 (1998) 140–151. https://doi.org/10.1080/13926292.1998.9637097.

Reference

[164] J.U. Brackbill, D.B. Kothe, ScienceDirect - Journal of Computational Physics : A continuum method for modeling surface tension*1, J. Comput. Phys. 335354 (1992). http://www.sciencedirect.com/science/article/pii/002199919290240Y.

[165] Q.L. Liu, X.L. Ma, J. Liu, Physical property of chemistry & chemical engineering handbook, Chemical Industry Press, Beijing, 2002.

[166] J. Fukai, Y. Shiiba, T. Yamamoto, O. Miyatake, D. Poulikakos, C.M. Megaridis, Z. Zhao, Wetting effects on the spreading of a liquid droplet colliding with a flat surface: Experiment and modeling, Phys. Fluids. 7 (1995) 236–247. https://doi.org/10.1063/1.868622.

[167] J. Blake, D. Thompson, D. Raps, T. Strobl, Simulating the Freezing of Supercooled Water Droplets Impacting a Cooled Substrate, AIAA J. 53 (2015) 1725–1739. https://doi.org/10.2514/1.J053391.

[168] I. Malgarinos, N. Nikolopoulos, M. Marengo, C. Antonini, M. Gavaises, VOF simulations of the contact angle dynamics during the drop spreading: Standard models and a new wetting force model, Adv. Colloid Interface Sci. 212 (2014) 1–20. https://doi.org/10.1016/j.cis.2014.07.004.

[169] M. Bussmann, S. Chandra, J. Mostaghimi, Modeling the splash of a droplet impacting a solid surface, Phys. Fluids. 12 (2000) 3121–3132. https://doi.org/10.1063/1.1321258.

[170] Š. Šikalo, H.D. Wilhelm, I. V. Roisman, S. Jakirlić, C. Tropea, Dynamic contact angle of spreading droplets: Experiments and simulations, Phys. Fluids. 17 (2005) 1–13. https://doi.org/10.1063/1.1928828.

[171] M. Pasandideh-Fard, S. Chandra, J. Mostaghimi, A three-dimensional model of droplet impact and solidification, Int. J. Heat Mass Transf. 45 (2002) 2229–2242. https://doi.org/10.1016/S0017-9310(01)00336-2.

[172] P.R. Gunjal, V. V. Ranade, R. V. Chaudhari, Dynamics of drop impact on solid surface: Experiments and VOF simulations, AIChE J. 51 (2005) 59–78. https://doi.org/10.1002/aic.10300.

Reference

[173] I. V. Roisman, L. Opfer, C. Tropea, M. Raessi, J. Mostaghimi, S. Chandra, Drop impact onto a dry surface: Role of the dynamic contact angle, Colloids Surfaces A Physicochem. Eng. Asp. 322 (2008) 183–191. https://doi.org/10.1016/j.colsurfa.2008.03.005.

[174] S. F. Kistler, Hydrodynamics of Wetting, Wettability, (1993) 311–429.

[175] T. D. Blake, Dynamic contact angles and wetting kinetics, Wettability, (1993) 251–309.

[176] D.T. Brown, Handbook of offshore Engineering (2005) 663–708.

[177] R.B. Bird, Transport phenomena, (1965) 318–319.

Appendices

Appendix A The prepared SHS topography analyzed via the WSxM 4.0 Beta software

Figure A.1 shows the SHS topography analyzed via the WSxM 4.0 Beta software. Parameters of the prepared SHS are shown Figure A.1 as well. The test was carried out within a random surface area of 50 × 50 μm. The analysis results show that the maximum height of surface texture is 11.27 μm and the average surface roughness is 5.92 μm, taking a number of intervals of 100.

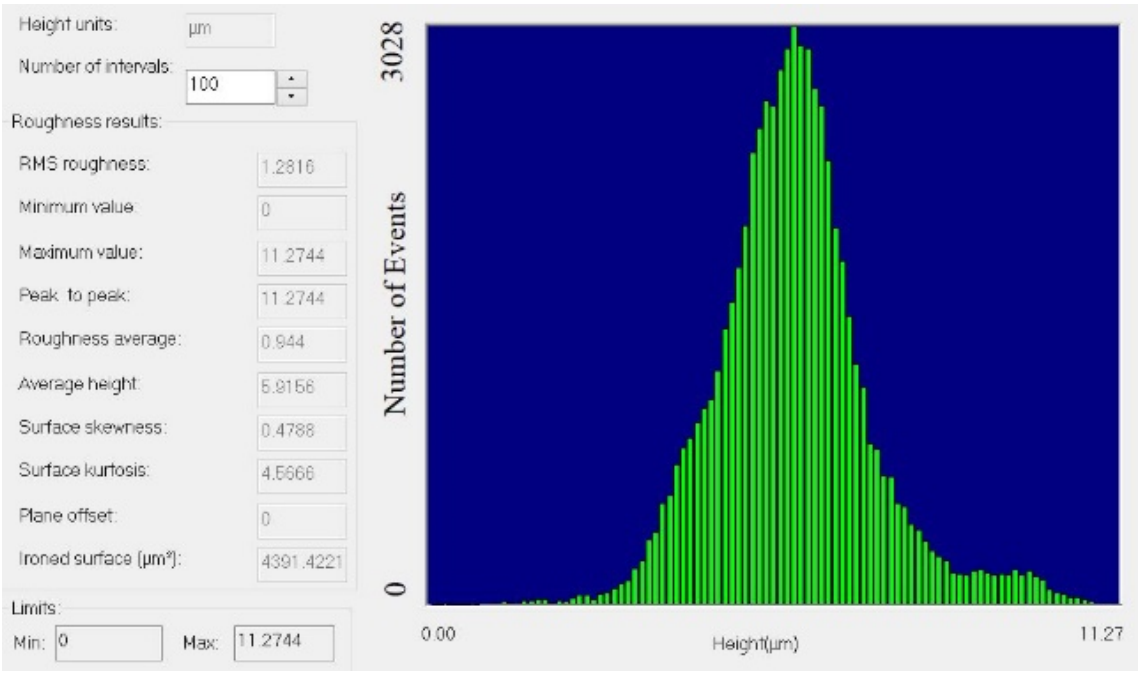

Figure A.1 The fabricated SHS topography and parameters of surface structures analyzed via the WSxM 4.0 Beta software.

Appendix B Measurement of contact angles of a sessile water droplet on SHS

Firstly, the SHS temperature and ambient temperature were controlled at 283 ± 0.2 K and 278 ± 0.2 K, respectively, and the ambient relative humidity was maintained

within the range between 2–5 %. During each measurement, a droplet was deposited gently on SHS and θ_s was measured (Figure A.2a). Then the Peltier cooling stage was tilted at a speed of 0.1 ° s^{-1} until droplet sliding happened (Figure A.2b). At moment before droplet movement, θ_a and θ_r were extracted from the images of the front and back of droplet, respectively (Figure A.2b). The difference between θ_a and θ_r was calculated as the contact angle hysteresis. α was the angle of tilted surface at which droplet sliding occurred (Figure A.2b). In this study, contact angles of sessile droplets with three different diameters D_S, D_M, and D_L were measured.

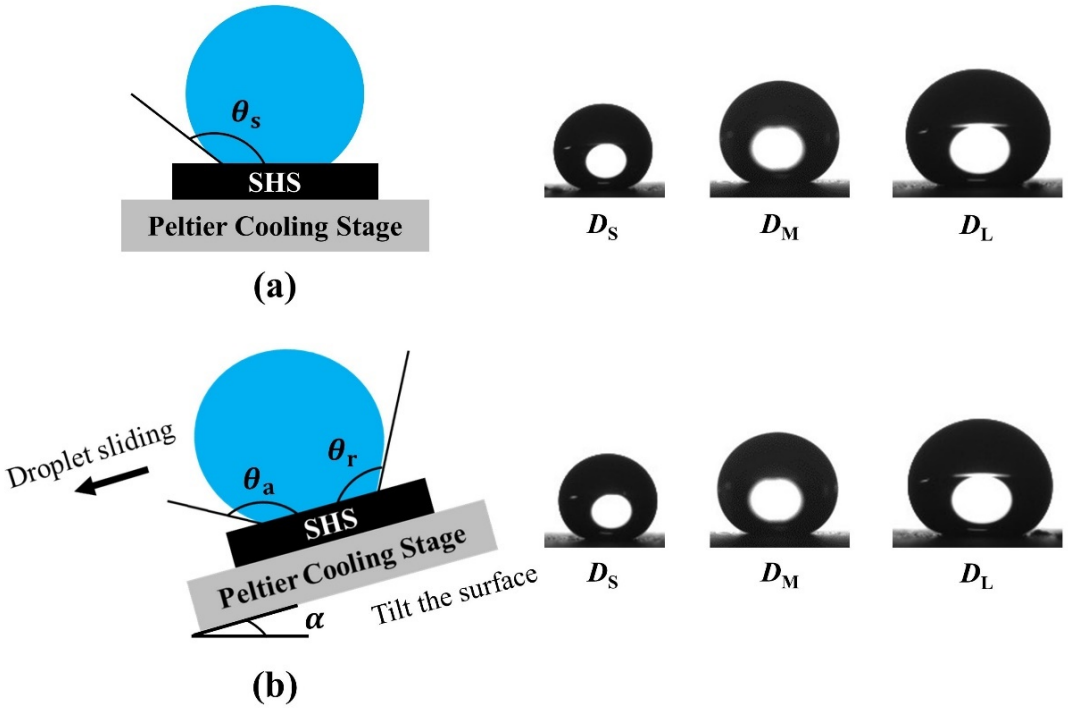

Figure A.2 (a) Schematic diagram of measuring the static contact angle θ_s of a sessile droplet on a flat SHS, and the real-time images of droplets with different diameters D_S, D_M, and D_L on a flat SHS. (b) Schematic diagram of measuring the advancing contact angle θ_a, receding contact angle θ_r, and sliding angle α of a sessile droplet on a tilted SHS, and the real-time images of droplet with different diameters D_S, D_M, and D_L on tilted SHS before sliding.

Appendix C Summary of the chemicals to fabricate super-hydrophobic surface and the employed experimental apparatuses in this work

Table A.1 and Table A.2 summarize the chemicals to fabricate super-hydrophobic surface and the experimental apparatuses utilized in this work, respectively.

Table A.1 Summary of the chemicals utilized in this work to fabricate the super-hydrophobic surface.

Experimental Apparatus	Company	Function
Acetylene black	Denki Kagaku Kogyo	To make hierarchical surface micro/nano textures.
Trimethylsiloxysilicate (KF-37312J)	Shin-Etsu Chemical	To increase surface hydrophobicity of the prepared SHS.
Ethanol (99.5 %)	Kanto Kagaku	To clean surfaces. To homogenize the suspension of AB particles and TMSS.
Copper sheet	Furukawa Electric	To be employed as the substrate to prepare SHS.

Table A.2 Summary of the experimental apparatuses, companies, and functions utilized in this work.

Experimental Apparatus	Company	Function
Magnetic Stirrer (Remix RSH-4DN)	AS ONE	To stir the nanoparticle suspension.
Ultrasonic disperser (UH-50)	SMT Co. Ltd.	To sonicate the nanoparticle suspension.
Reagent sprayer (Glass with rubber bulb)	Tokyo Glass Kikai	To spray-coat the suspension over copper sheet.
Thermal field-emission electron microscope	JEOL	To measure the SHS morphology.

(JSM-7100F)		
Atomic force microscopy (MFP-3D Infinity)	Oxford Instruments	To measure the SHS topography.
Contact angle meter (Dmo-501)	Kyowa Interface Science	To measure the contact angles of a sessile water droplet
Temperature humidity chamber (PL-3J)	Espec	To control the ambient humidity and temperature during experiments. RH and temperature are controlled within the range of 2–5 % and 278–293 K, respectively.
Humidity sensor (Hygrolog-HL-NT3)	Rotronic Instruments	To measure the ambient humidity and temperature during experiments.
Syringe pump (PHD Ultra)	Harvard Apparatus	To control the generation of water droplets.
Peltier cooling stage (VTH3500)	VICS	To control the SHS temperature during experiments from 283–248 K.
K-type thermocouple	National Instruments	To measure the SHS temperature and water droplet temperature.
High-speed camera (Mini AX2000)	Photron Fastcam	To capture the droplet impact behaviors on SHS.

Appendix D Derivation of the interfacial heat transfer coefficient

The interfacial heat transfer coefficient in Equation 3.6 of Chapter 3 in this work was derived based on Chapter 4.5 of the book Liquid-Vapor Phase-Change Phenomena written by Carey [136].

Appendices

To begin with, liquid-vapor interface is considered at molecular level because motion of vapor molecules around interface plays a central role in heat flux during condensation. Maxwell velocity distribution of classic kinetic theory of gases is used,

$$\frac{dn_{\mathrm{uvw}}}{n} = \left(\frac{m}{2\pi k_{\mathrm{B}} T}\right)^{3/2} e^{\left[-\left(\frac{m}{2k_{\mathrm{B}}T}\right)\left(u^2+v^2+w^2\right)\right]} dudvdw \tag{A1}$$

where dn_{uvw}/n is the fraction of the total number of molecules n with Cartesian velocities u, v, and w in the ranges of u to $u+du$, v to $v+dv$, and w to $w+dw$. m, k_{B}, and T represent for the one molecule mass, Boltzmann constant, and absolute temperature respectively. k_{B} can be expressed as,

$$k_{\mathrm{B}} = \frac{\bar{R}}{N_{\mathrm{A}}} \tag{A2}$$

where $\bar{R}$ is gas constant and N_{A} is Avogadro's number.

Then flux of molecules through an arbitrary plane for a gas that has a Maxwell velocity distribution can be obtained as,

$$\frac{dn_{\mathrm{u}}}{n} = \int_v \int_w \frac{dn_{\mathrm{uvw}}}{n} \tag{A3}$$

$$\frac{dn_{\mathrm{u}}}{n} = \left(\frac{m}{2\pi k_{\mathrm{B}} T}\right)^{1/2} e^{-mu^2/2k_{\mathrm{B}}T} du \tag{A4}$$

Total molecule flux j_{n} can be calculated through integrating through all possible values of u from 0 to ∞,

$$j_{\mathrm{n}} = \frac{1}{4}\frac{n}{V}\left(\frac{8k_{\mathrm{B}}T}{\pi m}\right)^{1/2} = \left(\frac{\bar{M}}{2\pi\bar{R}}\right)^{1/2} \frac{P}{mT^{1/2}} \tag{A5}$$

where $\bar{M}$ is the molecular weight of vapor.

The results above from kinetic theory of gas can be used to interpret the motion of vapor molecules near a vapor-liquid interface. Condensation occurs when the flux of vapor molecules joining the liquid exceed the flux of liquid molecules escaping to the vapor phase. At the interface, considering that pressures and temperatures in two phases are different, the net flux of molecules m''_{net} can be expressed as,

$$m''_{\text{net}} = m''_{\text{v}} - m''_{\text{l}} \tag{A6}$$

where m''_{v} and m''_{l} represent the flux of molecules from vapor to liquid and flux of molecules from liquid to vapor respectively. These two molecule fluxes are assumed to be characterized by the temperatures and pressures in different phases.

For vapor, there expectedly exists bulk motion with the velocity of w_0, therefore,

$$m''_{\text{v}} = m\hat{\sigma} j_{\text{nw}} \tag{A7}$$

$$j_{\text{nw}} = \Gamma(a)\left(\frac{\bar{M}}{2\pi\bar{R}}\right)^{1/2}\frac{P}{mT^{1/2}} \tag{A8}$$

$$\Gamma(a) = e^{a^2} + a\pi^{1/2}[1 + erf(a)] \tag{A9}$$

$$\text{a} = \frac{w_0}{\left(\frac{2\bar{R}T}{\bar{M}}\right)^{1/2}} \tag{A10}$$

For molecules emerging from liquid, it is assumed that there is no bulk motion effect, and thus,

$$m''_{\text{l}} = m\hat{\sigma} j_{\text{n}} \tag{A11}$$

$$m''_{\text{net}} = \left(\frac{\bar{M}}{2\pi\bar{R}}\right)^{1/2}\left(\frac{\Gamma\hat{\sigma}P_{\text{v}}}{T_{\text{v}}^{1/2}} - \frac{\hat{\sigma}P_{\text{l}}}{T_{\text{l}}^{1/2}}\right) \tag{A12}$$

where $\hat{\sigma}$ is the accommodation coefficient, P_{v} and T_{v} are the pressure and temperature of water vapor, P_{l} and T_{l} are the pressure and temperature of liquid.

Heat flux q'' equals to the net mass flux multiplied by the latent heat of condensation h_{fg},

$$q'' = \hat{\sigma}L\left(\frac{\bar{M}}{2\pi\bar{R}}\right)^{1/2}\left(\frac{\Gamma P_{\text{v}}}{T_{\text{v}}^{1/2}} - \frac{P_{\text{l}}}{T_{\text{l}}^{1/2}}\right) \tag{A13}$$

For small a, $\Gamma = 1 + \text{a}\pi^{1/2}$, based on ideal gas law, Equation A13 can be transformed to,

$$q'' = [\frac{2\hat{\sigma}}{2-\hat{\sigma}}]L\left(\frac{\bar{M}}{2\pi\bar{R}}\right)^{1/2}\left(\frac{P_{\text{v}}}{T_{\text{v}}^{1/2}} - \frac{P_{\text{l}}}{T_{\text{l}}^{1/2}}\right) \tag{A14}$$

To simplify Equation A14,

$$\Delta P_{\mathrm{vl}} = P_{\mathrm{v}} - P_{\mathrm{l}} \qquad \Delta T_{\mathrm{vl}} = T_{\mathrm{v}} - T_{\mathrm{l}} \tag{A15}$$

It is assumed that $\Delta P_{\mathrm{vl}}/P_{\mathrm{v}} << 1$, $\Delta T_{\mathrm{vl}}/T_{\mathrm{v}} << 1$, $P_{\mathrm{v}} = P_{\mathrm{sat}}(T_{\mathrm{v}})$ and $P_{\mathrm{l}} = P_{\mathrm{sat}}(T_{\mathrm{l}})$. Then based on Clausius-Clapeyron equation,

$$\frac{\Delta P_{\mathrm{vl}}}{\Delta T_{\mathrm{vl}}} = \frac{L}{T v_{\mathrm{lv}}} \tag{A16}$$

where v_{lv} is the specific volume and L is the latent heat of condensation. Then Equation A14 can be simplified to,

$$q^{"} = \left[\frac{2\hat{\sigma}}{2-\hat{\sigma}}\right]\left(\frac{L^2}{T_{\mathrm{v}} v_{\mathrm{lv}}}\right)\left(\frac{\bar{M}}{2\pi \bar{R} T_{\mathrm{v}}}\right)^{1/2}\left(1 - \frac{P_{\mathrm{v}} v_{\mathrm{lv}}}{2L}\right)\Delta T_{\mathrm{vl}} \tag{A17}$$

Heat transfer coefficient for the interface h_{i} can be defined as,

$$h_{\mathrm{i}} = \frac{q^{"}}{\Delta T_{\mathrm{vl}}} = \left[\frac{2\hat{\sigma}}{2-\hat{\sigma}}\right]\left(\frac{L^2}{T_{\mathrm{v}} v_{\mathrm{lv}}}\right)\left(\frac{\bar{M}}{2\pi \bar{R} T_{\mathrm{v}}}\right)^{1/2}\left(1 - \frac{P_{\mathrm{v}} v_{\mathrm{lv}}}{2L}\right) \tag{A18}$$

$$\frac{P_{\mathrm{v}} v_{\mathrm{lv}}}{2L} \approx 0 \tag{A19}$$

$$\rho_{\mathrm{v}} \approx 1/v_{\mathrm{lv}} \tag{A20}$$

where ρ_{v} is the water vapor density, then the interfacial heat transfer coefficient h_{i} can be obtained as,

$$h_{\mathrm{i}} = \frac{2\hat{\sigma}}{2-\hat{\sigma}}\left(\frac{\rho_{\mathrm{v}} L^2}{T_{\mathrm{v}}}\right)\left(\frac{\bar{M}}{2\pi \bar{R} T_{\mathrm{v}}}\right)^{1/2} \tag{A21}$$

Appendix E Measured contact area between a droplet and SHS

By assuming that the contact area between a droplet and an SHS is a circle with a diameter of d, the maximum values of d were measured from the instantaneous side-view images as shown in Figure 4.1. Table A.3 shows the mean values of the measured $d_{\max}$ for three repeat experiments under various experimental conditions.

Table A.3 Measured droplet-SHS maximum contact length $d_{\max}$ of three repeat experiments under various experimental conditions.

D	T_{wd} (K)	T_{s} (K)	$d_{\max}$ (mm)
D_{M}	278	283	3.83 ± 0.06
		278	3.83 ± 0.05
		273	3.79 ± 0.04
		268	3.84 ± 0.04
		263	3.86 ± 0.05
		258	3.86 ± 0.04
		253	3.87 ± 0.03
		248	3.88 ± 0.07
	283	283	3.82 ± 0.03
		268	3.82 ± 0.06
		263	3.84 ± 0.03
		258	3.83 ± 0.03
	293	283	3.83 ± 0.05
		268	3.82 ± 0.04
		263	3.82 ± 0.05
		258	3.81 ± 0.05
D_{S}	283	283	3.04 ± 0.08
		268	3.03 ± 0.05
		263	3.03 ± 0.02
		258	3.07 ± 0.01
D_{L}		283	4.77 ± 0.07
		268	4.79 ± 0.11
		263	4.75 ± 0.06
		258	4.75 ± 0.05

Appendix F Dynamic contact angle change during droplet impact on a surface

For the impact of a droplet on a surface, when contact line moves, there is contact angle changes depending on contact line movement velocity, static contact angle, droplet viscosity, and surface tension coefficient. In literature, empirical relations (e.g., Kistler's law [174]) and theoretical models (e.g., Blake's model [175]) can be found and employed to calculate the contact angle changes. In this work, Kistler's law (Equation A22 and Equation A23) is employed to evaluate the contact angle changes as shown in Figure A.3 when the contact line velocity v_{CL} increases from 0 to 2 m s^{-1} and the static contact angle θ_{s} decreases from 160° to 80°, respectively. Based on the maximum contact length in Table A.3, the average recoiling velocity of the contact line is around 0.38 m s^{-1}. Figure A.3 shows that for this contact line velocity (0.38 m s^{-1}) the contact angle change ($\theta_{\mathrm{s}} - \theta$) is within 3°.

$$\theta = f_{\mathrm{H}}\left[\frac{v_{\mathrm{CL}}\mu}{\gamma} + f_H^{-1}(\theta_{\mathrm{s}})\right] \tag{A22}$$

$$f_{\mathrm{H}} = \arccos\left\{1 - 2\tanh\left[5.16\left(\frac{x}{1 + 1.31x^{0.99}}\right)\right]^{0.706}\right\} \tag{A23}$$

where v_{CL} is the contact line velocity.

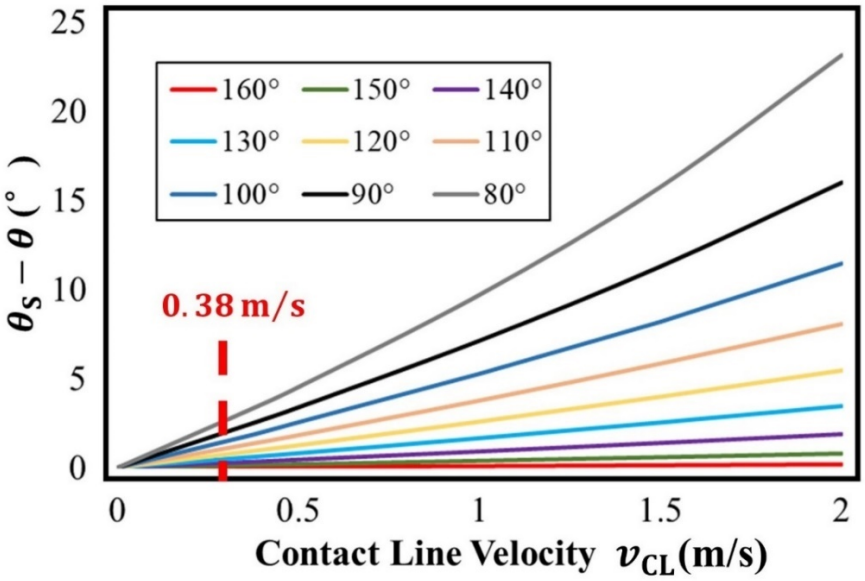

Figure A.3 The contact angle change ($\theta_s - \theta$) when the contact line moves as the contact line velocity v_{CL} and static contact angle θ_s change from 0 to 2 m s^{-1} and from 160° to 80°, respectively. Viscosity μ is taken as $1.52e^{-3}$ N s m^{-2} and surface tension coefficient γ is taken as $7.49e^{-2}$ N m^{-1}.

Appendix G d_{max} and d_{min} of an impact water droplet on a surface in parametric study.

Table A.4 maximum contact length d_{max} and minimum contact length d_{min} of an impact water droplet on a surface in parametric study.

θ_r (°)	μ_w (N s m^{-2})	γ (N m^{-1})	d_{max} (mm)	d_{min} (mm)
180				0
160				0
140	1.52e^{-3}	7.49e^{-2}	3.50	0
120				0
100				1.25
80				2.09

140	$9.9e^{-4}$	$7.49e^{-2}$	3.58	0
	$6.27e^{-3}$		3.47	0
140	$1.52e^{-3}$	$7.28e^{-2}$	3.61	0
		$7.93e^{-2}$	3.47	0

Appendix H Contact angle model with the accumulation of condensed water inside SHS micro/ nano textures

In literature, Cassie's model [79] and Wenzel's model [80] have been widely employed to calculate the contact angles when different wetting states exist. Figure A.4 shows the schematic diagrams of Cassie state and Wenzel state. For Cassie state, when there is a small displacement dx, the surface energy change dE can be expressed as,

$$dE = f_1(\gamma_{\mathrm{SL1}} - \gamma_{\mathrm{SG1}})dx + f_2(\gamma_{\mathrm{SL2}} - \gamma_{\mathrm{SG2}})dx + \gamma_{\mathrm{LG}}\cos\theta_{\mathrm{Cassie}}dx \quad \text{(A24)}$$

$$f_1 = \frac{m}{m+n} \quad \text{(A25)}$$

$$f_2 = \frac{n}{m+n} \quad \text{(A27)}$$

$$\cos\theta_{\mathrm{Cassie}} = f_1\cos\theta_{\mathrm{s-ideal}} - f_2 \quad \text{(A28)}$$

where θ_{Cassie} is the contact angle at Cassie state and $\theta_{\mathrm{s-ideal}}$ refers to the contact angle on a perfect surface without roughness. m and n are the parameters of surface structures. For Wenzel state, the surface energy change dE for a small displacement dx is,

$$dE = r(\gamma_{\mathrm{SL}} - \gamma_{\mathrm{SG}})dx + \gamma_{\mathrm{LG}}\cos\theta_{\mathrm{Wenzel}}dx \quad \text{(A29)}$$

$$r = \frac{(2h+m+n)}{(m+n)} \quad \text{(A30)}$$

$$\cos\theta_{\mathrm{Wenzel}} = r\cos\theta_{\mathrm{s-ideal}} \quad \text{(A31)}$$

where θ_{Wenzel} is the contact angle at Wenzel state, and h is the height of the SHS textures.

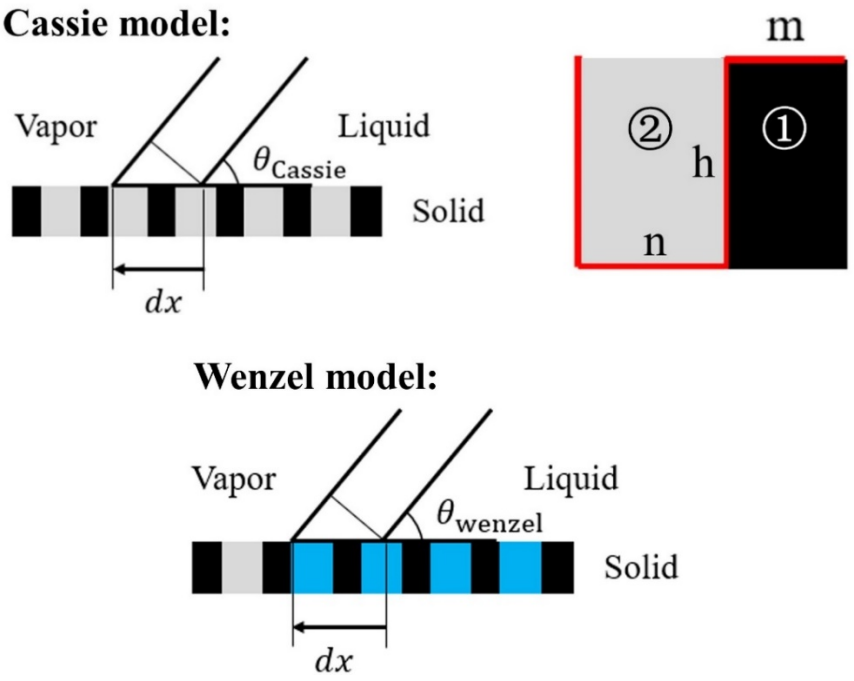

Figure A.4 Schematic diagram of the Cassie state and Wenzel state.

Figure A.5 shows the schematic diagram when part of the SHS textures is occupied with condensed water during droplet impacting process. For the current SHS with non-uniform surface textures based on AFM measurement result, the average height of surface structure h can be obtained. However, it is challenging to evaluate other surface parameters a, b, and c. Therefore, SHS with uniform surface textures is necessary for this work. In addition, both Cassie model and Wenzel model calculate contact angles of a sessile water droplet. However, for contact line movement during droplet impacting process, extra force or energy should be considered when developing the balance at triple-phase contact line.

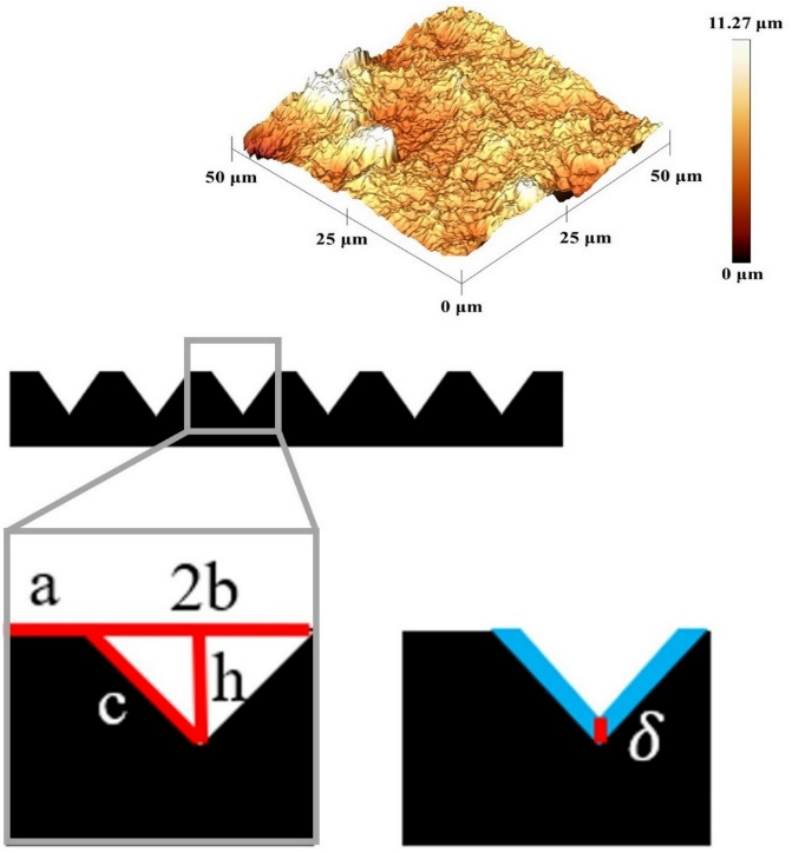

Figure A.5 Schematic diagram when part of the SHS textures is occupied by condensed water during droplet impacting process.

Publication List

Journal Papers:

[1] **H. Wang**, Q. Wu, J. Okagaki, A. Alizadeh, J.A. Shamim, W.L. Hsu, H. Daiguji, Bouncing behavior of a water droplet on a super-hydrophobic surface near freezing temperatures, Int. J. Heat Mass Transf. 174 (2021) 121304. https://doi.org/10.1016/j.ijheatmasstransfer.2021.121304.

[2] **H. Wang**, W.L. Hsu, H. Daiguji, Numerical investigation of the droplet impact on a super-hydrophobic surface near freezing temperatures, Int. J. Heat Mass Transf. (Working paper)

Conference Papers:

[1] **H. Wang**, Q. Wu, J. Okagaki, A. Alizadeh, J.A. Shamim, W.L. Hsu, H. Daiguji, Rebounding behavior of an impinging water droplet on a super-hydrophobic surface near freezing temperatures, 2nd Asian Conference on Thermal Sciences, October 2021.

[2] **H. Wang**, Q. Wu, J. Okagaki, A. Alizadeh, W.L. Hsu, H. Daiguji, Rebounding and sticking mechanism of an impinging water droplet on super-hydrophobic surfaces around freezing point, Japan Society of Refrigerating and Air Conditioning Engineering (JSRAE) Annual Conference, September 2020.

[3] Q. Wu, **H. Wang**, J. Okagaki, A. Alizadeh, W.L. Hsu, H. Daiguji, Frost induced freezing of a water droplet on a super-hydrophobic surface, Japan Society of Refrigerating and Air Conditioning Engineering (JSRAE) Annual Conference, September 2020.